

Synthesis of Functionalized Porphyrins and Corroles and Their Applications in Materials Science

By

ANTARA GARAI
CHEM07201004011

National Institute of Science Education and Research
Bhubaneswar, Odisha-751005

A thesis submitted to the
Board of Studies in Chemical Sciences
In partial fulfilment of requirements
for the Degree of

DOCTOR OF PHILOSOPHY

of

HOMI BHABHA NATIONAL INSTITUTE


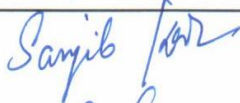
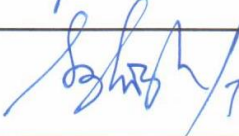
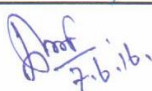
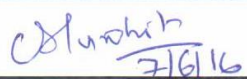


June, 2016

Homi Bhabha National Institute¹

Recommendations of the Viva Voce Committee

As members of the Viva Voce Committee, we certify that we have read the dissertation prepared by **Antara Garai** entitled “**Synthesis of Functionalized Porphyrins and Corroles and Their Applications in Materials Science**” and recommend that it may be accepted as fulfilling the thesis requirement for the award of Degree of Doctor of Philosophy.


Chairman - <Prof. Tapobrata Som>	Date:  07/06/2016
Guide / Convener - <Dr. Sanjib Kar>	Date:  07/06/2016
Examiner - <Prof. Sundargopal Ghosh, (IIT Madras)>	Date:  7/6/2016
Member 1- <Prof. A. Srinivasan>	Date:  7.6.16
Member 2- <Dr. Chandra Shekhar Purohit>	Date:  7/6/16

Final approval and acceptance of this thesis is contingent upon the candidate's submission of the final copies of the thesis to HBNI.

I/We hereby certify that I/we have read this thesis prepared under my/our direction and recommend that it may be accepted as fulfilling the thesis requirement.

Date: 07.06.2016

Place: NISER
BHUBANESHWAR

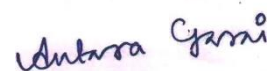

<Signature>
Guide

¹ This page is to be included only for final submission after successful completion of viva voce.

STATEMENT BY AUTHOR

This dissertation has been submitted in partial fulfilment of requirements for an advanced degree at Homi Bhabha National Institute (HBNI) and is deposited in the Library to be made available to borrowers under rules of the HBNI.

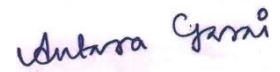
Brief quotations from this dissertation are allowable without special permission, provided that accurate acknowledgement of source is made. Requests for permission for extended quotation from or reproduction of this manuscript in whole or in part may be granted by the Competent Authority of HBNI when in his or her judgment the proposed use of the material is in the interests of scholarship. In all other instances, however, permission must be obtained from the author.

A handwritten signature in purple ink that reads "Antara Garai".

Antara Garai

DECLARATION

I, hereby declare that the investigation presented in the thesis has been carried out by me. The work is original and has not been submitted earlier as a whole or in part for a degree / diploma at this or any other Institution / University.

A handwritten signature in purple ink that reads "Antara Garai".

Antara Garai

List of Publications

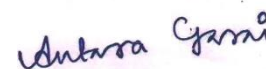
1. ***Garai, A.**; Kumar, S.; Sinha, W.; Purohit, C. S.; Das, R.; Kar, S., A comparative study of optical nonlinearities of *trans*-A₂B-corroles in solution and in aggregated state. *RSC Adv.* **2015**, *5* (36), 28643-28651.
2. ***Garai, A.**; Kumar, M.; Sinha, W.; Chatterjee, S.; Purohit, C. S.; Som, T.; Kar, S., Synthesis, electron transport, and charge storage properties of fullerene-zinc porphyrin hybrid nanodiscs. *RSC Adv.* **2014**, *4* (109), 64119-64127.
3. Sinha, W.; Kumar, M.; **Garai, A.**; Purohit, C. S.; Som, T.; Kar, S., Semi-insulating behaviour of self-assembled tin(IV)corrole nanospheres. *Dalton Trans.* **2014**, *43* (33), 12564-12573.
4. Sinha, W.; Deibel, N.; Agarwala, H.; **Garai, A.**; Schweinfurth, D.; Purohit, C. S.; Lahiri, G. K.; Sarkar, B.; Kar, S., Synthesis, spectral characterization, structures, and oxidation state distributions in [(corrolato)Fe^{III}(NO)]_n (n = 0, +1, -1) Complexes. *Inorg. Chem.* **2014**, *53* (3), 1417-1429.
5. Sinha, W.; Deibel, N.; **Garai, A.**; Schweinfurth, D.; Anwar, S.; Purohit, C. S.; Sarkar, B.; Kar, S., In-situ spectroelectrochemistry (EPR, UV-Visible) and aggregation behavior of H₂BDCP and Zn(II)BDCP [BDCP = {5,10,15,20-tetrakis[3,4-(1,4-dioxan)phenyl]porphyrin}²⁻]. *Dyes and Pigments* **2014**, *107*, 29-37.
6. Pradhan, N.; Pratheek, B.M.; **Garai, A.**, Kar, Sanjib *et al.*, Induction of apoptosis by Fe(salen)Cl through caspase-dependent pathway specifically in tumor cells. *Cell Biology International* **2014**, *38*, 1118-1131.
7. ***Garai, A.**; Nandy, P.; Sinha, W.; Purohit, C. S.; Kar, S., A new synthetic protocol for the preparation of 5-cyano-10,15,20-tris(alkoxyphenyl)porphyrins. *Polyhedron* **2013**, *56*, 18-23.

8. Kar, S.; **Garai, A.**; Bala, S.; Purohit, C.S., Tetrakis (μ -3-methoxybenzoato $\kappa^2O^1:O^1$)bis[acetonitrilecopper(II)]. *Acta Cryst.* **2011**, *E67*, m557.

*pertaining to the present thesis.

Conferences

1. “Symposium in Chemistry”, Chemical Research Society of India (CRSI-2011), February 4-6, **2011**, conducted at Kalinga Institute of Industrial Technology (KIIT), Bhubaneswar, India.
2. Indo-European symposium on frontiers of chemistry, November 10-12, **2011**, conducted at National Institute of Science Education and Research (NISER), Bhubaneswar, India.
3. **Poster Presentation:** Indo-French Symposium on functional Metal Organics: Applications in Materials and Catalysis, February 24-26, **2014**, conducted at National Institute of Science Education and Research (NISER), Bhubaneswar, India.



Antara Garai

To my Family....

ACKNOWLEDGEMENTS

*I am deeply indebted to my research supervisor, **Dr. Sanjib Kar**, for his heartfelt depth of knowledge and an enduring dedication in research. His innovative ideas and moral support inspired me throughout the journey of my research period. I take this golden opportunity to convey my earnest gratitude to him from the core of my heart.*

*I am thankful to **Prof. T. K. Chandrashekar**, Founder Director-NISER and **Prof. V. Chandrashekar**, Director-NISER for the research infrastructure and NISER for financial support.*

*I am grateful to **Prof. Tapobrata Som** (Institute of Physics) and **Dr. Ritwick Das** (School of Physical Science, NISER) for the application part of my research. **Dr. H. Biswal** helped me for the detailed theoretical studies. I am thankful to my thesis committee members **Dr. Moloy Sarkar** and **Dr. C.S. Purohit** for their continuous help. I wish to extend my profound thanks to **Dr. Arindam Ghosh** and **Dr. Nagendra Sharma** for their continuous support for the analysis of NMR and mass spectra. I am also greatly privileged by the immense help of all faculty members of School of Chemical Sciences.*

*I thank my lab members **Woormi, Bratati, Payel, Sajal and Yogesh**. I am always boosted up by my friends and seniors specially **Adi, Subba, Tapas, Milan, Mriganka, Pardhu, Ajesh, Sudhir, Manoj, Reddy, Sameer and Mohit**.*

*No words are enough for my pillar of strength, my husband **Mr. Somnath Dawn** in all my endeavours.*

*I am indebted to my first teachers, my **parents** and my brother **Aditya** without whom it was impossible to fulfil my dream. Their endless sacrifice and immense support helped me to pursue my doctoral degree.*

Antara Garai

CONTENTS

	Page No
Synopsis	13
List of Schemes	23
List of Figures	24
List of Tables	31
List of Abbreviations	32
Chapter 1	
Introduction	
1.1 Porphyrin	36
1.1.1 General Synthetic Procedures	38
1.1.2 Cyanoporphyrin	39
1.1.3 Porphyrin-fullerene dyad	41
1.2 Porphyrin Analogue	
1.2.1 Corrole	44
1.2.2 General Synthetic Procedures	46
1.2.3 Aromaticity and Planarity	52
1.2.4 Photophysical Studies	54
1.2.5 Nonlinear Optics	54
1.2.5.1 Nonlinear Optical Material	55
1.3 Objective of Present Thesis	56
References	59

Chapter 2

A New Synthetic Protocol For the Preparation of 5-Cyano-10, 15, 20 tris(alkoxy phenyl)porphyrins

2.1	Abstract	67
2.2	Introduction	68
2.3	Results and Discussion	
2.3.1	Synthesis, Spectral Analysis, and Photophysical Studies	69
2.3.2	X-Ray Analysis	75
2.3.3	Mechanism	78
2.4	Conclusions	85
2.5	Experimental Section	
2.5.1	Material and Methods	86
2.5.2	Physical Measurements	86
2.5.3	Crystal Structure Determination	86
2.5.4	Synthesis of Porphyrin 1	87
2.5.5	Synthesis of Porphyrin 2	89
	References	93

Chapter 3

Synthesis, Electron Transports, and Charge Storage Properties of Fullerene-Zinc Porphyrin Hybrid Nanodiscs

3.1	Abstract	97
3.2	Introduction	98
3.3	Results and Discussion	
3.3.1	Synthesis and Characterization	100

3.3.2	Growth Mechanism	103
3.3.3	X-ray Structural Studies of ZnTANP	104
3.3.4	Electronic Spectra	106
3.3.5	X-ray Photoelectron Spectroscopy (XPS)	107
3.3.6	X-ray Diffraction (XRD)	108
3.3.7	<i>I-V</i> Characteristics	109
3.3.8	<i>C-V</i> Characteristics	112
3.4	Conclusions	113
3.5	Experimental Section	
3.5.1	Materials	114
3.5.2	Characterization	114
3.5.3	Crystal Structure Determination	116
3.5.4	Preparation of C ₆₀ -ZnTANP Hybrid Material	117
References		118

Chapter 4

A Comparative Study of Optical Nonlinearities of trans-A₂B-Corroles in Solution and in Aggregated State

4.1	Abstract	123
4.2	Introduction	125
4.3	Results and Discussion	
4.3.1	Synthesis and Characterization	127
4.3.2	Structures	128
4.3.3	Electronic Spectra	131
4.3.4	Emission Spectra	132
4.3.5	Self-aggregates of 1-3	134

4.3.6	Measurements of NLO Properties	138
4.3.7	Theoretical Model for Analysing NLO Responses	139
4.3.8	Results	142
4.4	Conclusions	146
4.5	Experimental Section	
4.5.1	Materials	147
4.5.2	Physical Measurements	147
4.5.3	Crystal Structure Determination	148
4.5.4	NLO Measurement	148
	References	158
	Summery and Future Prospect	163

SYNOPSIS

The ‘pigment of life’ porphyrin and its analogues are imperatively involved in the natural biological system.¹ Apart from their biological significance, porphyrin has tremendous impact over multidisciplinary areas. Tetrapyrrole macrocycles other than porphyrin, like core-modified porphyrinoid are considerably optimized and developed over time.² Among these, corrole, a model complex for the corrin ring in vitamin B₁₂ is quite important. It has an intermediate structure between porphyrin and corrin with a direct bipyrrrole link between two pyrrole rings. Thus, from the aspect of aromaticity (Figure 1) and other physical properties, corrole has close resemblance to the porphyrin ring. In addition to the rich coordination chemistry, diverse catalytic activity, medicinal aspect, nonlinear properties of corrole derivatives has encouraged researcher to create an independent and new area of interest.³⁻⁵

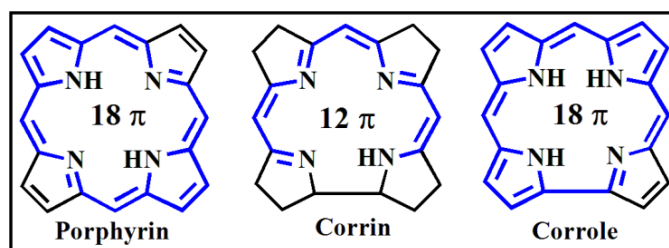


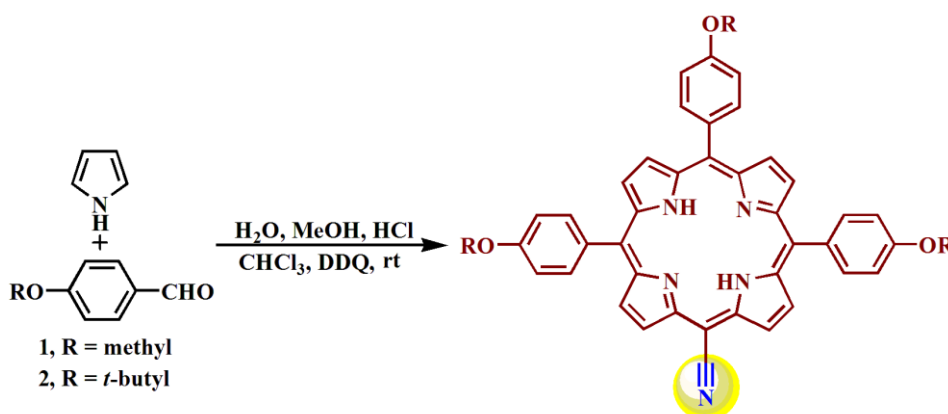
Figure 1. Basic difference of aromaticity in the porphyrin, corrin and corrole macrocycles. Aromatic path is shown in *dark blue* .

Organization of the thesis

Chapter 1: Introduction

This chapter deals with a short introduction about porphyrin and contracted porphyrinoid, corrole. Present development in porphyrin chemistry has been discussed elaborately. After first synthetic approach in 1965, synthetic obstacles in corrole synthesis got a new dimension in 1999 by the work of Paolesse⁶ and Gross.⁷ Brief literature survey includes different approaches by numerous groups for reshaping corrole synthesis and its diverse application.

Chapter 2: A New Synthetic Protocol for the Preparation of 5-cyano-10, 15, 20-tris(alkoxyphenyl)porphyrins



This chapter describes a novel synthetic protocol for the *meso*-cyano substituted porphyrin, based on four key steps: (i) no requirement of porphyrin/metalloporphyrin based starting materials (ii) two step one pot synthesis (iii) absence of additional reagents for cyanation and (iv) use of comparatively less investigated solvent mixture in porphyrin synthesis. A simple benzaldehyde with *tert*-butoxy or methoxy group at the *para* position of phenyl ring undergoes this kind of cyanation reaction to yield the corresponding cyano substituted porphyrins. Both the porphyrins were characterised by their detailed spectroscopic results along with one representative crystal structure of porphyrin **2** (Figure 2).

Here, a unique solvent system, H₂O/HCl/MeOH is used for the synthesis of porphyrin. Trace amount (0.002%) of formaldehyde is always present in the reagent grade methanol. The presence of di(1*H*-pyrrol-2-yl)methane and unsubstituted tetrapyrane supports the presence of the formyl group in the reaction mixture. Furthermore, the combination of H₂O/HCl/MeOH system and *p*-chloranil resulted only symmetrical corrole (4-5%) and porphyrin (2-3%) and cyano substituted porphyrin was not formed at all. This clearly proved that DDQ exclusively supplies the *meso*-cyano group.

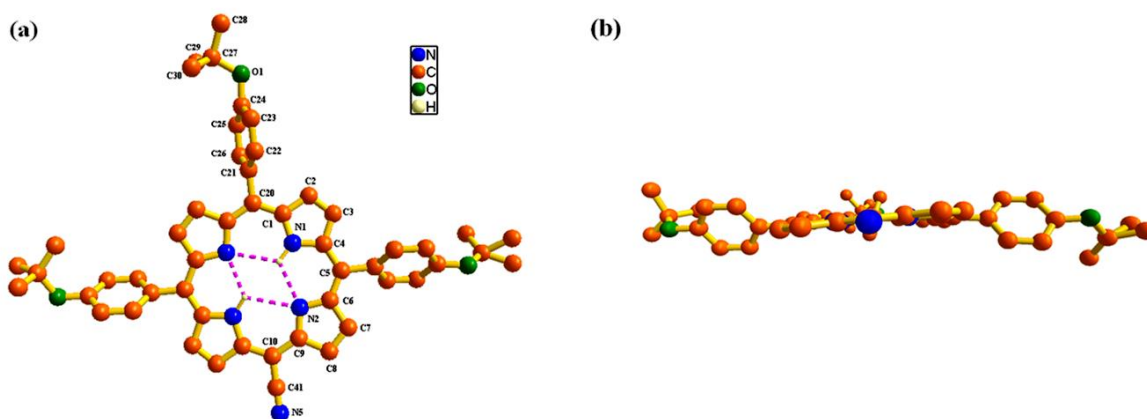
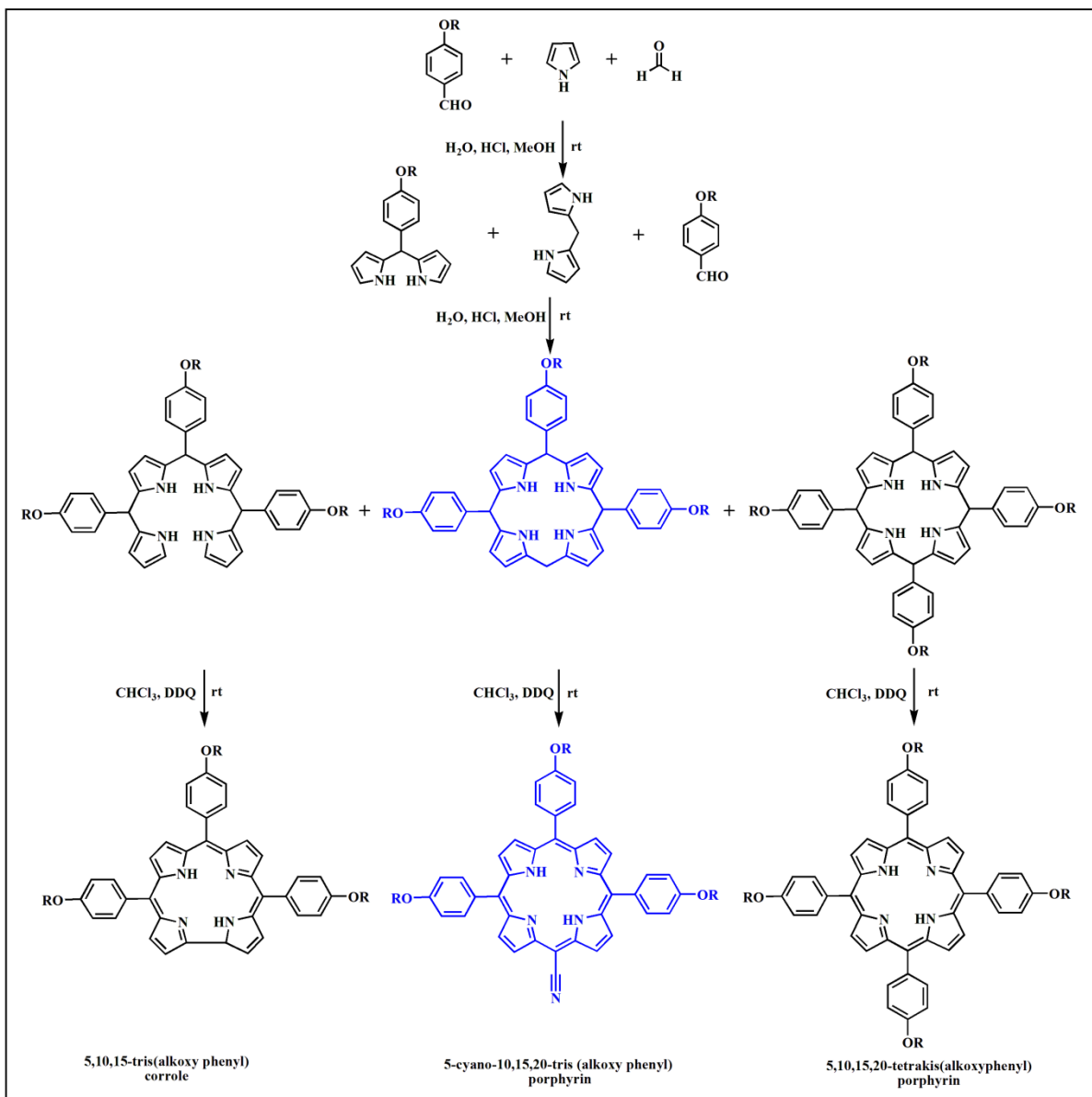


Figure 2. Single-crystal X-ray structure of porphyrin **2**. (a) top view with intramolecular hydrogen bonding interaction between the amine and imine units, (b) side view. Hydrogen atoms omitted for clarity.

Based on GC-Mass analysis of the reaction intermediates in the reaction mixture, the following mechanism has been proposed for the formation of *meso*-cyanoporphyrin (Scheme 1). The overall reaction proceeds in two steps: (i) formation of a porphyrinogen, and (ii) conversion of the porphyrinogen to *meso*-cyanoporphyrin by DDQ. First, pyrrole and corresponding *p*-alkoxybenzaldehyde, e.g., 4-*tert*-butoxy benzaldehyde condenses in H₂O/HCl/MeOH system and results 5-(4-*tert*-butoxyphenyl)dipyrromethane (Scheme 1). Another dipyrromethane, di(1*H*-pyrrol-2-yl)methane is also formed by the condensation of pyrrole with formaldehyde (Scheme 1). In the next step both the dipyrromethanes, and the corresponding aldehyde, e.g. 4-*tert*-butoxy benzaldehyde, condense and form the desired intermediate compound 5, 10, 15-tris(4-*tert*-butoxyphenyl)porphyrinogen. In the last step, DDQ simultaneously oxidizes the porphyrinogen to the corresponding porphyrin and performs the cyanation reaction. It has been postulated that the reaction proceeds *via* the formation of an adduct between DDQ and the porphyrin^{8, 9} and successive intermolecular transfer of cyanide ion.^{10,11}



Scheme 1. Mechanistic presentation of the formation of *meso*-cyanoporphyrins.

Chapter 3: Synthesis, Electron Transports, and Charge Storage Properties of Fullerene-Zinc Porphyrin Hybrid Nanodiscs



This chapter deals with the synthesis of a hybrid material, from a novel Zn-porphyrin complex [5,10,15,20-tetrakis(1,2-dihydro-5-acenaphthylenyl)porphinato]zinc (II), ZnTANP and C₆₀ fullerene and its application in charge storage device. First, ZnTANP is synthesized and well characterized by single crystal X-ray structure (Figure 3a) and other spectroscopic techniques. X-ray crystal structure analysis of ZnTANP describes that the molecules are stacked together by various weak van der Waals forces *viz.* π - π stacking interaction, C–H \cdots N interactions and form closely packed 3D structures in the packing diagram (Figure 3b).

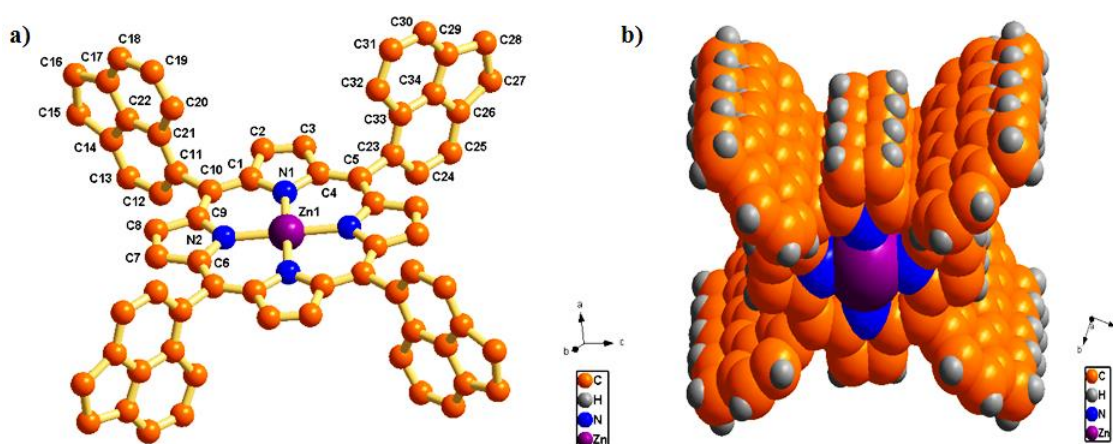


Figure 3. (a) Single-crystal X-ray structure of ZnTANP. (b) Orientation of zinc atoms in single-crystal X-ray structure of ZnTANP when viewed along *c*-axis.

Then, a donor (D)-acceptor (A) based system is developed with the help of ZnTANP complex and C₆₀ fullerene. Then different spectroscopic methods were performed to confirm the existence of a charge transfer based complex between Zn-porphyrin and C₆₀ fullerene. These porphyrins (D)-fullerene (A) based hybrid material were used to generate circular discs like nano-structure by simple drop casting method (Figure 4).

These nano objects were employed to fabricate a diode with the composition of Ag/C₆₀-ZnTANP circular discs/*p*-Si/Ag (Figure 5d). The current-voltage (*I*-*V*) characteristic of the device depicts that it is not an ideal schottky barrier diode but a metal-insulator-semiconductor (MIS) type diode. It shows a non-ideal rectifying behavior (Figure 5a) and reveals that the electrical characteristic of the Ag/C₆₀-ZnTANP/SiO_x/*p*-Si/Ag diode is largely

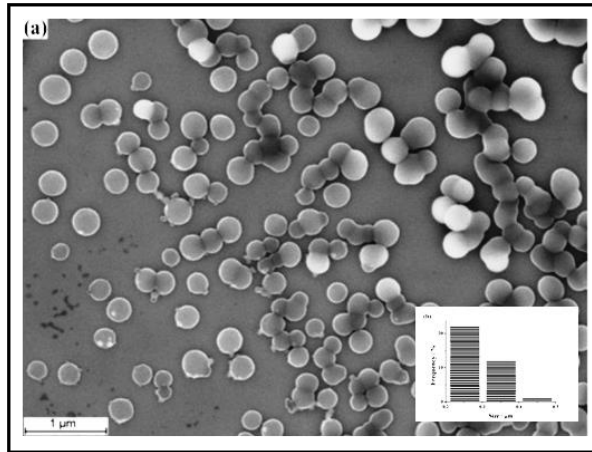


Figure 4. (a) SEM images of the C₆₀-ZnTANP circular disc, (b) size distribution histograms of circular discs (inset).

controlled by Ag-C₆₀-ZnTANP and C₆₀-ZnTANP-SiO_x interfaces. Further *C-V* measurements were also conducted for the vivid analysis of the charge storage properties of these circular discs (Figure 5c). The observed counter-clock wise a positive shift in voltage (~2.7 V) indicates hysteresis in the *C-V* measurement with a clear impression of the charge-trapping phenomena due to the electrons only. The bright spots with ~100 pA intensity, observed at 10V bias in the CAFM measurement, are assigned as leakage current (Figure 5b). These bright spots control the conduction properties in the device. It is quite evident that due to very low thickness (~2 nm) of the native oxide layer, the other alternatives, like SiO_x/Si interface, or the oxide layers are clearly ruled out from the aspects of charge storage capabilities. Henceforth, trapped charges can reside only at the C₆₀-ZnTANP circular discs/SiO_x interface. However, as the *p*-Si substrate is not fully covered by the nanodiscs, thus the possibility of other conduction pathways (Ag/*p*-Si/Ag) in the device also cannot be ruled out completely (*vide supra*). Thus our results reveal that the circular disc like nano-architectures made from C₆₀-ZnTANP hybrid materials have strong impact to the diode characteristics but its true nature cannot be identified precisely.

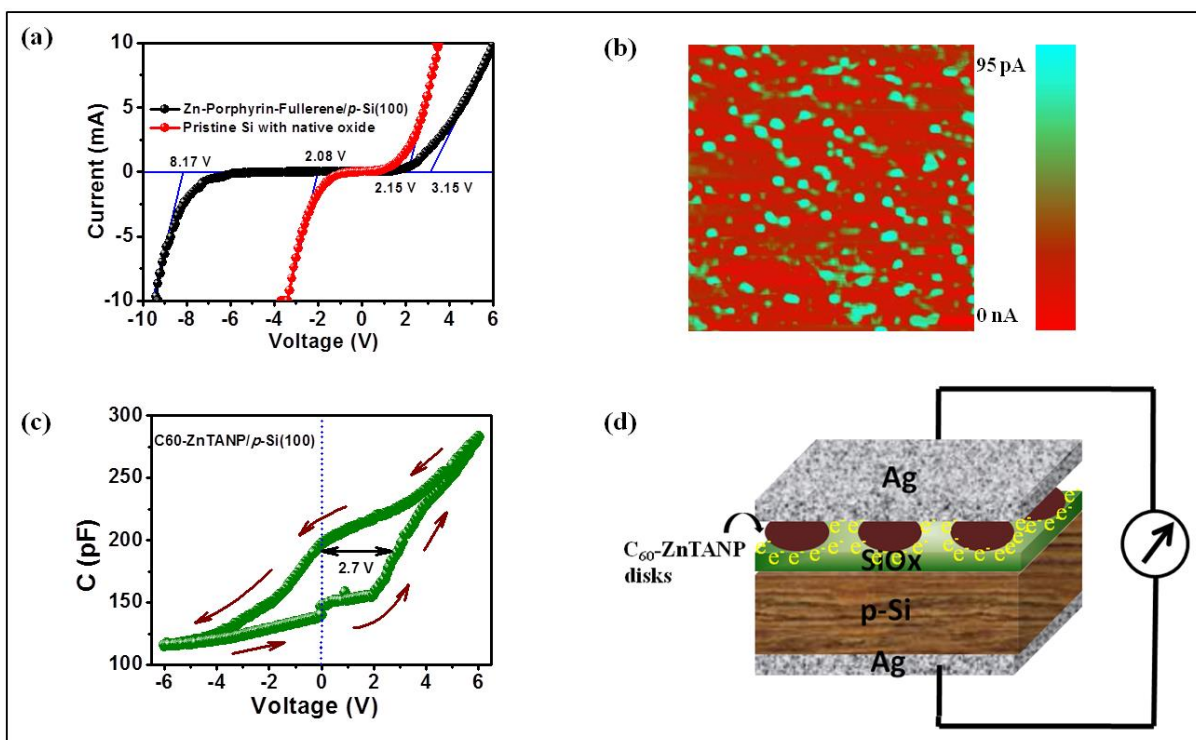
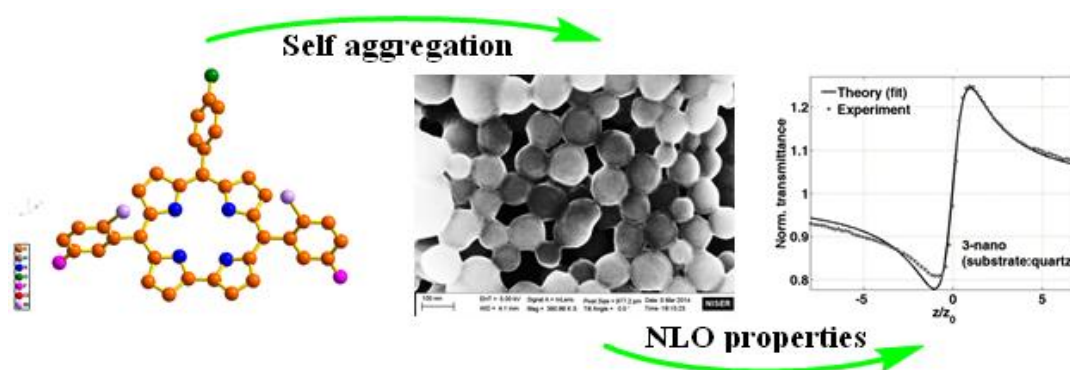


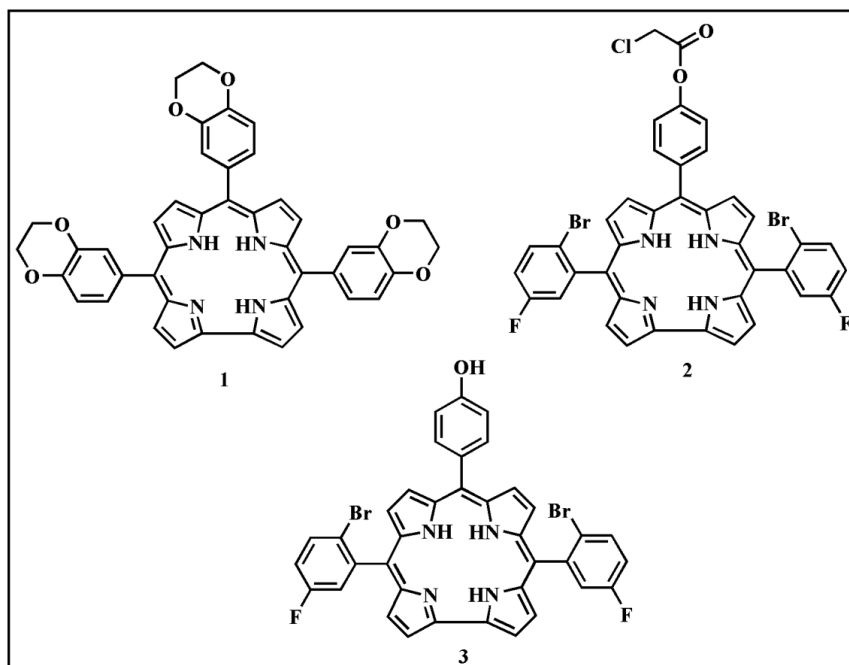
Figure 5. (a) Nonlinear I - V characteristics of Ag/C₆₀-ZnTANP circular discs/ p -Si/Ag diodes. The black solid line denotes the I - V characteristics of Ag/C₆₀-ZnTANP circular discs/ p -Si/Ag diodes and the red line are for the Ag/ p -Si/Ag diodes. (b) CAFM micrographs ($2\mu\text{m} \times 2\mu\text{m}$) of C₆₀-ZnTANP circular discs deposited on Si. (c) A voltage dependent capacitance of Ag/C₆₀-ZnTANP circular discs/ p -Si/Ag hetero structure diode. (d) Charge transport across the potential barriers is shown schematically for the hetero-structure diode Ag/ C₆₀-ZnTANP circular discs / p -Si/Ag.

Chapter 4: A Comparative Study of Optical Nonlinearities of *trans*-A₂B-corroles in Solution and in Aggregated State



Present work deals with NLO properties of a series of novel corroles, measured in both the aggregates state and in solution state. One novel A₃-corrole and two *trans*-A₂B-corroles namely 5,10,15-tris[3,4-(1,4-dioxan)phenyl]corrole, **1**, 10-[4-(chloroacetoxy)phenyl]-5,15-

bis(2-bromo-5-fluorophenyl)corrole, **2**, and 10-(4-hydroxyphenyl)-5,15-bis(2-bromo-5-fluorophenyl)corrole, **3** (Scheme 2) were synthesized and characterized by several spectroscopic techniques including single crystal X-ray structural analysis of the corrole **3** (Figure 6).



Scheme 2. Structure of the FB corroles **1-3**.

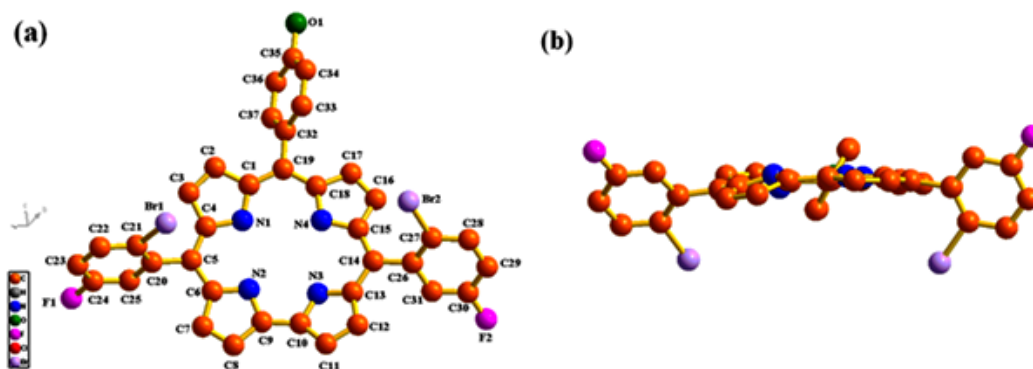


Figure 6. Single-crystal X-ray structure of **3**, (a) top view (b) side view. Hydrogen atoms omitted for clarity.

All these corrole based self-aggregates were generated on a silicon wafer as well as on quartz substrate by simple drop-casting method. In all three free base corroles, well defined and nicely organized three-dimensional objects were obtained (Figure 7). The NLO properties (nonlinear refractive index, n_2 and two-photon absorption coefficient, β) of all of

the corrole derivatives in toluene solution and in aggregated form were measured by the Z-scan technique. Two-photon absorption coefficient, β and nonlinear refractive index, n_2 , measured in the aggregated state are 100-1000 times higher compared to the solution state. Due to higher density of molecules in aggregates in addition to low mobility in solid phase,

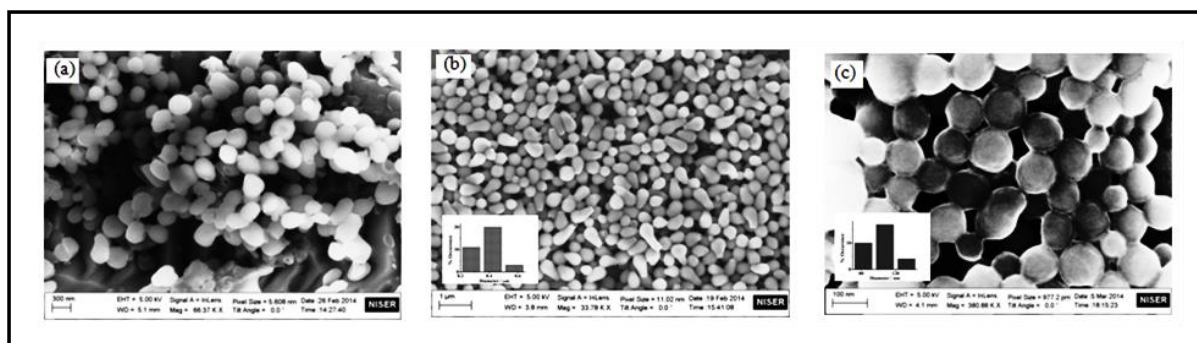


Figure 7. SEM images in dichloromethane-methanol mixture (a) **1**; nano hollow-spheres are seen (b) **2**; nanobulbs are seen. Inset shows particle size distribution histograms of nanobulbs (c) **3**; nanodiscs are seen. Inset shows particle size distribution histograms of nanodiscs.

the contribution to nonlinear optical effects is higher. Fundamentally, polarizability and ground state dipole moment controls the NLO responses. DFT study on the molecular ground state dipole moment, explains that the large improvement of nonlinear optical behavior for **1-Nano**, **2-Nano** and **3-Nano** could be due to the presence of coupled MOs and thus resulting in an enhanced transition dipole moment. Therefore, from the NLO study of these corroles, it can be concluded that the corrole-**3** and **3-Nano** are promising candidates for devising optical switch which can have direct applications in high-speed communication technology.

References

1. Milgrom, L. R., *The colours of life : an introduction to the chemistry of porphyrins and related compounds*. Oxford University Press: Oxford, **1997**.
2. Jonathan, L. S.; Steven, J. W., in: *Expanded, Contracted, & Isomeric Porphyrins*, Pergamon, Oxford: **1997**; vol. 15, pp 11-125.
3. Aviv-Harel, I.; Gross, Z., *Chem. Eur. J.* , **2009**, *15*, 8382-8394.
4. Aviv-Harel, I.; Gross, Z., *Coordination Chem. Rev.*, **2011**, *255*, 717-736.
5. Rebane, A.; Drobizhev, M.; Makarov, N. S.; Koszarna, B.; Tasiar, M.; Gryko, D. T., *Chem. Phys. Lett.*, **2008**, *462*, 246-250.
6. Paolesse, R.; Mini, S.; Sagone, F.; Boschi, T.; Jaquinod, L.; J. Nurco, D.; M. Smith, K., *Chem. Commun.*, **1999**, 1307-1308.
7. Steene, E.; Wondimagegn, T.; Ghosh, A., *J. Phys. Chem. B.*, **2001**, *105*, 11406-11413.
8. Kano, K.; Hayakawa, T.; Hashimoto, S., *Bull. Chem. Soc. Jpn.*, **1991**, *64*, 778-784.
9. Mohajer, D.; Dehghani, H., *J. Chem. Soc., Perkin Trans. 2*, **2000**, 199-205.
10. Saito, I.; Shimosono, K.; Matsuura, T., *J. Am. Chem. Soc.*, **1983**, *105*, 963-970.
11. Bury, A.; Bougeard, P.; Corker, S. J.; Johnson, M. D.; Perlmann, M., *Chem. Soc. Perkin Trans. 2*, **1982**, 1367-1372.

List of Schemes		Page No
1.	Scheme 1.1 Rothemund synthesis of tetraphenyl porphyrin.	38
2.	Scheme 1.2 Synthesis of tetraphenyl porphyrin.	39
3.	Scheme 1.3 Functionalization of cyano group.	40
4.	Scheme 1.4 Synthesis of the model complex, 1 for arginine-aspartate salt bridge.	40
5.	Scheme 1.5 Cyanation of porphyrin with cyanoethylzinc bromide.	41
6.	Scheme 1.6 Synthesis of Co-corrole metal complex by Paolesse <i>et al.</i>	47
7.	Scheme 1.7 Synthesis of 5,10,15-tris(pentafluorophenyl) corrole, 12 by Gross <i>et al.</i>	47
8.	Scheme 1.8 Synthesis of <i>meso</i> substituted corrole by Paolesse <i>et al.</i>	48
9.	Scheme 1.9 Synthesis of <i>meso</i> substituted corrole by Lee <i>et al.</i>	49
10.	Scheme 1.10 Triaryl corrole synthesis by Gryko method.	50
11.	Scheme 1.11 Synthesis of 5,10,15-tris(pentafluorophenyl)corrole by Nocera and co-workers.	51
12.	Scheme 1.12 Structure of corrole 12, 17-19	52
13.	Scheme 2.1 Structure of cyanoporphyrins.	69
14.	Scheme 2.2 Synthesis of cyanoporphyrins.	70
15.	Scheme 2.3 Mechanistic presentation of the formation of cyanoporphyrins.	81
16.	Scheme 3.1 Molecular structures of the ZnTANP.	99
17.	Scheme 4.1 Structure of the FB corroles 1-3 .	126
18.	Scheme 4.2 Synthesis of 3 .	128

	List of Figures	Page No
1.	Figure 1.1. Biologically important porphyrin derivative.	37
2.	Figure 1.2. The close approach of fullerene to the centre of a porphyrin in the crystal structure.	42
3.	Figure 1.3. Covalently linked porphyrin-fullerene dyad as artificial photosynthetic system.	43
4.	Figure 1.4. Non-covalent supramolecular assembly of porphyrin-fullerene dyad.	44
5.	Figure 1.5. Basic difference of aromaticity in the porphyrin, corrin and corrole macrocycles. Aromatic path is shown in <i>dark blue</i> .	45
6.	Figure 1.6. Water soluble corrole 9 , first corrole based medicinal approach by Gross <i>et al.</i>	46
7.	Figure 1.7. The general substitution pattern of tetraaryl porphyrins and triarylcorroles, H ₃ (tpc) (Ar = C ₆ H ₅ , 17).	52
8.	Figure 1.8. Top and side view models of the X-ray structure of corrole 17 .	53
9.	Figure 1.9. Tautomerism between two non-equivalent corrole tautomers.	53
10.	Figure 1.10. Transmittance vs. Incident light intensity for linear and optical limiting material.	56
11.	Figure 2.1. ESI-MS spectrum of porphyrin 1 in CH ₃ CN (a) shows the measured spectrum and (b) shows an expansion of the isotopic distribution pattern.	71
12.	Figure 2.2. ESI-MS spectrum of porphyrin 2 in CH ₃ CN (a) shows the measured spectrum and (b) shows an expansion of the isotopic distribution pattern.	71
13.	Figure 2.3. FTIR spectrum of porphyrin 1 , as a KBr pellet.	72

14. **Figure 2.4.** FTIR spectrum of porphyrin **2**, as a KBr pellet. 72
15. **Figure 2.5.** ^1H NMR spectrum of porphyrin **1** in CDCl_3 . 73
16. **Figure 2.6.** ^1H NMR spectrum of porphyrin **2** in CDCl_3 . 74
17. **Figure 2.7.** (a) Electronic absorption (—) and normalized emission (—) spectrum of porphyrin **1** in toluene. (b) Electronic absorption (—) and normalized emission (—) spectrum of porphyrin **2** in toluene. 75
18. **Figure 2.8.** Single-crystal X-ray structure of porphyrin **2**. (a) top view with intramolecular hydrogen bonding interaction between the amine and imine units, (b) side view. Hydrogen atoms omitted for clarity. 76
19. **Figure 2.9.** X-ray single crystal structure analysis of porphyrin **2**. (a) C-H \cdots N interactions, [2.69 Å, 163.43° and 3.12 Å, 137.47°] (b) C-H \cdots C interactions [3.09 Å, 134.66° and 3.53 Å, 168.61°] (c) C-H $\cdots\pi$ stacking interactions [3.09 Å-3.22 Å] (d) C-H \cdots O interactions, [4.06 Å, 148°] (e) CN-CN distance, [9.5 Å] and (f) π - π stacking interactions [4.01 Å]. The entries in square brackets are the distances and the angles. 78
20. **Figure 2.10.** Mass spectrum (GC-EIMS) of tetrapyrane detected by GC of the reaction mixture. 79
21. **Figure 2.11.** GC-EIMS analysis of the reaction mixture: 4-*tert*-butoxybenzaldehyde and pyrrole were dissolved in (1:1) MeOH and water mixture. After addition of conc. HCl, the reaction mixture was stirred continuously at room temperature. Aliquots of this reaction mixture were taken after 82

	two hours interval and were monitored by GC-EIMS analysis.	
22.	Figure 2.12. Mass spectrum (GC-EIMS) of 4- <i>tert</i> -butoxybenzaldehyde detected by GC of the reaction mixture.	83
23.	Figure 2.13. Mass spectrum (GC-EIMS) of 5, 10, 15-tri (4- <i>tert</i> -butoxy phenyl)porphyrinogen detected by GC of the reaction mixture.	83
24.	Figure 2.14. Mass spectrum (GC-EIMS) of 5-(4- <i>tert</i> -butoxyphenyl) dipyrromethane detected by GC of the reaction mixture.	84
25.	Figure 2.15. Mass spectrum (GC-EIMS) of 5,10,15-tri (4- <i>tert</i> -butoxy phenyl)porphyrinogen detected by GC of the reaction mixture.	84
26.	Figure 2.16. Mass spectrum (GC-EIMS) of dipyrromethane detected by GC of the reaction mixture.	85
27.	Figure 2.17. ¹³ C NMR spectrum of porphyrin 1 in CDCl ₃ .	89
28.	Figure 2.18. ¹³ C NMR spectrum of porphyrin 2 in CDCl ₃ .	91
29.	Figure 3.1. ¹ H NMR spectrum of ZnTANP in CDCl ₃ .	101
30.	Figure 3.2. ESI-MS spectrum of ZnTANP in CH ₃ CN shows the (a) measured spectrum and (b) isotopic distribution pattern.	102
31.	Figure 3.3. (a) SEM images of the C ₆₀ -ZnTANP circular disc (b) size distribution histograms of circular discs (inset).	102
32.	Figure 3.4. EDX spectrum of the C ₆₀ -ZnTANP circular disc grown on <i>p</i> -Si substrate.	103
33.	Figure 3.5. Plausible mechanism of C ₆₀ -ZnTANP circular nanodisc formation <i>via</i> aggregations of smaller sized nanodisc.	104
34.	Figure 3.6. Single-crystal X-ray structure of ZnTANP.	105
35.	Figure 3.7. Orientation of zinc atoms in single-crystal X-ray structure of	105

- ZnTANP when viewed along *c*-axis.
36. **Figure 3.8.** UV-Vis-NIR spectra of the (a) C₆₀-ZnTANP hybrid material (———), (b) C₆₀ powder (·····), and (c) ZnTANP powder (----).
 37. **Figure 3.9.I** N1s region of the X-ray photo electron spectrum of (a) ZnTANP powder, and (b) C₆₀-ZnTANP hybrid materials.
 38. **Figure 3.9.II** Zn2p_{3/2} region of the X-ray photo electron spectrum of (a) ZnTANP powder and (b) C₆₀-ZnTANP hybrid materials.
 39. **Figure 3.10.** XRD patterns of the (a) C₆₀-ZnTANP circular discs, (b) ZnTANP powder and (c) C₆₀ powder.
 40. **Figure 3.11.** (a) Nonlinear *I-V* characteristics of Ag/C₆₀-ZnTANP circular discs/*p*-Si/Ag diodes. The black solid line represents the *I-V* characteristics of Ag/C₆₀-ZnTANP circular discs/*p*-Si/Ag diodes and the red line are for the Ag/*p*-Si/Ag diodes. (b) CAFM micrographs (2μm × 2μm) of C₆₀-ZnTANP circular discs deposited on Si. (c) A voltage dependent capacitance of Ag/C₆₀-ZnTANP circular discs/*p*-Si/Ag hetero structure diode. (d) Charge transport across the potential barriers is shown schematically for the hetero-structure diode Ag/C₆₀-ZnTANP circular discs /*p*-Si/Ag.
 41. **Figure 4.1.** Single-crystal X-ray structure of **3**, (a) top view (b) side view. Hydrogen atoms omitted for clarity.
 42. **Figure 4.2.** X-ray single crystal structure analysis of 10-(4-hydroxyl phenyl)-5,15-bis(2-bromo-5-fluorophenyl)corrole, **3**, (a) O—H···N interactions, [2.86 Å] (b) π-π stacking interactions

[3.51 Å]. The entries in square brackets are the distances. (c) ORTEP diagram of **3**. Solvent molecules are removed for clarity. Ellipsoids are drawn at 30% probability.

43. **Figure 4.3.** Electronic absorption and normalized emission spectrum of **1**, (blue line), **2**, (black line), and **3**, (red line) in CH₂Cl₂. 132
44. **Figure 4.4.** Fluorescence decay profiles of (a) **1**, (—); $\lambda_{em} = 676$ nm, (b) **2**, (—) $\lambda_{em} = 654$ nm, and (c) **3**, (—); $\lambda_{em} = 661$ nm. The black line represents experimental data, whereas the red line represents best fit. 133
45. **Figure 4.5.** SEM images in dichloromethane-methanol mixture of **1**; nano hollow-spheres are seen 134
46. **Figure 4.6.** SEM images in dichloromethane-methanol mixture of **2**; nanobulbs are seen. Inset shows particle size distribution histograms of nanobulbs. 135
47. **Figure 4.7.** SEM images in dichloromethane-methanol mixture of **3**; nanodiscs are seen. Inset shows particle size distribution histograms of nanodiscs. 135
48. **Figure 4.8.** EDX elemental analysis obtained from the nano hollow-spheres of **1** showing the presence of the entire constituent elements: C, N, and O. 136
49. **Figure 4.9.** EDX elemental analysis obtained from the nanobulbs of **2** showing the presence of the entire constituent elements: C, N, O, F, Cl, and Br. 137
50. **Figure 4.10.** EDX elemental analysis obtained from the nanodiscs of **3** showing the presence of the entire constituent elements: C, N, 137

O, F, and Br.

51. **Figure 4.11.** Changes in particle size distribution of the aggregates of **3** on letting it stay in DMF and H₂O (1:1) mixture. Measurements are made at 10 minutes interval. 138
52. **Figure 4.12.** Closed aperture normalized transmittance as a function of propagation distance (*z*) for (a) 0.1 mM solution **1** (in toluene) (b) Aggregates of **1** (**1**-Nano on quartz substrate) (c) 0.1 mM solution of **2** (in toluene) (d) Aggregates of **2** (**2**-Nano on quartz substrate) (e) 0.1 mM solution of **3** (in toluene) (f) Aggregates of **3** (**3**-Nano on quartz substrate). 140
53. **Figure 4.13.** Z-scan experimental set-up using Yb-fiber laser source; FI: Fiber laser; HWP: Half-wave plate; PBS: Polarizing beam-splitter; L: Lens (*f* =100 mm); TS: Translation stage (10 cm travel; S: Sample; A: Aperture (*S* ~ 0.3); PD1: Reference photodetector; PD2: Signal photodetector. 141
54. **Figure 4.14.** DFT optimized (BP-86/TZVP) structures of (a) **1**, (b) **2**, and (c) **3**, obtained are in the same order of magnitudes (3.05, 1.67, and 2.45 Debye respectively for the FB corroles **1-3**). 146
55. **Figure 4.15.** ¹H NMR spectrum of 2,2'-((2-bromo-5-fluorophenyl)methylene) bis(1*H*-pyrrole) in CDCl₃. 150
56. **Figure 4.16.** ESI-MS spectrum of 2,2'-((2-bromo-5-fluorophenyl)methylene)bis(1*H*-pyrrole) in CH₃CN shows the measured spectrum with isotopic distribution pattern. 151
57. **Figure 4.17.** ¹H NMR spectrum of 5,10,15-tris[3,4-(1,4-dioxan)phenyl] corrole, **1** in CDCl₃. 152

58. **Figure 4.18.** ESI-MS spectrum of 5, 10, 15-tris[3, 4-(1, 4-dioxan)phenyl] corrole, **1** in CH₃CN shows the measured spectrum with isotopic distribution pattern. 153
59. **Figure 4.19.** ¹H NMR spectrum of 10-[4-(chloroacetoxy)phenyl]-5,15-bis(2-bromo-5-fluorophenyl)corrole, **2**, in CDCl₃. 154
60. **Figure 4.20.** ¹³C NMR spectrum of 10-[4-(chloroacetoxy)phenyl]-5,15-bis(2-bromo-5-fluorophenyl)corrole, **2**, in CDCl₃. 154
61. **Figure 4.21.** ESI-MS spectrum of 10-[4-(chloroacetoxy)phenyl]-5,15-bis(2-bromo-5-fluorophenyl)corrole, **2**, in CH₃CN shows the measured spectrum with isotopic distribution pattern. 155
62. **Figure 4.22.** ¹H NMR spectrum of 10-(4-hydroxyphenyl)-5,15-bis(2-bromo-5-fluorophenyl)corrole, **3** in CDCl₃. 156
63. **Figure 4.23.** ¹³C NMR spectrum of 10-(4-hydroxyphenyl)-5,15-bis(2-bromo-5-fluorophenyl)corrole, **3** in CDCl₃. 156
64. **Figure 4.24.** ESI-MS spectrum of 10-(4-hydroxyphenyl)-5,15-bis(2-bromo-5-fluorophenyl)corrole, **3** in CH₃CN shows the measured spectrum with isotopic distribution pattern. 157

	List of Tables	Page No
1.	Table 2.1. Crystallographic Data for porphyrin 2	77
2.	Table 3.1. Crystallographic data for ZnTANP	106
3.	Table 4.1. Crystallographic data for 3	130
4.	Table 4.2. Fluorescence data ^a of compounds 1-3	134
5.	Table 4.3. UV–Vis data ^a and NLO coefficients ^{a,b}	144
6.	Table 4.4. σ_{TPA} values for related compounds	145

List of Abbreviations

DNA	Deoxyribonucleic acid
DDQ	2, 3-Dichloro-5,6-dicyano benzoquinone
TFA	Trifluoroacetic acid
BF ₃ .OEt ₂	Borontrifluoride diethyletherate
CH ₂ Cl ₂	Dichloromethane
Pd	Palladium
NH ₄ OH	Ammonium hydroxide
H ₂ O	Water
H ₂	Hydrogen gas
R'MgBr	Alkyl magnesium bromide
H ₂ S	Hydrogen sulphide
SnCl ₂	Tin chloride
R'OH	Alcohol
Aq.HCl	Aqueous hydrochloric acid
POCl ₃	Phosphoryl chloride
DMF	Dimethyl formamide
H ₂ SO ₄	Sulphuric acid
HCO ₂ H	Formic acid
NH ₂ OH.HCl	Hydroxylamine hydrochloride
Ni(OAc) ₂	Nickel acetate
AlCl(CH ₃)(NH ₂)	Chloromethylaluminum amide
NBS	<i>N</i> -Bromosuccinamide
CHCl ₃	Chloroform
Pd(PPh ₃) ₄	Tetrakis(triphenylphosphine)palladium(0)

THF	Tetrahydrofuran
HOMO	Highest occupied molecular orbital
LUMO	Lowest unoccupied molecular orbital
UV-Vis-NIR	Ultraviolet-visible-near infrared
ZnP	Zn porphyrin
EtOH	Ethanol
Na(OAc) ₂	Sodium acetate
Co(OAc) ₂	Cobalt acetate
PPh ₃	Triphenyl phosphine
rt	Room temperature
AcOH	Acetic acid
MeOH	Methanol
[bmin][BF ₄]	1-butyl-3-methylimidazolium tetrafluoroborate
EtCN	Propionitrile
NH ₄ Cl	Ammonium chloride
CN ⁻	Cyanide ion
NMR	Nuclear magnetic resonance
nm	Nanometer
Cu	Copper
CDCl ₃	Chloroform-d
CH ₃ CN	Acetonitrile
FTIR	Fourier transform infrared
KBr	Potassium bromide
φ	Quantum yield
ns	Nano-second

CaH_2	Calcium hydride
nJ	Nano joule
KOH	Potassium hydroxide
$\text{Zn}(\text{OAc})_2 \cdot 2\text{H}_2\text{O}$	Zinc acetate dihydrate

CHAPTER 1

Introduction

- 1.1** Porphyrin
 - 1.1.1** General Synthetic Procedures
 - 1.1.2** Cyanoporphyrin
 - 1.1.3** Porphyrin-fullerene dyad
- 1.2** Porphyrin Analogue
 - 1.2.1** Corrole
 - 1.2.2** General Synthetic Procedures
 - 1.2.3** Aromaticity and Planarity
 - 1.2.4** Photophysical Study
 - 1.2.5** Nonlinear Optics
 - 1.2.5.1** Nonlinear Optical Material
- 1.3** Objective of Present Thesis

1.1 Porphyrin

Porphyrins and its analogue are one of the extroverts of nature. They take part in various indispensable biological activities in their metallated form *viz.* heme (Fe complex of porphyrin) in oxygen transport and storage; cytochrome P-450 (Fe complex of porphyrin) for catalysis; vitamin B₁₂ dependent enzymes (cobalt chelated corrin) and chlorophylls or bacteriochlorophyll (Mg complex of chlorophyll and bacteriochlorophyll), involved in the photosynthesis¹ (Figure 1.1). Therefore, numerous synthetic porphyrins and metalloporphyrins were slowly developed to mimic these complex biological processes. Apart from their biological significance, porphyrin has tremendous potentiality over interdisciplinary area such as catalysis, medicine, material science, solar energy conversion, optics, electronics etc. Thus, over few decades porphyrin family gradually became the centre of interest in multidisciplinary area.

The name 'porphyrin' was originated from the Greek word 'porphyrus' which means bright and purple. Basic porphyrin nucleus is a C₂₀ "porphine" core where four pyrrole rings are connected *via* methine bridges (=CH-) in Figure 1.5. Fine tuning of peripheral substituents or suitable metal insertion in the macrocycle can impart ample modification in the photophysics, redox properties, catalytic activity, nature of aggregation and other properties. Although, porphyrin is a planar, 22 π electron system, but only 18 π electrons are in shortest conjugation obeying Huckel's rule of aromaticity (Figure 1.5). This (4n+2) π electron generates a strong ring current throughout the macrocyclic core. Therefore, large magnetic anisotropy due to ring current spreads ¹H NMR spectra of porphyrin over an unusually broad range. For example, highly shielded inner NH protons resonate at very high field where as peripheral protons (protons from the *meso* positions and β positions) appear at very down field.

Porphyrin macrocycle was first characterised by its characteristic optical spectra, as it is a signature of bonding pattern of the macrocycle. Near UV region, a strong and sharp band is observed. This is called Soret or B band. The other four weak bands are called the Q bands. These two types of bands constitute characteristic UV-Vis spectra. Free base porphyrin and

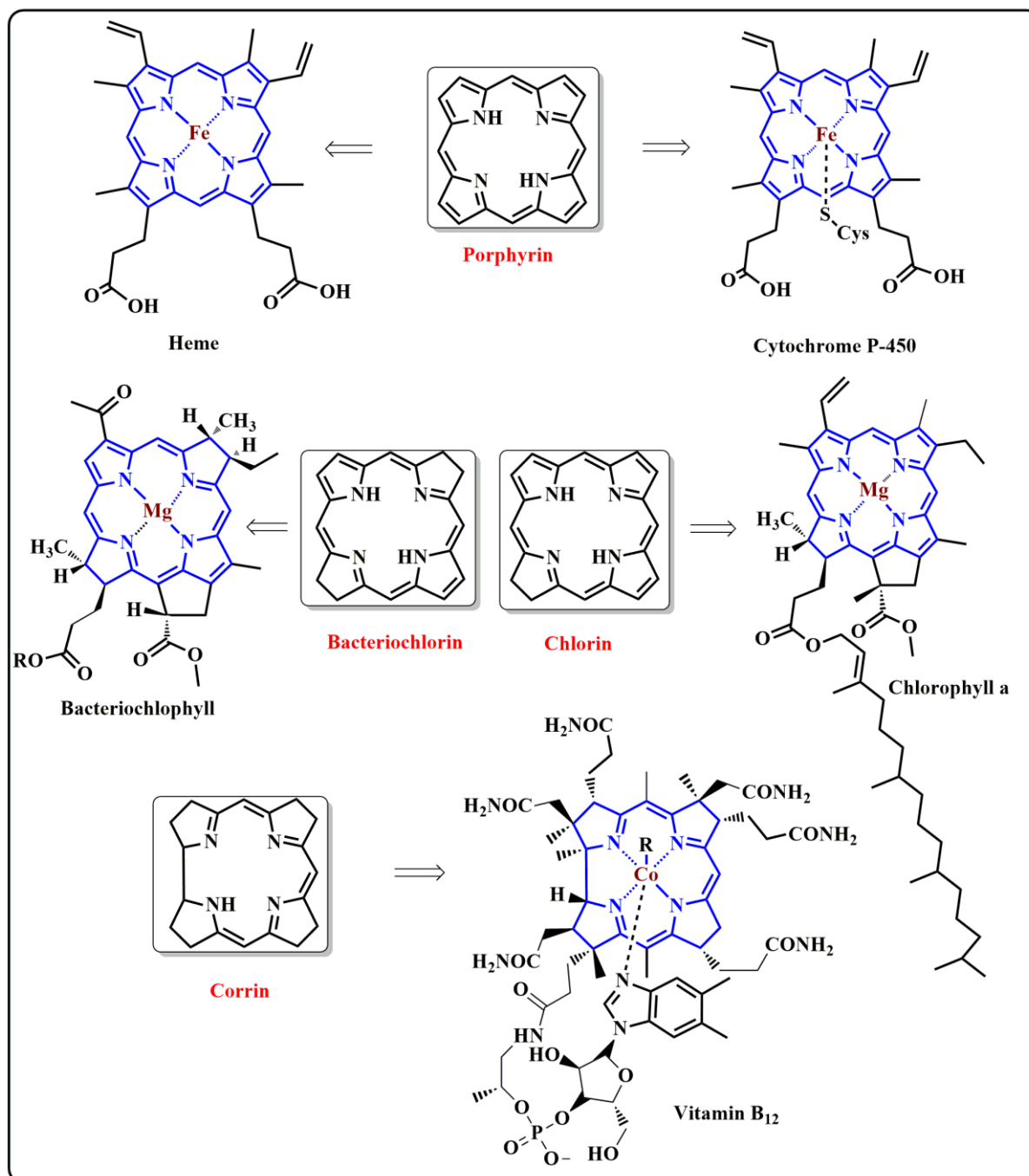
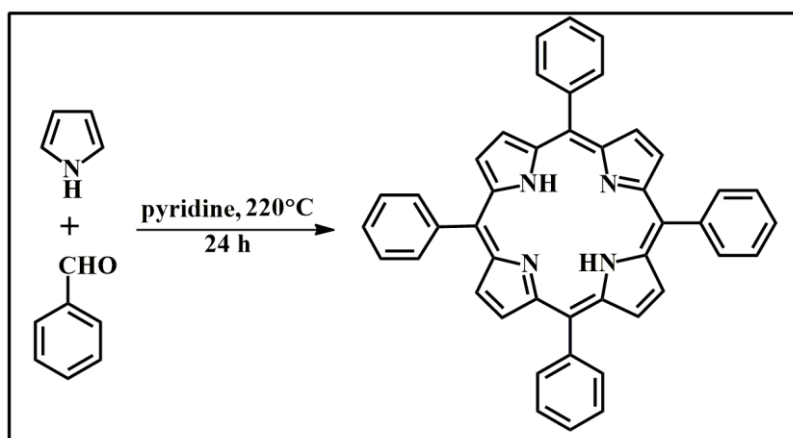


Figure 1.1. Biologically important porphyrin derivative.¹

its metal derivative can be distinguished easily from the optical spectra, as change in symmetry (D_{2h} to D_{4h}) reduces number of Q bands in metalloporphyrin.

1.1.1 General Synthetic Procedures

Initial study by Fischer² and later by Woodward,³ stimulated interesting chemistry behind tetrapyrrole macrocycles. In 1935, Rothmund⁴ reported first synthetic *meso*-substituted porphyrins, by condensing pyrrole and a series of aromatic aldehydes in presence of excess pyridine in a sealed bomb at considerably high temperature without any oxidant (Scheme 1.1). The yield was considerably poor due to harsh reaction condition (10%).

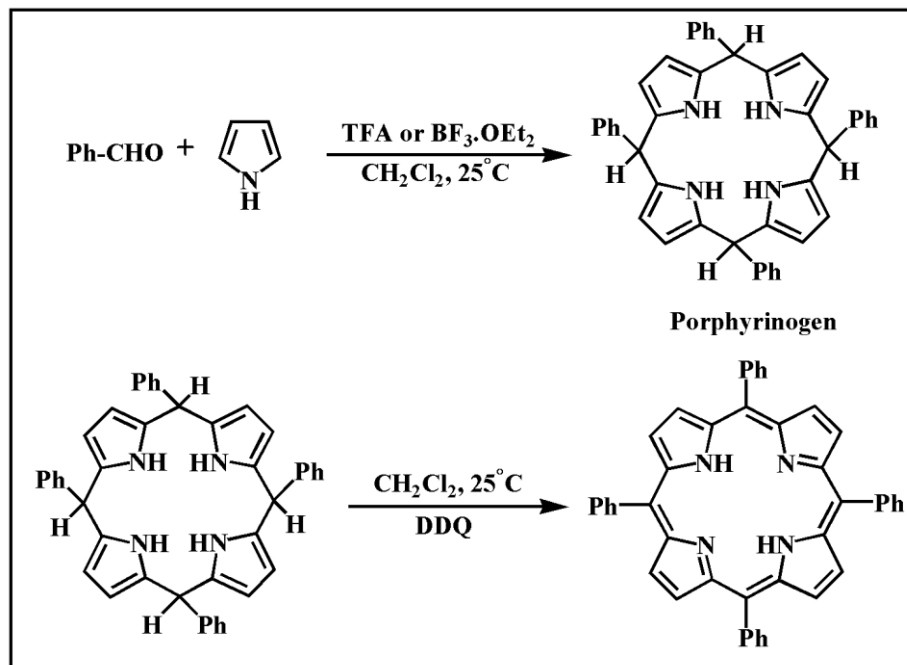


Scheme 1.1. Rothmund synthesis of tetraphenyl porphyrin.⁴

Rothmund strategy was modified by Adler *et al.* in 1967.⁵ They refluxed the mixture of pyrrole and aldehyde in propionic acid under open atmosphere. Till date, it is very amenable methodology to prepare substituted porphyrin in multigram quantity. Adler method is often used for synthesizing unsymmetrically substituted porphyrin. Lavallo *et al.*⁶ followed this protocol for synthesizing cationic porphyrin, which can bind with DNA in the suitable pH range. However, major limitation of using acid sensitive functional group containing aldehyde narrows its application.

Finally, Lindsey *et al.*⁷ developed a two-step one pot synthesis of *meso* substituted porphyrin. It involves condensation of pyrrole and aldehyde (1:1) catalysed by protic or lewis acid under inert atmosphere resulting porphyrinogen intermediate which was immediately

oxidised with *p*-chloranil or DDQ (2.5equiv, Scheme 1.2). This methodology was quite versatile, as a vast range of substituted porphyrin was synthesized under this mild reaction condition with reasonably high yield (30-40%).

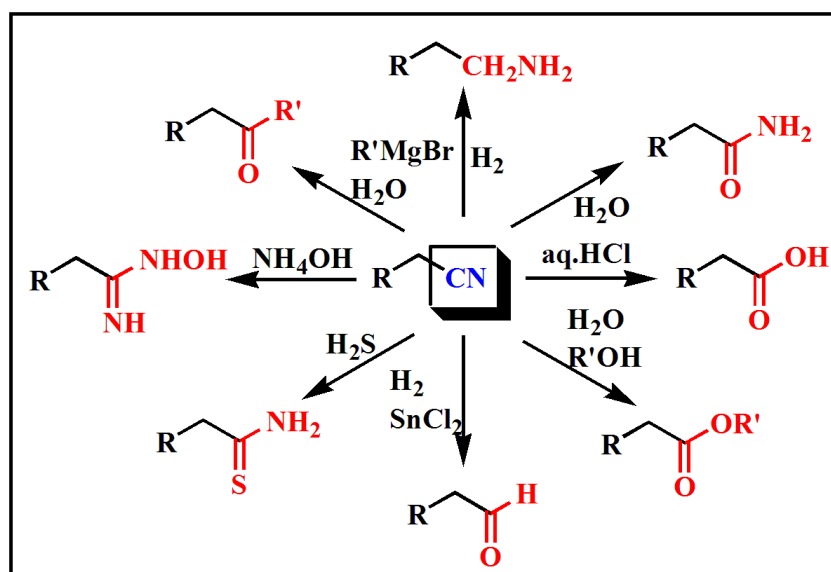


Scheme 1.2. Synthesis of tetraphenyl porphyrin.⁷

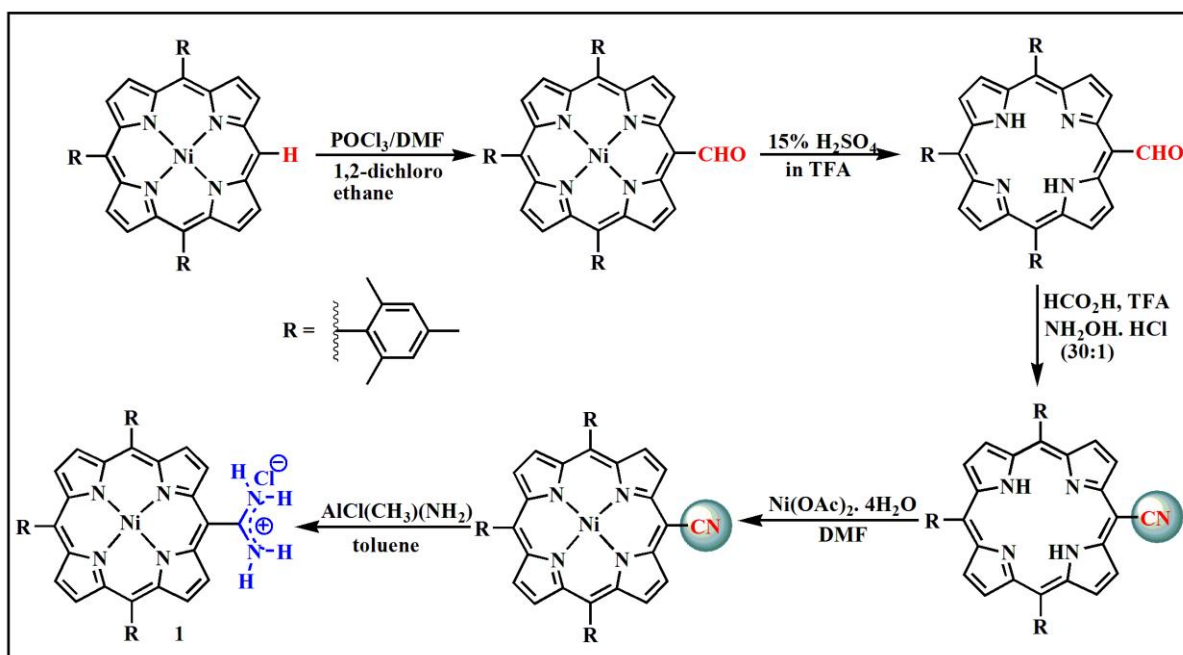
1.1.2 Cyanoporphyrin

It is quite interesting, that change in the peripheral substituent in the porphyrin macrocycle, can synchronize the electronic environment of the macrocycle drastically. A broad spectrum of research groups is actively associated with the synthesis of various substituted porphyrins.⁸ Specifically, Callot *et al.*^{9,10} explained significance of cyano group as substituent over the electronic structure of the tetraphenyl porphyrins (TPP) and ZnTPP. Yokoyama *et al.* utilised the dipole-dipole interaction between cyano groups to generate supramolecular assembly.¹¹ Cyanoporphyrins have excellent application in various field such as versatile catalyst for alkane oxidation.¹² Push-pull type cyanoporphyrins¹³ could have a bright future as field responsive material. Apart from this, cyano group work as an excellent building block for functionalizing molecule^{14, 15} (Scheme 1.3). Therefore, cyano substituted porphyrins are

extremely important as a platform for further synthesis of complex porphyrin molecules¹⁶ (Scheme 1.4).



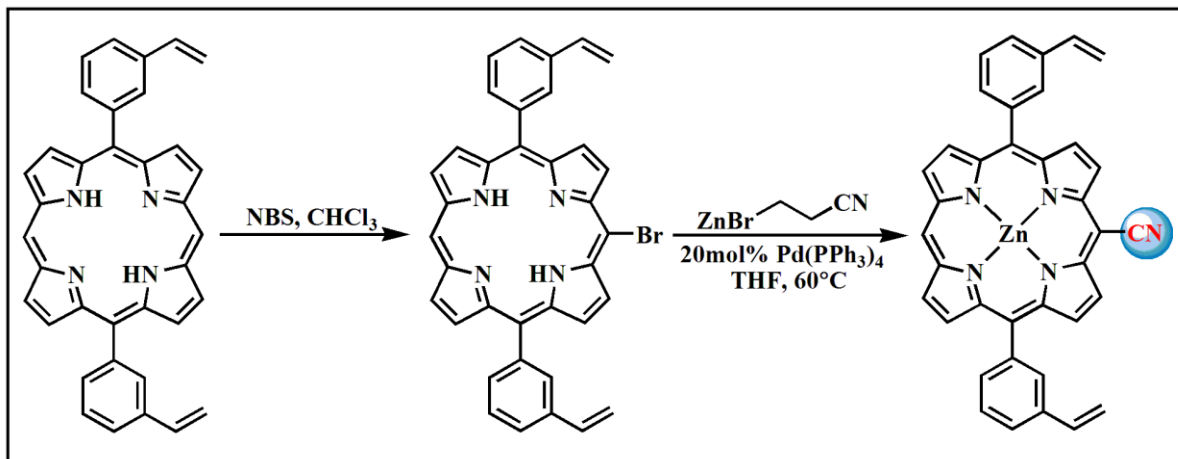
Scheme 1.3. Functionalization of cyano group.¹⁷



Scheme 1.4. Synthesis of the model complex, **1** for arginine-aspartate salt bridge.¹⁶

Hence there is a great demand for the development of synthetic methodologies for the facile synthesis of cyano substituted porphyrins. Several methodology *viz.*, electrochemical cyanation,¹⁸⁻²⁰ Friedel-Crafts cyanation,²¹ Pd catalysed reactions: Suzuki-coupling reactions,

Sonogashira-coupling reactions and Stille-coupling reactions have been employed in this respect.²²⁻³⁹ Generally, all of this protocol involves multistep organic transformation over porphyrin or metalloporphyrin based starting material (Scheme 1.4 and 1.5) and expensive



Scheme 1.5. Cyanation of porphyrin with cyanoethylzinc bromide.⁴⁰

cyanating agent.⁴⁰ Hence, these genuine problems associated with cyano substitution in porphyrin stimulated researchers for further progress in facile synthetic protocol of cyanation in porphyrin macrocycle.

1.1.3 Porphyrin-fullerene dyad

Natural photosynthetic reaction centre based on chlorophyll pigment and quinone, motivated researcher to utilize porphyrin and metalloporphyrin as efficient electron donor in artificial photosynthetic system. On the other side, three dimensional, spherical fullerene works as an excellent acceptor in several area including *n*-type semiconductors,⁴¹ solar cells,⁴² organic field effect transistors,⁴³ superconductor,⁴⁴ and medicine.⁴⁵ Redox-active fullerene can reversibly accommodate upto six electrons in its triply degenerate LUMO under ambient conditions.^{46,47} HOMO-LUMO gap in fullerene is comparable to delocalised π electron systems like porphyrin. Porphyrin/metalloporphyrin and fullerene are known to form potentially useful donor-acceptor pair. They absorb light in broad spectral window of UV-Vis-NIR range. Porphyrin-fullerene separation is close to 2.75Å due to van der Waals force,

operated between curved π surfaces to the planar π surface of porphyrin moiety⁴⁸ (Figure 1.2). Gust and co-workers,⁴⁹ is one of the beginners for developing covalently linked porphyrin-fullerene system where fullerene acts as an electron acceptor. Further DFT calculation revealed that HOMO-LUMO gap in the metalloporphyrin-fullerene complex is highly dependent on central metal ion coordinated to porphyrin.⁵⁰ Moreover, such a donor-acceptor based interaction is highly beneficial for designing modified porphyrin-fullerene dyad with extremely rich physical properties,⁵¹ viz. metallic,⁵² magnetic,⁵³ luminescent⁵⁴ and nonlinear optical (NLO) properties.⁵⁵ Thus covalently linked porphyrin-fullerene dyad has been widely explored as molecular photovoltaic devices. For example, C₆₀-ZnP-ferrocene

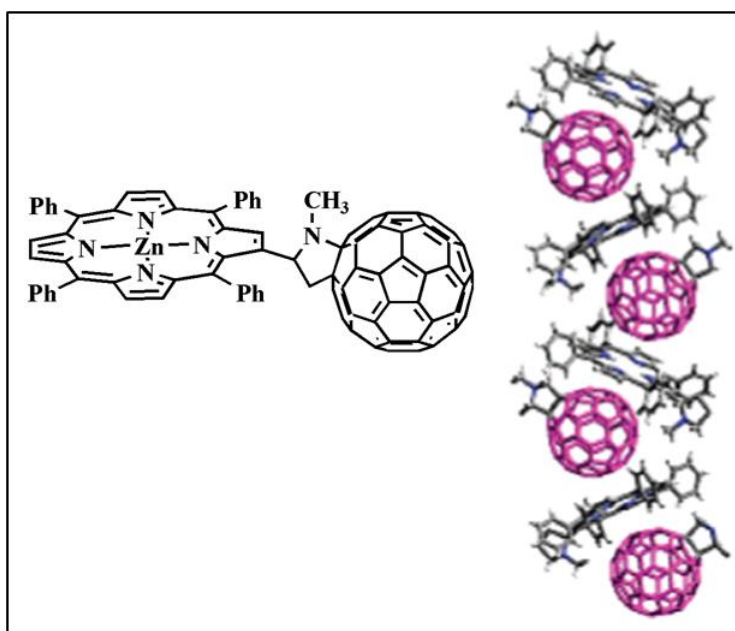


Figure 1.2. The close approach of fullerene to the centre of a porphyrin in the crystal structure.⁴⁸

triad **2** and ZnP-free base porphyrin-C₆₀ triad **3** has been studied intensely as artificial photosynthetic systems (Figure 1.3).^{56,57} Self-assembly of this type of dyad over metal or semiconductor surface, can increase the efficacy of photovoltaic cells to a large extent.⁵⁸ However, observation of fast electron transfer from donor to the acceptor in covalently attached system is relatively difficult. In this respect, non-bonded porphyrin-fullerene dyad

are superior than the covalently linked one.⁵⁹ Some pyridine linked non-covalent supramolecular assembly works as excellent photosensitizer^{58,59} (Figure 1.4).

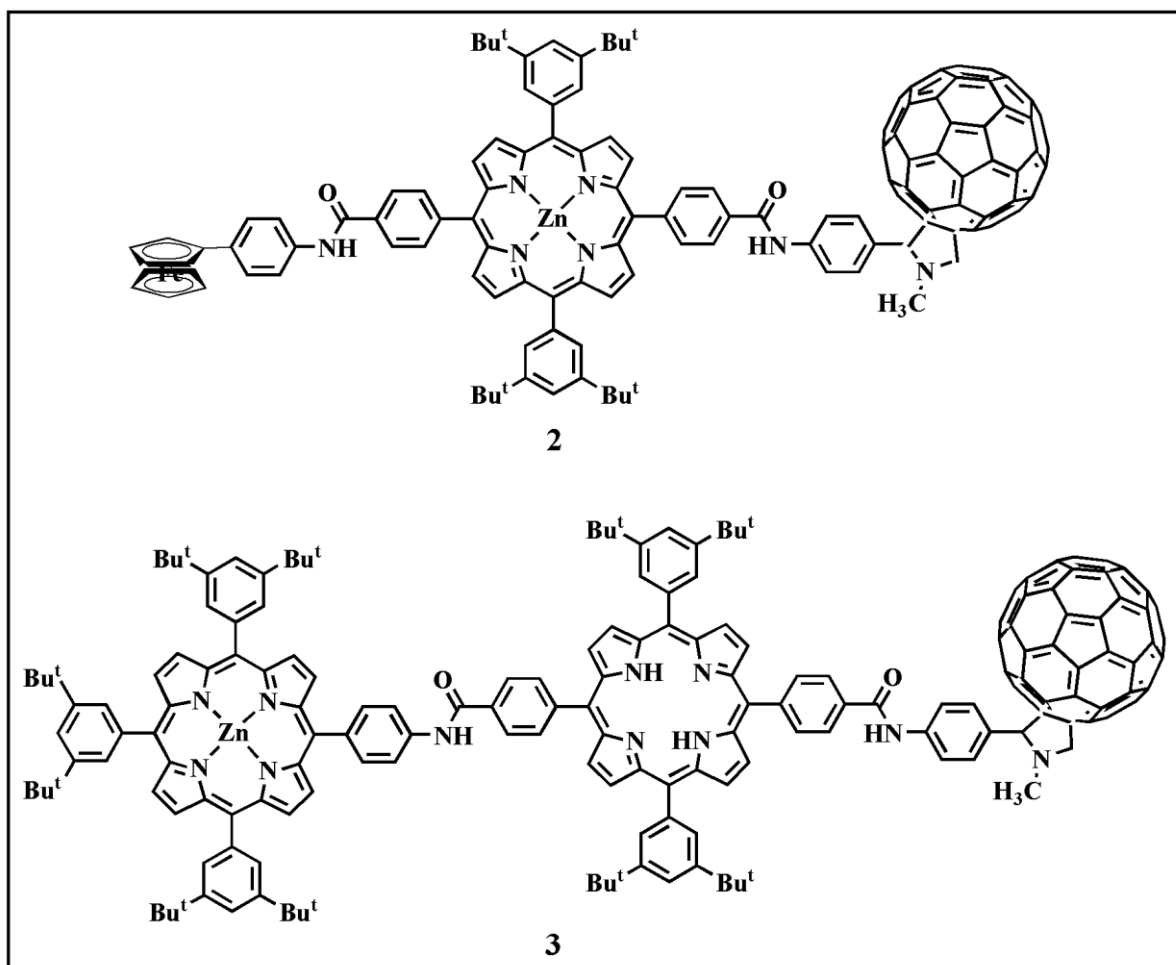


Figure 1.3. Covalently linked porphyrin-fullerene dyad as artificial photosynthetic system.^{56, 57}

But, functionalization in the fullerene moiety reduces electron acceptance capability than pristine fullerene.⁶⁰ Therefore, designing a pure supramolecular assembly of pristine fullerene as acceptor with a strongly electron donor system like porphyrin can improve electron transfer to a large extent. Molecular orientation in the nano-structure is a key element for designing non-covalently attached supramolecular assembly to achieve desired application. Till date, very limited literatures are available about the extremely interesting chemistry associated with non-bonded porphyrin-fullerene dyad. Hence, there is broad scope in future to expand this area with more promising applications.

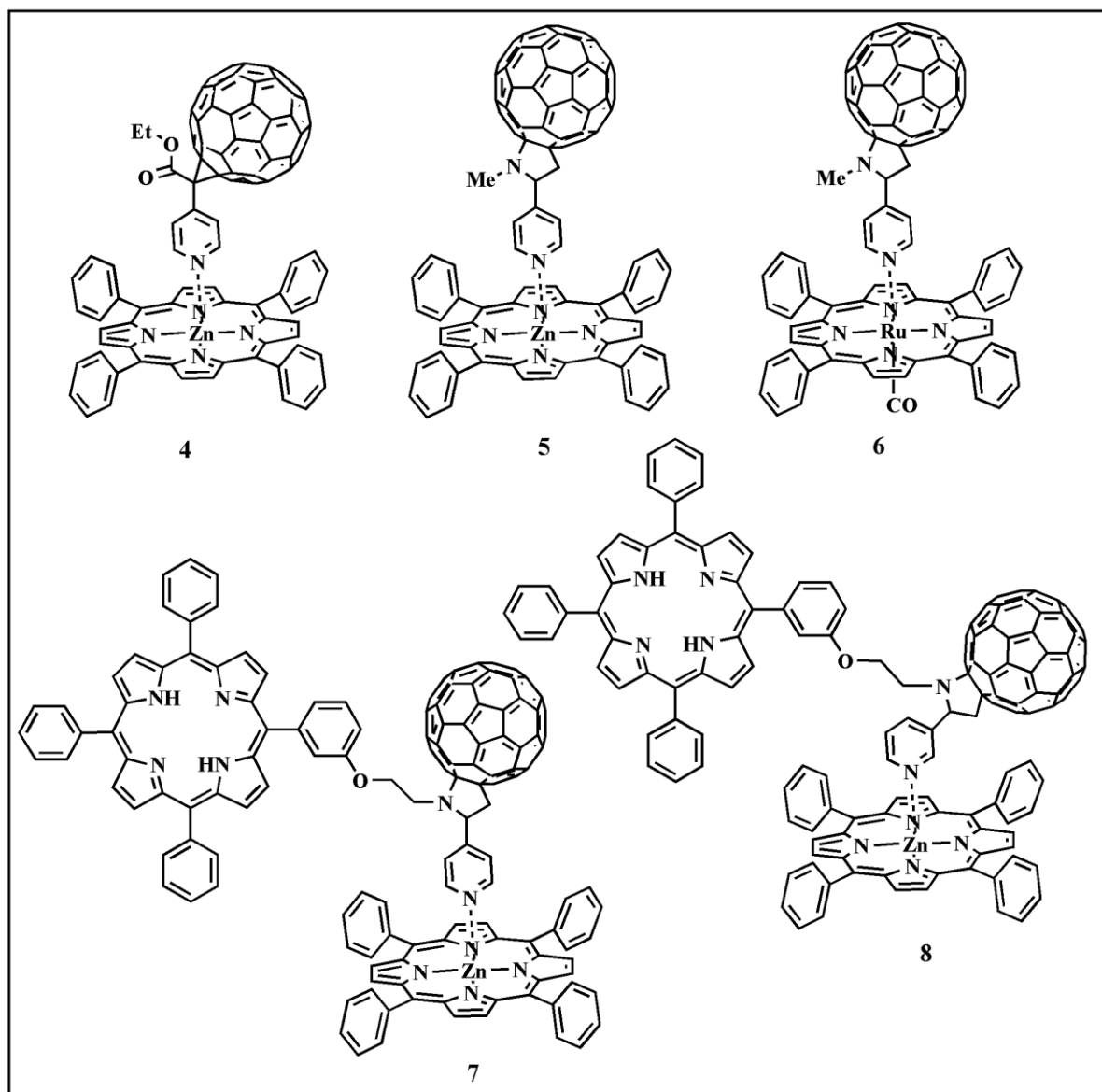


Figure 1.4. Non-covalent supramolecular assembly of porphyrin-fullerene dyad.^{58,59}

1.2 Porphyrin Analogue

1.2.1 Corrole

Over the past decade, research area has expanded over other tetrapyrrole macrocycles, including several core-modified porphyrinoid.⁶¹ Among these, corrole (Figure 1.5) has attained considerable interest due to the close resemblance with the corrin ring (Figure 1.1 and 1.5) in vitamin B₁₂. It is an intermediate structure between porphyrin and corrin with a direct bipyrrole link between two pyrrole rings. But, corroles are 18 π aromatic system with three ionisable NH protons, while corrins are 12 π half-aromatic systems with only one

ionisable NH proton. Therefore, from the aspect of aromaticity and other physical properties, corrole is closely related to porphyrin (Figure 1.5). These trianionic corrole are of smaller cavity size in fully deprotonated form and stronger σ donor compared to porphyrin.

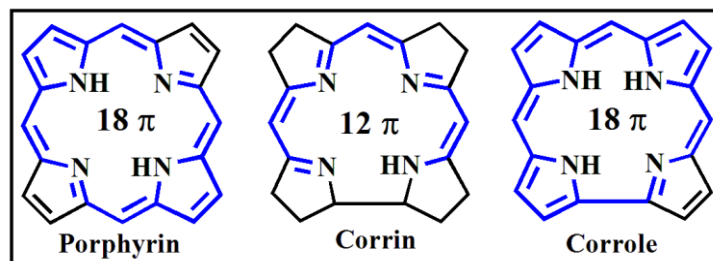


Figure 1.5. Basic difference of aromaticity in the porphyrin, corrin and corrole macrocycles. Aromatic path is shown in *dark blue*.⁶²

Vogel *et al.*⁶³, first demonstrated that due to these structural advantages, corrole can stabilize the unusually high oxidation states of metal ions which enriched corrole chemistry. Aviv-Harel and Gross,⁶⁴ in 2009 published a brief review about some excellent application of corroles and their derivatives. Later, Palmer *et al.*⁶² published a concise report regarding first row transition metal corrole complexes and their application in catalysis. Recent advancement till date about several alkali metals, early transition metals, lanthanides, and actinides has been added by Arnold and co-workers.⁶⁵ Apart from this rich coordination chemistry and their immense potential, free base corrole itself is a good candidate in multiple area. Specially designed sol-gel capsulated 10-(4-aminophenyl)-5,15-dimesitylcorrole based optode⁶⁶ is a promising candidate against conventional pH sensor. *N*-alkylated, water soluble corrole,⁶⁷ **9** (Figure 1.6) was first employed as corrole based anti-cancer drug. Another important corrole based liquid membrane electrode can easily identify phenol isomers in aqueous-organic inter phase.⁶⁸

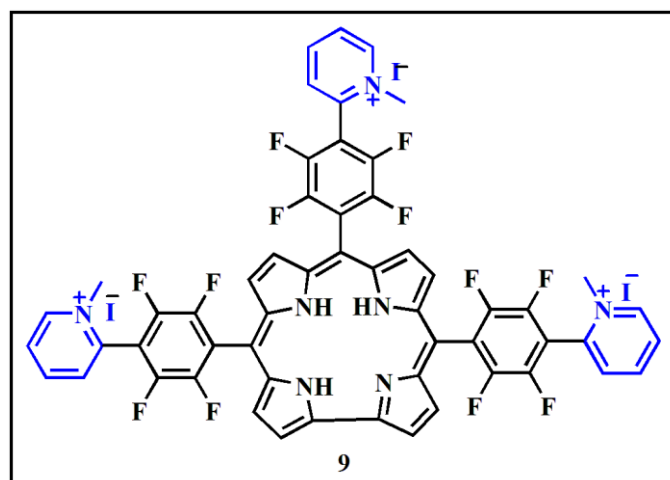
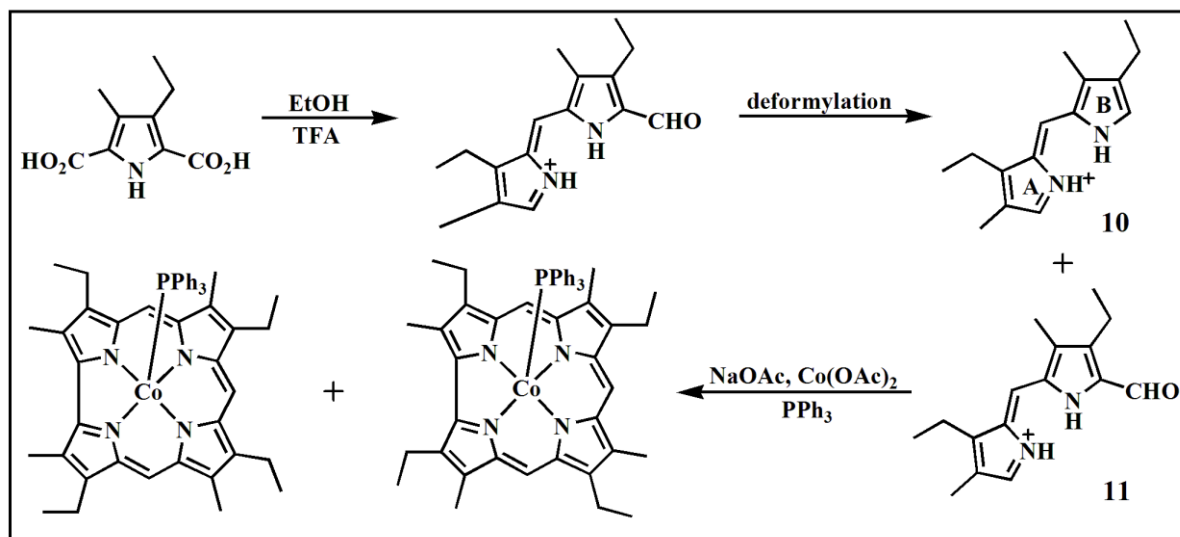


Figure 1.6. Water soluble corrole **9**, first corrole based medicinal approach by Gross *et al.*⁶⁷

1.2.2 General Synthetic Procedures

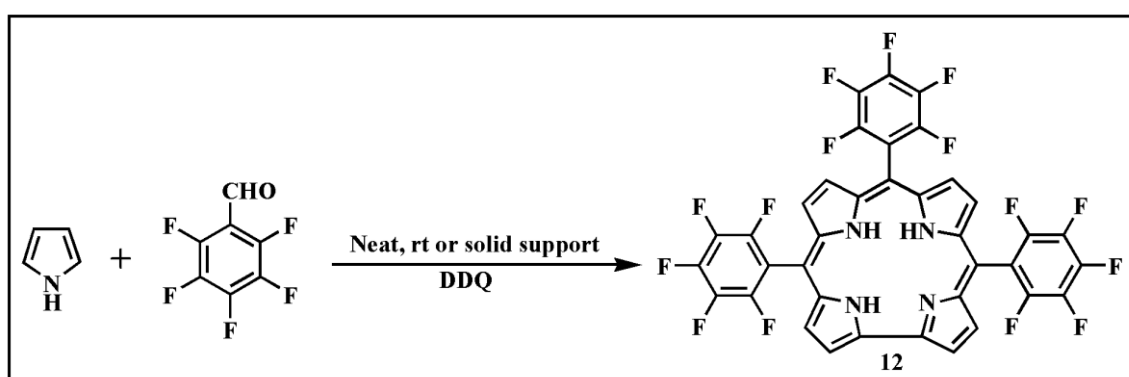
Johnson and Kay, synthesized corrole as a model complex to mimic enzymatic activity of vitamin B₁₂.^{69,70} Later, Hodgkin and co-workers, deciphered crystal structure of vitamin B₁₂, and simultaneously reported the first X-ray structure of a metal free corrole derivative.⁷¹ These pioneer work, including detailed progress of synthesis of corroles and its metal derivatives, upto 1999, are well depicted in several reviews and book chapters.⁷² This explains that the potentiality of corrole chemistry was largely overshadowed by its porphyrin counterpart due to lack of facile synthetic protocol of corrole.

Paollesse *et al.*^{73,74} reported for the first time, that the template effect of cobalt ion can trigger one pot synthesis of contracted corrole ring from acid substituted pyrrole (Scheme 1.6). Here, deformylation step generates a α -free dipyrromethene, **10** which further condenses with a dipyrromethene aldehyde, **11** and results cobalt complex of corrole (10%). However, major drawback of this protocol is only cobalt metal and substituted pyrrole can drive synthesis and fully substituted cobalt derivative is the sole product.



Scheme 1.6. Synthesis of Co-corrole metal complex by Paolesse *et al.*⁷⁴

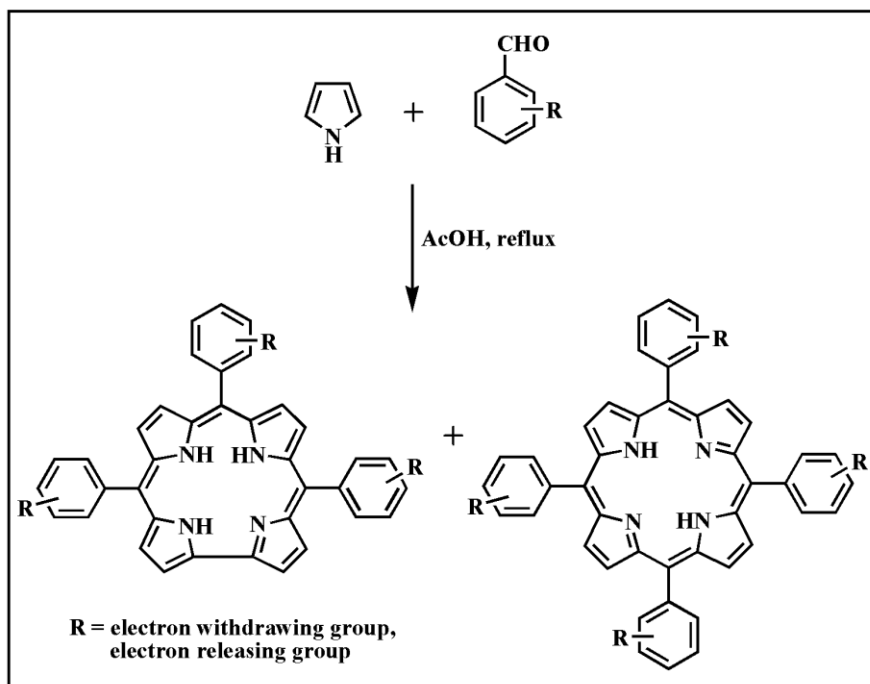
In 1999, Gross *et al.*⁶⁷ explored a solvent free condensation of pyrrole and aromatic aldehyde (1:1) on a solid support like alumina, without any catalyst. Further oxidation with DDQ (0.5equiv) resulted 5,10,15-tris(pentafluorophenyl)corrole **12**, (Scheme 1.7). Major bottleneck of this methodology is the requirement of highly reactive aldehyde as less reactive aldehydes resulted only porphyrin. Ghosh and co-workers⁷⁵ also reported similar corrole synthesis with *p*-tolualdehyde. But, they did not provide any reaction conditions or physical characterization of the corrole.



Scheme 1.7. Synthesis of 5,10,15-tris(pentafluorophenyl) corrole, **12** by Gross *et al.*⁶⁷

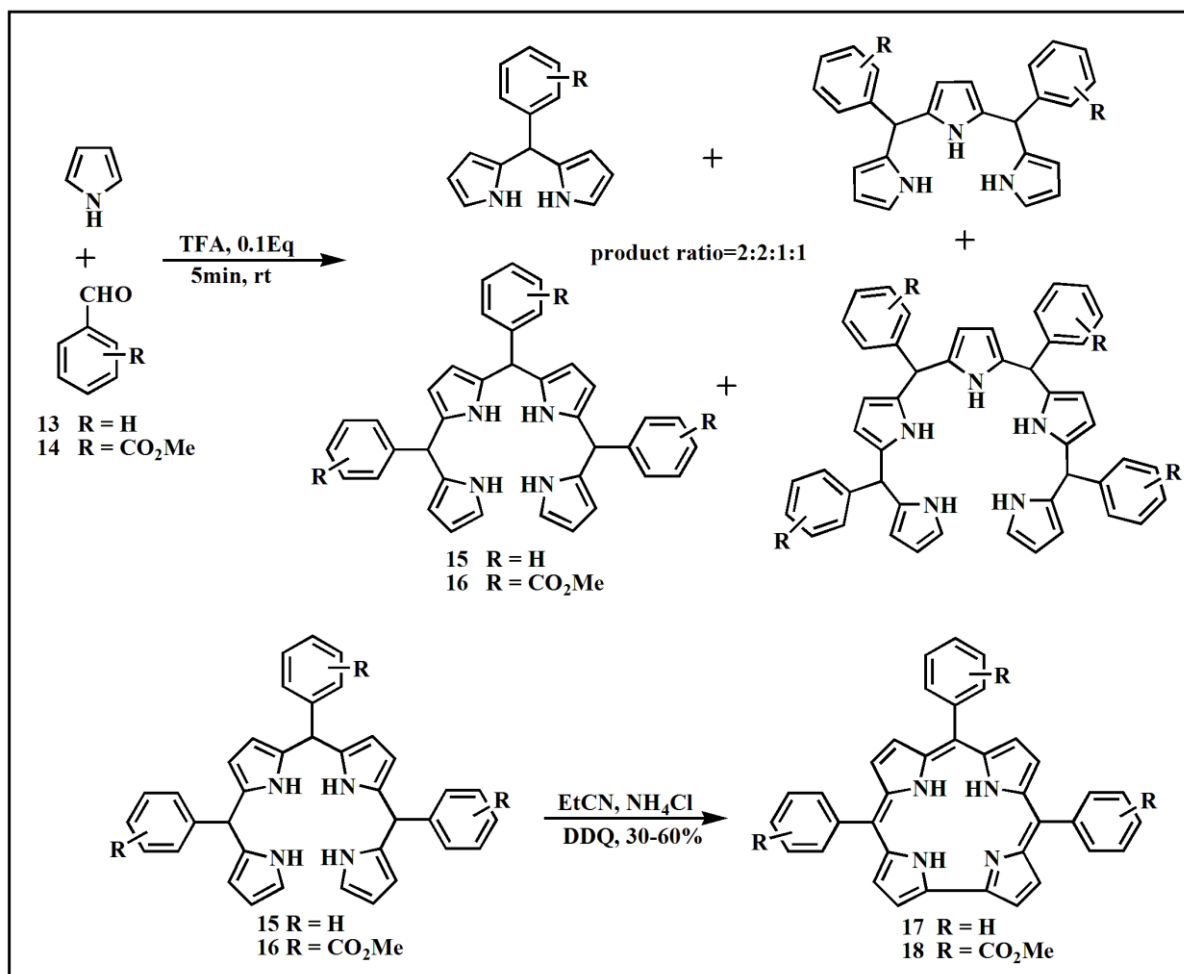
At the same time, Paolesse *et al.*⁷⁶ found that a simple modification of Adler Longo conditions can change the yield of corrole to a large extent. They altered the molar ratio of pyrrole to aldehyde (3:1) and replaced propionic acid by acetic acid (Scheme 1.8). This

methodology is of quite synthetic value as numerous aldehydes with either electron-donating or electron-withdrawing substituents were successfully incorporated. Major drawback includes, sterically hindered corroles cannot be synthesized following this method and porphyrin yield was almost equivalent to corrole yield (6%). Furthermore, only few aldehydes were stable in boiling acetic acid.



Scheme 1.8. Synthesis of *meso* substituted corrole by Paolesse *et al.*⁷⁶

Gross *et al.* postulated that bilanes are the possible precursor of corrole. Keeping this in mind, Lee and co-workers⁷⁷ isolated bilane (5,10,15,20,22,23-hexahydro tetrapyrin), from the TFA catalysed reaction of an aromatic aldehyde with excess pyrrole (3:1), under neat condition (**15** and **16** in Scheme 1.9). They purified bilane for the first time. Finally radical macrocyclization of bilane with DDQ yielded corrole (**17** and **18** in Scheme 1.9). However, they didn't mention the total yield of the synthesized corrole. Limitations associated with this protocol, was modified and extended to other aldehydes by Collman *et al.*⁷⁸ They replaced thermal heating with the microwave irradiation to reduce the by-product leading to a considerable increase in the yield.

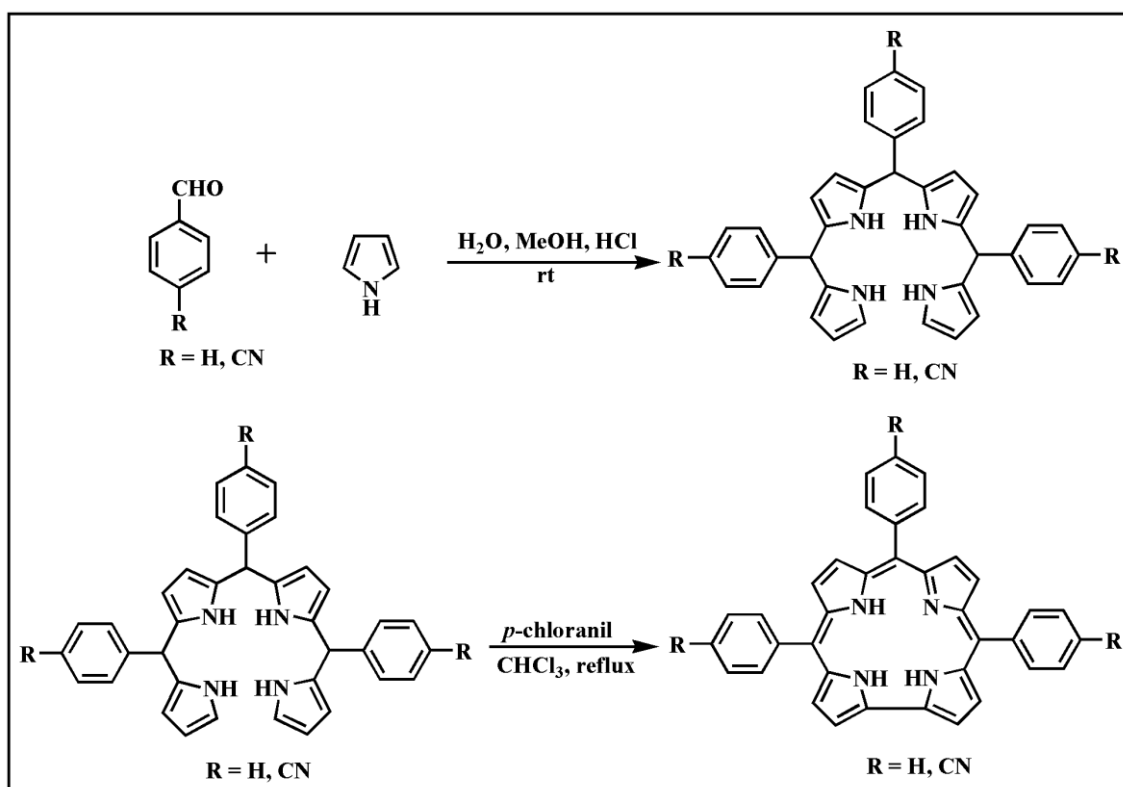


Scheme 1.9. Synthesis of *meso* substituted corrole by Lee and co-workers.⁷⁷

After easy accessibility and proper characterization of A₃ type corrole, more complex unsymmetrical corrole synthesis was the next target. In this respect, Gryko *et al.*⁷⁹ first reported a simple two step procedure of *meso* substituted A₂B type corrole bearing one fluorinated substituent. Although it was a non-catalysed condensation of dipyrromethane and reactive aldehyde, careful observations found that trace amount of acid present in the aromatic aldehyde catalyses the first step. At the same time, Bruckner and co-workers⁸⁰ performed TFA catalysed condensation of aldehydes with excess sterically unhindered dipyrromethane (near six fold) and obtained *trans*-A₂B corrole in 20-40% yield. Dehaen and co-workers.⁸¹ also reported same protocol with highly reactive aldehydes and TFA was replaced by BF₃.OEt₂. Extensive modification of this [2+1] approach was quite successful for

installing basic nitrogenous group bearing substituent in the *meso* position of the macrocyclic ring.

Kral *et al.*⁸² previously described synthesis of dipyrromethane in water. They clearly mentioned that addition of methanol in reaction mixture can cut down yield of dipyrromethane. Inspired by their work, Gryko and co-workers⁸³ optimized several reaction condition including solvents, concentration and oxidant. Finally, they established one-pot, two step synthesis of *meso*-substituted A₃-corroles and *trans*-A₂B corrole from aldehydes and pyrrole condensation (Scheme 1.10). The first step is the acid-mediated aldehyde-pyrrole (1:2) condensation in water-methanol (1:1) resulting various oligocondensate. This key step



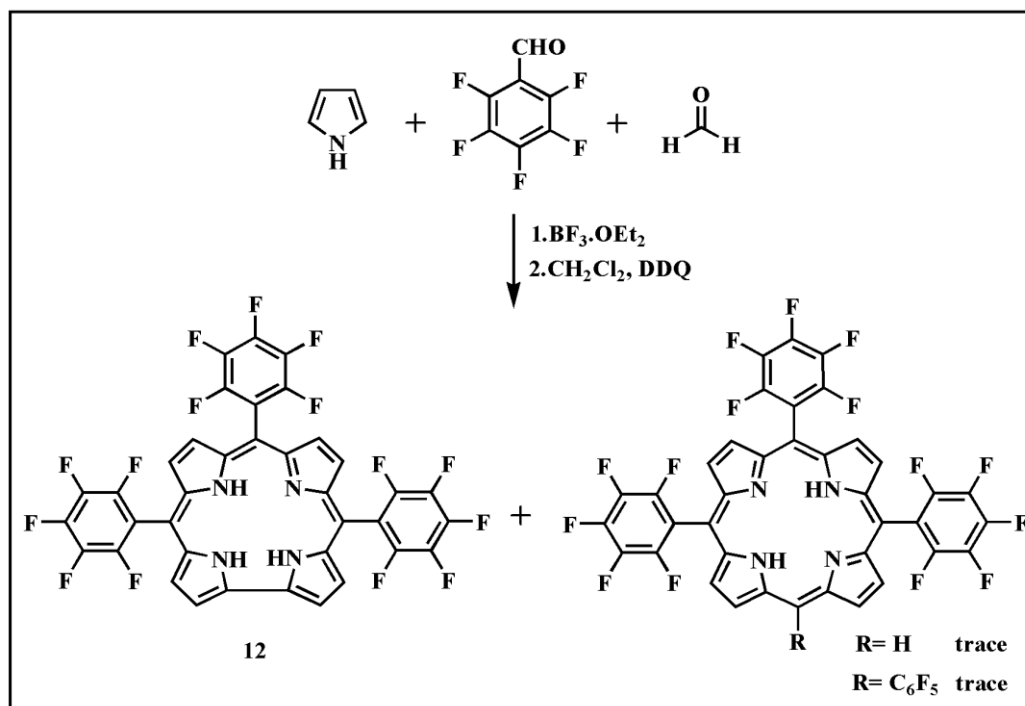
Scheme 1.10. Triaryl corrole synthesis by Gryko method.⁸³

was well optimized to yield bilane (direct precursor for corrole) as major product over other higher oligocondensate. Second step proceeds through oxidative ring closure of bilane by *p*-chloranil (1 equiv.). Here, *p*-chloranil was favoured over DDQ for mild reaction condition as well as to minimize yield of porphyrin. Their discovery of facile procedure leads to

breakneck pace over the last decade. But still there are some challenges in the corrole synthesis as yield of corrole is quite low unlike porphyrin and highly dependent on the nature of aldehyde used. To overcome these problems, further improvement to the old one as well as new attempt is under progress.

Among the different approaches from other group, Kumari and Chauhan reported one environment friendly synthetic protocol with considerably high yield.⁸⁴ They carried out Amberlyst 15 catalysed condensation of pyrrole and aromatic aldehyde under solvent free condition followed by oxidation with DDQ in room temperature. Use of ionic liquid [bmim][BF₄]⁸⁵ as solvent is another promising greener approach to overcome the problems associated with corrole synthesis.

Recently Nocera and co-workers⁸⁶ reported synthesis of corrole, **12** by condensation of pyrrole, pentafluorobenzaldehyde and paraformaldehyde (16:1:15) following Lindsey method (Scheme 1.11). Although, the role of paraformaldehyde is not precisely defined but it



Scheme 1.11. Synthesis of 5,10,15-tris(pentafluorophenyl)corrole by Nocera and co-workers.⁸⁶

is postulated that it can control the formation of bilane which upon further macrocyclization with DDQ results corrole. Absence of paraformaldehyde yields porphyrin only. Major advantage of this process is the ease of scale up to a large extent.

1.2.3 Aromaticity and Planarity

Corrole nomenclature is similar to porphyrin nomenclature (Figure 1.7). It has surprisingly acidic NH protons compared to other porphyrinoid macrocycles. Specially, free base corrole,

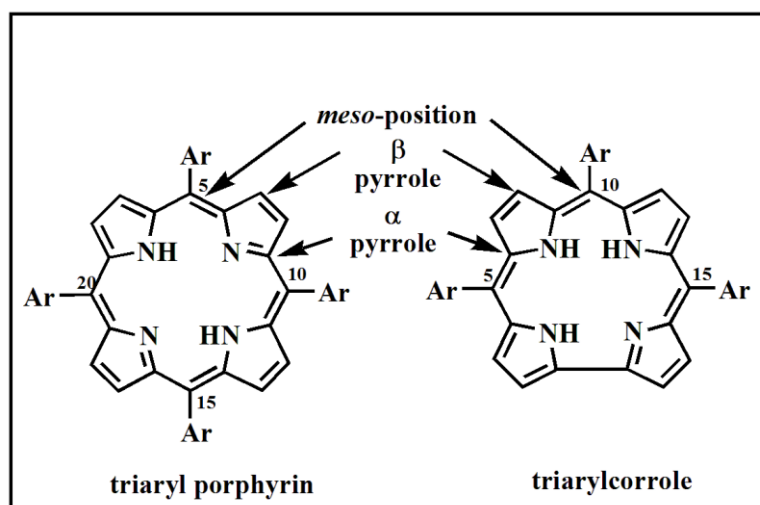
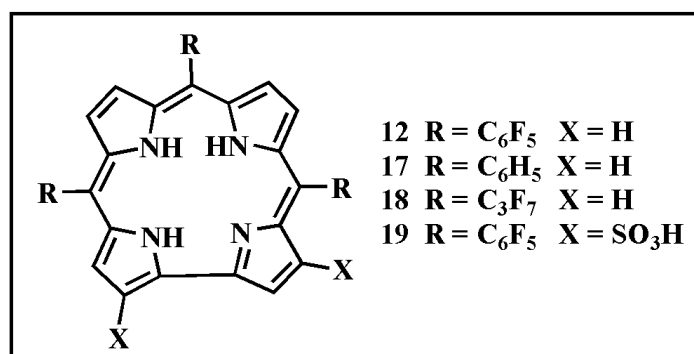


Figure 1.7. The general substitution pattern of tetraaryl porphyrins and triarylcorroles, $H_3(tpc)$ (Ar = C_6H_5 , **17**).

12, 17-19 of Scheme 1.12 shows spontaneous conversion to its monoanionic form in weakly basic solvents such as DMF or ethanol.^{67,87} This high NH acidity is well explained by the



Scheme 1.12. Structure of corrole **12, 17-19**.^{67, 87}

structural analysis of 5,10,15-triphenyl corrole,⁸⁸ **17** in Figure 1.8. At low temperature, exact location of the entire hydrogen atom can be obtained from X-ray crystal structure (Figure

1.8). This clearly shows distortion in the planarity of the macrocycle minimizes the steric hindrance between the three NH protons in the contracted N4 coordination core. Additionally, the NH proton of ring A is situated perpendicular to its own pyrrole skeleton. Thus the release of large steric strain upon deprotonation is the driving force behind high NH acidity of corroles. This non planarity of macrocycle, makes tetrapyrrole rings in corrole, asymmetric unlike porphyrin tetrapyrrole rings (Figure 1.9). Energetically different but similar two tautomers are present unlike energetically similar stable porphyrin tautomers. ^1H NMR spectra⁸⁹ shows unusual broad signal for NH proton at ambient temperature due to two basic

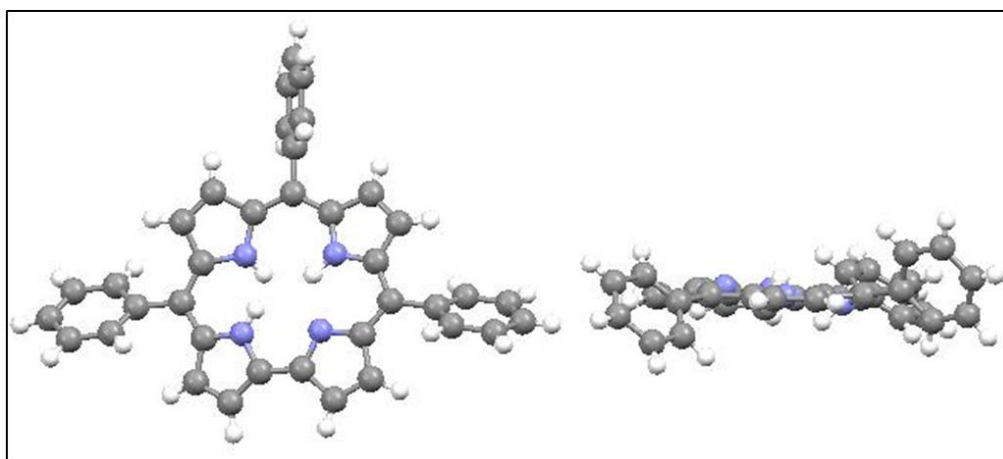


Figure 1.8. Top and side view models of the X-ray structure of corrole 17.⁸⁸

reason *i.e.*, strong NH acidity and dissimilarity between tautomers. The inner NH protons rapidly exchange position within the ring, which can be identified at low temperature ^1H NMR experiment.

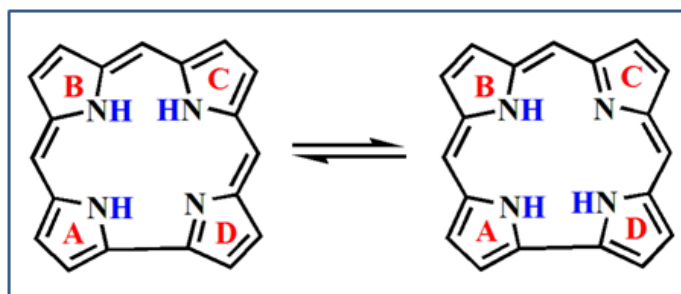


Figure 1.9. Tautomerism between two non-equivalent corrole tautomers.⁸⁸

1.2.4 Photophysical Studies

Photophysical properties of corrole are extremely interesting and intensively investigated. Corrole exhibits more red-shifted, very intense Soret type transitions near 300-400 nm region and less intense Q-bands in 600-700nm, compared to its porphyrin analogue. However, these Soret band as well as Q bands is highly susceptible to change in solvent and peripheral substituent. Metal complexes of corrole shows similar type of spectra like metalloporphyrin.

Free base corroles and its main group metal derivatives is highly fluorescent molecule compared to other porphyrinoid macrocycles. Reduced symmetry of the macrocycle (D_{4h} to C_{2v}) and lack of inversion centre changes the degeneracy of the molecular orbital which in turn results small quantum efficiency of S_2 - S_1 internal conversion, long-lived excited triplet state with strong intersystem crossing.⁹⁰ These parameters inherently increase two photon absorption (2PA) of corrole macrocycle.

1.2.5 Nonlinear Optics

The field of nonlinear optics started its journey in 1875 with the Kerr Effect. Franken et al.,⁹¹ in 1961, made a drastic change in this field with the observation of second harmonic generation. Nonlinear optics is basically expansion of conventional linear optics fostered by laser technology. Generally, very intense coherent light (laser), impart changes in the polarizability of the molecule. Such induced polarizability, \mathbf{P} in microscopic level is expressed by

$$\mathbf{P} = \alpha\mathbf{E} + \beta\mathbf{E}\mathbf{E} + \gamma\mathbf{E}\mathbf{E}\mathbf{E} \quad (1.1)$$

Here α = linear effects

β = Second order hyper polarizability (second order nonlinear effect)

γ = cubic hyper polarizability (third order nonlinear effect)

For small field last two terms are negligible thus linear behavior is observed.

Induced polarization, \mathbf{P} at macroscopic level is given by

$$P = \chi^{(1)}\mathbf{E} + \chi^{(2)}\mathbf{E}\mathbf{E} + \chi^{(3)}\mathbf{E}\mathbf{E}\mathbf{E} \quad (1.2)$$

Here $\chi^{(1)}$ is the linear susceptibility. $\chi^{(2)}$ and $\chi^{(3)}$ are the second order and third order susceptibility.

At macroscopic level, for centrosymmetric molecule, linear behavior is seen. $\chi^{(2)} \neq 0$, when the interacting molecule is either non-centrosymmetric or high β value due to the attachment of highly conjugated donor/acceptor group with the molecule.

1.2.5.1 Nonlinear Optical Material

Initially, conventional inorganic materials such as quartz, KH_2PO_4 , lithium niobate, CdS, CdSe, CdTe, semiconductors was mostly examined for checking nonlinearity in the medium. But organic materials and organometallic complexes^{92, 93} based NLO application has vast advantage over inorganic solid as they satisfy the primary requirement such as (i) low dielectric constant thus fast nonlinear response time (ii) low threshold intensity (iii) fast response time (iv) non-centrosymmetric molecule (v) fine tuning of the photophysical properties over a broad spectral window by simple structure variation and (vi) easy device fabrication. Therefore, these materials are rapidly replacing inorganic NLO materials.

Most precisely, present optical technology is highly dependent on NLO material with high optical limiting ability. Optical limiting can be defined as when a material is apparently transparent under low light intensity but above the threshold intensity, material completely ceases transmitting light through it (Figure 1.10). A good optical limiter relies on reverse saturable absorption (RSA). This RSA process is that, there must be large excited absorption cross section (σ_{ex}) compared to ground absorption cross section (σ_{g}). Thus with increase in the optical intensity, population in the excited state increases.

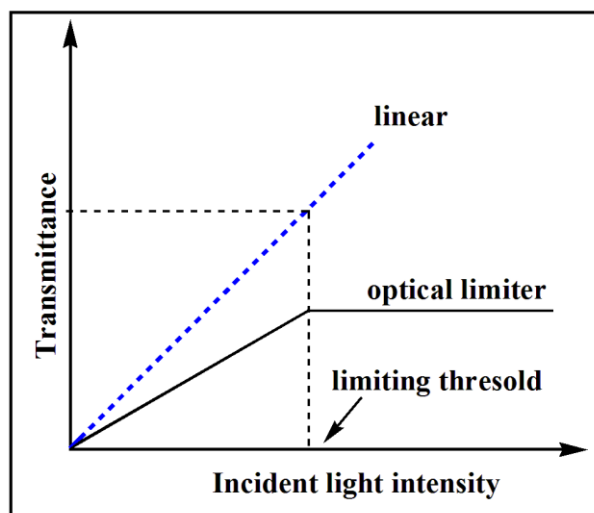


Figure 1.10. Transmittance vs. Incident light intensity for linear and optical limiting material.⁹⁴

Optical limiters are of immense importance for protecting sensors and human eye. Tetrapyrrolic macrocycle such as porphyrin,⁹⁴ phthalocyanin,⁹⁵ naphthalocyanin,^{96,97} efficiently work as optical limiters in the mid-visible region. However, unique photophysical properties and other parameters strongly support that corrole could be an excellent optical limiter. But, compared to other porphyrinoid materials NLO properties of corrole are investigated very recently.^{98,99} Therefore, proper designing of new corrole molecule will generate more interesting result.

1.3 Objective of Present Thesis

Chapter 1 gives a short introduction about porphyrin and corrole derivative. Beginning of the porphyrin chemistry, problems associated with the synthesis and its genesis till date, were discussed elaborately. Although, coordination chemistry as well as potential application of porphyrin derivative is extensively investigated over past few decades still development of new synthetic protocol as well as expansion over interdisciplinary area is very challenging.

Vitamin B₁₂ chemistry inspired researches to move into corrole chemistry. Eventhough, this macrocycle overcame its synthetic obstacles only fifteen years ago, corrole chemistry is rapidly expanding over various multidisciplinary areas. Brief literature survey

reveals remarkable photophysical property, high NH acidity, stabilisations of metals in unusually high oxidation state, highly reactive low valent metallocorroles as well as diverse potential application has made corrole a superior candidate over its porphyrin counterpart. Still application in optical communication, sensor is quite unexplored. Henceforth, there is a broad scope of work with free base corrole as its metal derivative.

Chapter 2 describes a very novel synthetic methodology of *meso*-cyanoporphyrins. Cyanoporphyrins are building block of numerous complex molecules due to easy transformability of cyano group. Literature study reveals that cyanoporphyrin synthesis requires porphyrin based starting material along with multi step synthesis, harsh reaction condition. Herein, we have developed two novel cyanoporphyrin along with one representative crystal structure and spectroscopic features. First of all, this protocol does not need any porphyrin or metalloporphyrin based starting material. Secondly, it's a two-step one pot synthesis using DDQ as cyanation reagent. We have also explained the probable mechanism with the help of GC-mass analysis of the reaction intermediates.

Chapter 3 deals with synthesis of a hybrid material, from a novel Zn-porphyrin complex and C₆₀ fullerene and its application. A series of spectroscopic methods were performed to confirm the existence of a charge transfer based complex between Zn-porphyrin and C₆₀. Circular discs like nano-objects were generated from this D-A based system. We have fabricated a porphyrin (D)-fullerene (A) based nano-architecture to a metal-insulator-semiconductor (MIS) diode with potential application as charge storage device. Current-voltage (*I-V*) and the capacitance-voltage (*C-V*) analyses of the diode were performed. The crucial roles of the Ag-C₆₀-Zn-porphyrin and C₆₀-Zn-porphyrin-SiO_x interfaces are clearly understood from the *I-V* characteristic of the present device. Existence of a hysteresis loop in the *C-V* plot indicates that the device is indeed suitable for charge storage applications.

Chapter 4 describes synthesis of two novel *trans*-A₂B corrole and one A₃ type corrole and application in high speed communication technology. Several spectroscopic techniques along with one representative X-ray crystal structure are done to characterize them. Self-aggregates of these corroles were generated on a silica wafer as well as quartz substrate by simple drop casting method. These self-aggregates were characterized by SEM technique. Further measurement of NLO properties (nonlinear refractive index, n_2 ; two-photon absorption coefficient, β) of these corrole in solution state as well as in solid aggregates reveal that one of the corrole has reasonably high n_2 , β which can be promising candidate for the devising optical switch.

References

1. Milgrom, L. R., *The colours of life : an introduction to the chemistry of porphyrins and related compounds*. Oxford University Press: Oxford, **1997**.
2. Fischer, H.; Zeile, K., *Liebigs Ann. Chem.*, **1929**, 468, 98-116.
3. Woodward, R. B.; Ayer, W. A.; Beaton, J. M.; Bickelhaupt, F.; Bonnett, R.; Buchschacher, P.; Closs, G. L.; Dutler, H.; Hannah, J.; Hauck, F. P.; Itô, S.; Langemann, A.; Le Goff, E.; Leimgruber, W.; Lwowski, W.; Sauer, J.; Valenta, Z.; Volz, H., *J. Am. Chem. Soc.*, **1960**, 82, 3800-3802.
4. Rothmund, P., *J. Am. Chem. Soc.*, **1935**, 57, 2010-2011.
5. Adler, A. D.; Longo, F. R.; Finarelli, J. D.; Goldmacher, J.; Assour, J.; Korsakoff, L., *J. Org. Chem.*, **1967**, 32, 476-476.
6. Lavalley, D. K.; Xu, Z.; Pina, R., *J. Org. Chem.*, **1993**, 58, 6000-6008.
7. Lindsey, J. S.; Schreiman, I. C.; Hsu, H. C.; Kearney, P. C.; Marguerettaz, A. M., *J. Org. Chem.*, **1987**, 52, 827-836.
8. Kadish, K. M.; Smith, K. M.; Guillard, R., *The Porphyrin Handbook*. Academic Press: San Diego, **1999-2003**; vol. 1-20.
9. Callot, H. J., *Tetrahedron Lett.*, **1973**, 14, 4987-4990.
10. Callot, H. J., *Bull. Soc. Chim. Fr.*, **1974**, 1492-1496.
11. Yokoyama, T.; Yokoyama, S.; Kamikado, T.; Okuno, Y.; Mashiko, S., *Nature*, **2001**, 413, 619-621.
12. Ellis, P. E.; Lyon, J. E. Cyano- and polycyanometalloporphyrins as catalysts for alkane oxidation. B01J 31/18, C07D 487/22, **1993**.
13. Balaban, M. C.; Eichhöfer, A.; Buth, G.; Hauschild, R.; Szmytkowski, J.; Kalt, H.; Balaban, T. S., *J. Phys. Chem. B*, **2008**, 112, 5512-5521.

14. Rappoport, Z., *The Chemistry of the Cyano Group*. Interscience Publishers: London, **1970**.
15. Larock, R. C., *Comprehensive Organic Transformations*. 2nd ed.; Wiley-VCH: New York, **1999**.
16. Yeh, C.-Y.; Miller, S. E.; Carpenter, S. D.; Nocera, D. G., *Inorg. Chem.*, **2001**, *40*, 3643-3646.
17. Wang, R.; Falck, J. R., *Cat. Rev. - Sci. Eng.*, **2014**, *56*, 288-331.
18. Smith, K. M.; Barnett, G. H.; Evans, B.; Martynenko, Z., *J. Am. Chem. Soc.*, **1979**, *101*, 5953-5961.
19. Callot, H. J.; Louati, A.; Gross, M., *Tetrahedron Lett.*, **1980**, *21*, 3281-3284.
20. Wu, G.-Z.; Leung, H.-K.; Gan, W.-X., *Tetrahedron*, **1990**, *46*, 3233-3244.
21. Smith, K. M.; Goff, D. A.; Simpson, D. J., *J. Am. Chem. Soc.*, **1985**, *107*, 4946-4954.
22. Sharman, W. M.; Lier, J. E. V., *J. Porphyrins Phthalocyanines*, **2000**, *04*, 441-453.
23. DiMugno, S. G.; Lin, V. S.-Y.; Therien, M. J., *J. Am. Chem. Soc.*, **1993**, *115*, 2513-2515.
24. DiMugno, S. G.; Lin, V. S.-Y.; Therien, M. J., *J. Org. Chem.*, **1993**, *58*, 5983-5993.
25. Chan, K. S.; Zhou, X.; Au, M. T.; Tam, C. Y., *Tetrahedron*, **1995**, *51*, 3129-3136.
26. Boyle, R. W.; Johnson, C. K.; Dolphin, D. *J. Chem. Soc., Chem. Commun.*, **1995**, 527-528.
27. Hyslop, A. G.; Kellett, M. A.; Iovine, P. M.; Therien, M. J., *J. Am. Chem. Soc.*, **1998**, *120*, 12676-12677.
28. Shanmugathan, S.; Johnson, C. K.; Edwards, C.; Matthews, E. K.; Dolphin, D.; Boyle, R. W., *J. Porphyrins Phthalocyanines*, **2000**, *4*, 228-232.
29. Deng, Y.; Chang, C. K.; Nocera, D. G., *Angew Chem., Int. Ed.*, **2000**, *39*, 1066-1068.

30. Vaz, B.; Alvarez, R.; Nieto, M.; Paniello, A. I.; de Lera, A. R., *Tetrahedron Lett.*, **2001**, *42*, 7409-7412.
31. Chng, L. L.; Chang, C. J.; Nocera, D. G., *J. Org. Chem.*, **2003**, *68*, 4075-4078.
32. Chen, Y.-J.; Lee, G.-H.; Peng, S.-M.; Yeh, C.-Y., *Tetrahedron Lett.*, **2005**, *46*, 1541-1544.
33. Kurotobi, K.; Osuka, A., *Org. Lett.*, **2005**, *7*, 1055-1058.
34. Hata, H.; Shinokubo, H.; Osuka, A., *J. Am. Chem. Soc.*, **2005**, *127*, 8264-8265.
35. Takanami, T.; Hayashi, M.; Hino, F.; Suda, K., *Tetrahedron Lett.*, **2003**, *44*, 7353-7357.
36. Chen, Y.; Zhang, X. P., *J. Org. Chem.*, **2003**, *68*, 4432-4438.
37. Gao, G.-Y.; Colvin, A. J.; Chen, Y.; Zhang, X. P., *Org. Lett.*, **2003**, *5*, 3261-3264.
38. Gao, G.-Y.; Chen, Y.; Zhang, X. P., *Org. Lett.*, **2004**, *6*, 1837-1840.
39. Gao, G.-Y.; Colvin, A. J.; Chen, Y.; Zhang, X. P., *J. Org. Chem.*, **2004**, *69*, 8886-8892.
40. Takanami, T.; Hayashi, M.; Chijimatsu, H.; Inoue, W.; Suda, K., *Org. Lett.*, **2005**, *7*, 3937-3940.
41. Yamaoka, H., *JETI*, **2011**, *59*, 37-42.
42. Camaioni, N.; Garlaschelli, L.; Geri, A.; Maggini, M.; Possamai, G.; Ridolfi, G., *J. Mater. Chem.*, **2002**, *12*, 2065-2070.
43. Irimia-Vladu, M.; Marjanovic, N.; Vlad, A.; Ramil, A. M.; Hernandez-Sosa, G.; Schwödiauer, R.; Bauer, S.; Sariciftci, N. S., *Adv. Mater. (Weinheim, Ger.)*, **2008**, *20*, 3887-3892.
44. Riccò, M.; Bisbiglia, M.; De Renzi, R.; Bolzoni, F., *Solid State Commun.*, **1997**, *101*, 413-416.
45. Bosi, S.; Da Ros, T.; Spalluto, G.; Prato, M., *Eur. J. Med. Chem.*, **2003**, *38*, 913-923.

46. Haddon, R. C.; Brus, L. E.; Raghavachari, K., *Chem. Phys. Lett.*, **1986**, *125*, 459-464.
47. Xie, Q.; Perez-Cordero, E.; Echegoyen, L., *J. Am. Chem. Soc.*, **1992**, *114*, 3978-3980.
48. Boyd, P. D. W.; Reed, C. A., *Acc. Chem. Res.* **2005**, *38*, 235-242
49. Liddell, P. A.; Sumida, J. P.; Macpherson, A. N.; Noss, L.; Seely, G. R.; Clark, K. N.; Moore, A. L.; Moore, T. A.; Gust, D., *Photochem. Photobiol.*, **1994**, *60*, 537-541.
50. Basiuk, V. A., *J. Phys. Chem. A*, **2005**, *109*, 3704-3710.
51. V. Konarev, D.; N. Lyubovskaya, R., *Russ.Chem. Rev.*, **1999**, *68*, 19-38.
52. Moriyama, H.; Kobayashi, H.; Kobayashi, A.; Watanabe, T., *Chem. Phys. Lett.*, **1995**, *238*, 116-121.
53. Stephens, P. W.; Cox, D.; Lauher, J. W.; Mihaly, L.; Wiley, J. B.; Allemand, P.-M.; Hirsch, A.; Holczer, K.; Li, Q.; Thompson, J. D.; Wudl, F., *Nature (London)*, **1992**, *355*, 331-332.
54. Kveder, V. V.; Steinman, E. A.; Narymbetov, B. Z.; Khasanov, S. S.; Rozenberg, L. P.; Shibaeva, R. P.; Bazhenov, A. V.; Gorbunov, A. V.; Maksimuk, M. Y.; Konarev, D. V.; Lyubovskaya, R. N.; Ossipyan, Y. A., *Chem.Phys.*, **1997**, *216*, 407-415.
55. Kajzar, F.; Okada-Shudo, Y.; Meritt, C.; Kafafi, Z., *Synth. Met.*, **1998**, *94*, 91-98.
56. Luo, C.; Guldi, D. M.; Imahori, H.; Tamaki, K.; Sakata, Y., *J. Am. Chem. Soc.*, **2000**, *122*, 6535-6551.
57. Imahori, H.; Tamaki, K.; Guldi, D. M.; Luo, C.; Fujitsuka, M.; Ito, O.; Sakata, Y.; Fukuzumi, S., *J. Am. Chem. Soc.*, **2001**, *123*, 2607-2617.
58. Yamada, H.; Imahori, H.; Nishimura, Y.; Yamazaki, I.; Ahn, T. K.; Kim, S. K.; Kim, D.; Fukuzumi, S., *J. Am. Chem. Soc.*, **2003**, *125*, 9129-9139.
59. Armaroli, N.; Diederich, F.; Echegoyen, L.; Habicher, T.; Flamigni, L.; Marconi, G.; Nierengarten, J.-F., *New J. Chem.*, **1999**, *23*, 77-83.

-
60. Williams, R. M.; Zwier, J. M.; Verhoeven, J. W., *J. Am. Chem. Soc.*, **1995**, *117*, 4093-4099.
61. Jonathan, L. S.; Steven, J. W., in: Expanded, Contracted, & Isomeric Porphyrins, Pergamon, Oxford: **1997**; vol. 15, pp 11-125.
62. Palmer, J., *Transition Metal Corrole Coordination Chemistry*. Struct. Bonding: **2012**; vol. 142, p 49-89.
63. Vogel, E.; Will, S.; Tilling, A. S.; Neumann, L.; Lex, J.; Bill, E.; Trautwein, A. X.; Wieghardt, K., *Angew. Chem. Int. Ed.*, **1994**, *33*, 731-735.
64. Aviv-Harel, I.; Gross, Z., *Chem. Eur. J.*, **2009**, *15*, 8382-8394.
65. Buckley, H. L.; Arnold, J., *Dalton Trans.*, **2015**, *44*, 30-36.
66. Li, C.-Y.; Zhang, X.-B.; Han, Z.-X.; Akermark, B.; Sun, L.; Shen, G.-L.; Yu, R.-Q., *Analyst*, **2006**, *131*, 388-393.
67. Gross, Z.; Galili, N.; Saltsman, I., *Angew. Chem., Int. Ed.*, **1999**, *38*, 1427-1429.
68. Radecki, J.; Stenka, I.; Dolusic, E.; Dehaen, W.; Plavec, J., *Comb. Chem. High Throughput Screening*, **2004**, *7*, 375-381.
69. Johnson, A. W.; Kay, I. T., *J. Chem. Soc.*, **1965**, 1620-1629.
70. Johnson, A. W.; Kay, I. T., *Proc. Chem. Soc.*, **1965**, 288, 334-341.
71. Harrison, H. R.; Hodder, O. J. R.; Hodgkin, D. C., *J. Chem. Soc. B*, **1971**, 640-645.
72. R. Paolesse in *The Porphyrin Handbook*, V.; (Eds.: K. M. Kadish, K. M. S., R. Guilard), Academic Press,; New York, Chapter 11, pp. 201-232, **2000**,
73. Paolesse, R.; Licoccia, S.; Fanciullo, M.; Morgante, E.; Boschi, T., *Inorg. Chim. Acta*, **1993**, *203*, 107-114.
74. Paolesse, R.; Tassoni, E.; Licoccia, S.; Paci, M.; Boschi, T., *Inorg. Chim. Acta*, **1996**, *241*, 55-60.
75. Steene, E.; Wondimagegn, T.; Ghosh, A., *J. Phys. Chem. B.*, **2001**, *105*, 11406-11413.

-
76. Paolesse, R.; Mini, S.; Sagone, F.; Boschi, T.; Jaquinod, L.; J. Nurco, D.; M. Smith, K., *Chem. Commun.*, **1999**, 1307-1308.
77. Ka, J.-W.; Cho, W.-S.; Lee, C.-H., *Tetrahedron Lett.*, **2000**, *41*, 8121-8125.
78. Collman, J. P.; Decreau, R. A., *Tetrahedron Lett.*, **2003**, *44*,
79. Gryko, D. T., *Chem. Commun.*, **2000**, 2243-2244.
80. Briñas, R. P.; Brückner, C., *Synlett*, **2001**, *2001*, 0442-0444.
81. Asokan, C. V.; Smeets, S.; Dehaen, W., *Tetrahedron Lett.*, **2001**, *42*, 4483-4485.
82. Král, V.; Vašek, P.; Dolensky, B., *Collect. Czech. Chem. Commun.*, **2004**, *69*, 1126-1136.
83. Koszarna, B.; Gryko, D. T., *J. Org. Chem.*, **2006**, *71*, 3707-3717.
84. Kumari, P.; Chauhan, S. M. S., *J. Heterocycl. Chem.*, **2008**, *45*, 779-783.
85. Zhan, H.-Y.; Liu, H.-Y.; Chen, H.-J.; Jiang, H.-F., *Tetrahedron Lett.*, **2009**, *50*, 2196-2199.
86. Dogutan, D. K.; Stoian, S. A.; McGuire, R.; Schwalbe, M.; Teets, T. S.; Nocera, D. G., *J. Am. Chem. Soc.*, **2011**, *133*, 131-140.
87. Ding, T.; Alemán, E. A.; Modarelli, D. A.; Ziegler, C. J., *J. Phys. Chem. A*, **2005**, *109*, 7411-7417.
88. Ding, T.; Harvey, J. D.; Ziegler, C. J., *J. Porphyrins Phthalocyanines*, **2005**, *09*, 22-27.
89. Balazs, Y. S.; Saltsman, I.; Mahammed, A.; Tkachenko, E.; Golubkov, G.; Levine, J.; Gross, Z., *Magn. Reson. Chem.*, **2004**, *42*, 624-635.
90. Liu, X.; Mahammed, A.; Tripathy, U.; Gross, Z.; Steer, R. P., *Chem. Phys. Lett.*, **2008**, *459*, 113-118.
91. Franken, P. A.; Hill, A. E.; Peters, C. W.; Weinreich, G., *Phys. Rev. Lett.*, **1961**, *7*, 118-119.

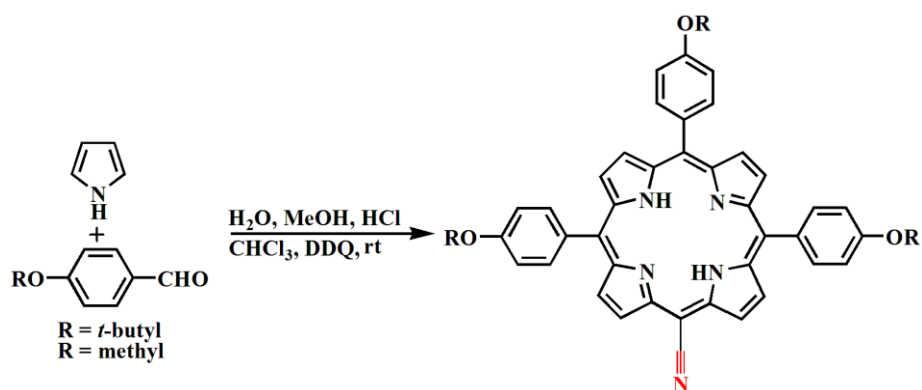
92. Perry, J. W.; Mansour, K.; Lee, I.-Y. S.; Wu, X.-L.; Bedworth, P. V.; Chen, C.-T.; Ng, D.; Marder, S. R.; Miles, P.; Wada, T.; Tian, M.; Sasabe, H., *Science*, **1996**, *273*, 1533-1536.
93. Hann, R. A.; Bloor, D., *Organic Materials for Nonlinear Optics*. The Royal Society of Chemistry: London, **1989**.
94. Calvete, M.; Yang, G. Y.; Hanack, M., *Syn. Met.*, **2004**, *141*, 231-243.
95. Dini, D.; Barthel, M.; Hanack, M., *Eur. J. Org. Chem.*, **2001**, *2001*, 3759-3769.
96. Hanack, M.; Schneider, T.; Barthel, M.; Shirk, J. S.; Flom, S. R.; Pong, R. G. S., *Coord. Chem. Rev.*, **2001**, *219–221*, 235-258.
97. Dini, D.; Calvete, M.; Vagin, S.; Hanack, M.; Eriksson, A.; Lopes, C., *J. Porphyrins Phthalocyanines*, **2006**, *10*, 1165-1171.
98. Rebane, A.; Drobizhev, M.; Makarov, N. S.; Koszarna, B.; Tasiar, M.; Gryko, D. T., *Chem. Phys. Lett.*, **2008**, *462*, 246-250.
99. Anusha, P. T.; Swain, D.; Hamad, S.; Giribabu, L.; Prashant, T. S.; Tewari, S. P.; Rao, S. V., *J. Phys. Chem. C*, **2012**, *116*, 17828-17837.

CHAPTER 2

A New Synthetic Protocol For the Preparation of 5-Cyano- 10, 15, 20 tris(alkoxyphenyl)porphyrins

- 2.1 Abstract
- 2.2 Introduction
- 2.3 Results and Discussions
 - 2.3.1 Synthesis, Spectral Analysis, and Photophysical Studies
 - 2.3.2 X-ray Analysis
 - 2.3.3 Mechanism
- 2.4 Conclusions
- 2.5 Experimental Section
 - 2.5.1 Materials and Methods
 - 2.5.2 Physical Measurements
 - 2.5.3 Crystal Structure Determination
 - 2.5.4 Synthesis of **Porphyrin 1**
 - 2.5.5 Synthesis of **Porphyrin 2**

2.1 Abstract

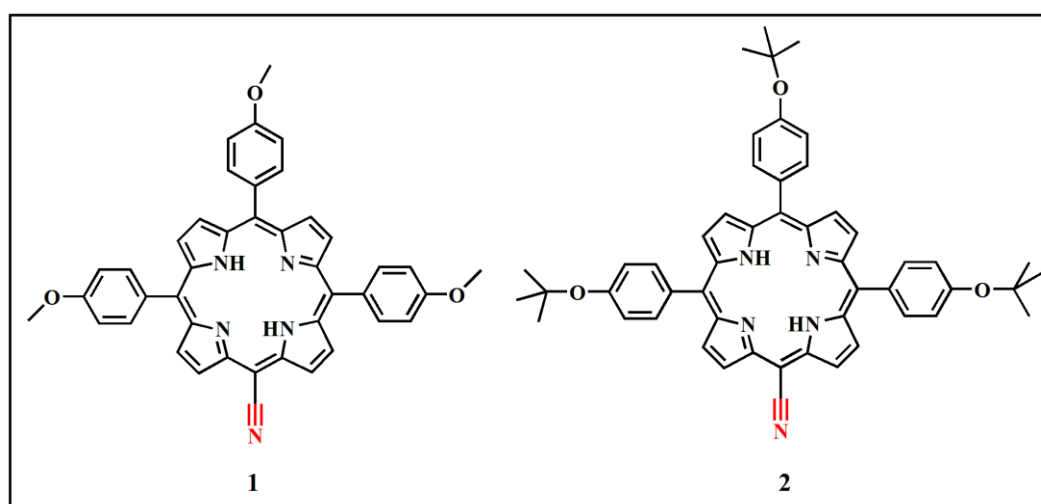


All the existing literatures reveal that meso-cyanoporphyrins are synthesized from porphyrin based starting materials. We report herein a new synthetic protocol for the preparation of meso-cyanoporphyrins which does not need any porphyrin based starting material. Meso-cyanoporphyrins can be directly synthesized from pyrrole and aldehyde. A representative crystal structure along with detailed spectroscopic studies are presented and discussed. An attempt has been made to explain the probable mechanism, based on GC-mass analysis of the reaction intermediates.

2.2 Introduction

Porphyrins and metalloporphyrins are very important molecules from the perspective of their widespread applications in many areas of chemistry, biology and materials science.¹ A large number of research groups are actively involved in the synthesis of various substituted porphyrins.¹ Cyano substituted porphyrins are in the forefront among the porphyrin systems because of their extensive applications as precursors for the synthesis of many complex porphyrin related molecules.^{2,3} Hence there is a great demand for the development of synthetic methodologies for the facile synthesis of cyano substituted porphyrins. Several methodologies have been reported in the literature for the synthesis of *meso*-cyanoporphyrins.⁴ Callot *et al.* reported the synthesis of cyano substituted porphyrin by using cuprous cyanide at high temperature.⁵⁻⁷ Inhoffen and co-workers have used a series of organic transformations including Schiff's base formation, Vilsmeier formylation, generation of oxime, and finally dehydration with acetic anhydride for the same.^{8,9} Synthesis of metalloporphyrin π -cation radicals by anodic oxidation followed by coupling with the CN^- ion was another method adopted by Smith *et al.*¹⁰⁻¹² Besides, Friedel-Crafts cyanation,¹³ Pd or Cu catalyzed cross coupling reactions: Suzuki-coupling reactions, Sonogashira-coupling reactions and Stille-coupling reactions have also been employed for the synthesis of *meso*-cyanoporphyrins.¹⁴⁻³¹ Thus the synthesis of *meso*-cyanoporphyrins involved the cyanation of either the porphyrin macrocycle or the metalloporphyrin derivative. In most cases the choice of porphyrin or metalloporphyrin based starting materials are also limited and costly. We report herein a new synthetic protocol for the synthesis of cyanoporphyrin. Our methodology does not need any porphyrin or metalloporphyrin based starting material. It is based on four key findings: (i) no porphyrin/metalloporphyrin based starting materials, (ii) the least number of synthetic steps, (iii) no addition of any traditional cyanation reagents, and (iv) a hitherto less investigated solvent mixture in porphyrin synthesis. DDQ (2,3-dichloro-5,6-dicyano

benzoquinone) is an oxidizing agent frequently used in organic synthesis. DDQ has been used to perform a dual role here: (i) as an oxidizing agent necessary for the conversion of porphyrinogen to porphyrin derivative and (ii) participating in the cyanation reaction for cyanoporphyrin formation. These important modifications reduce the number of synthetic steps drastically. The H₂O/HCl/MeOH system has also been rarely used in the synthesis of porphyrins.^{32,33} This mixture is frequently used in the synthesis of corrole. Thus we have developed a new synthetic methodology based on a simple combination of the H₂O/HCl/MeOH system and DDQ. A simple benzaldehyde that contains *tert*-butoxy or methoxy group at the *para* position of phenyl ring underwent this kind of cyanation reaction to yield the corresponding cyano substituted porphyrins (Scheme 2.1).

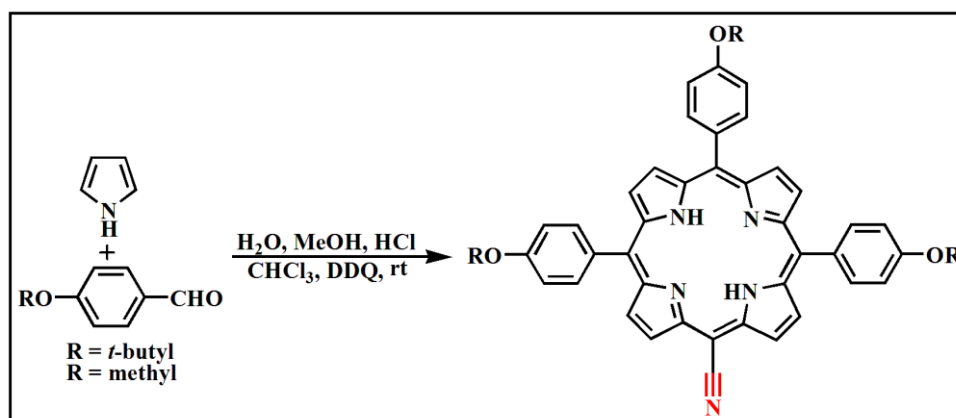


Scheme 2.1. Structure of cyanoporphyrins.

2.3 Results and Discussions

2.3.1 Synthesis, Spectral Analysis, and Photophysical Studies

The *meso*-cyanoporphyrins were prepared by the reaction of pyrrole with 4-alkoxy benzaldehyde in a (1:1) methanol water mixture at 25°C in the presence of hydrochloric acid, followed by addition of DDQ (Scheme 2.2). The yields of porphyrin **1** and porphyrin **2** were



Scheme 2.2. Synthesis of cyanoporphyrins.

3.5% and 2.1%, respectively. We recognize that the yields are very low, however we have to keep in mind that previously only after a multistep synthesis (at least three or four steps) can one achieve the synthesis of cyanoporphyrins. In that context, our methodology will be beneficial and advantageous on the basis of the overall yield. Satisfactory elemental analyses and electrospray mass spectra demonstrated the purity and identity of the *meso*-cyanoporphyrins. The ESI signals were observed at m/z values of 654.62 and 780.40 for porphyrins **1** and **2**, respectively (Figure 2.1 and 2.2), which corresponded to $\{\mathbf{1}\}^+$ (calculated mass: 653.72) and $\{\mathbf{2}\}^+$ (calculated mass: 779.38). The $\text{C}\equiv\text{N}$ stretching bands were observed in the IR spectra at 2211 cm^{-1} for porphyrin **1** and at 2218 cm^{-1} for porphyrin **2** (Figure 2.3 and 2.4). The ^1H NMR spectrum of porphyrin **1** in CDCl_3 is shown in Figure 2.5 and the ^1H NMR spectrum of porphyrin **2** in CDCl_3 is shown in Figure 2.6. All the signals and peak integrals arising from the *meso*-aryl groups, pyrrole groups and inner NH protons were clearly resolved and are consistent with the corresponding porphyrins **1**. Porphyrin **1** showed β -pyrrole resonance at 9.55 (2 H), 9.02 (2 H), and 8.78–8.88 (4 H) ppm relative to H_2TPP (8.85 ppm) in CDCl_3 . The *ortho*- and *meta*-phenyl protons of the *meso*-aryl group showed

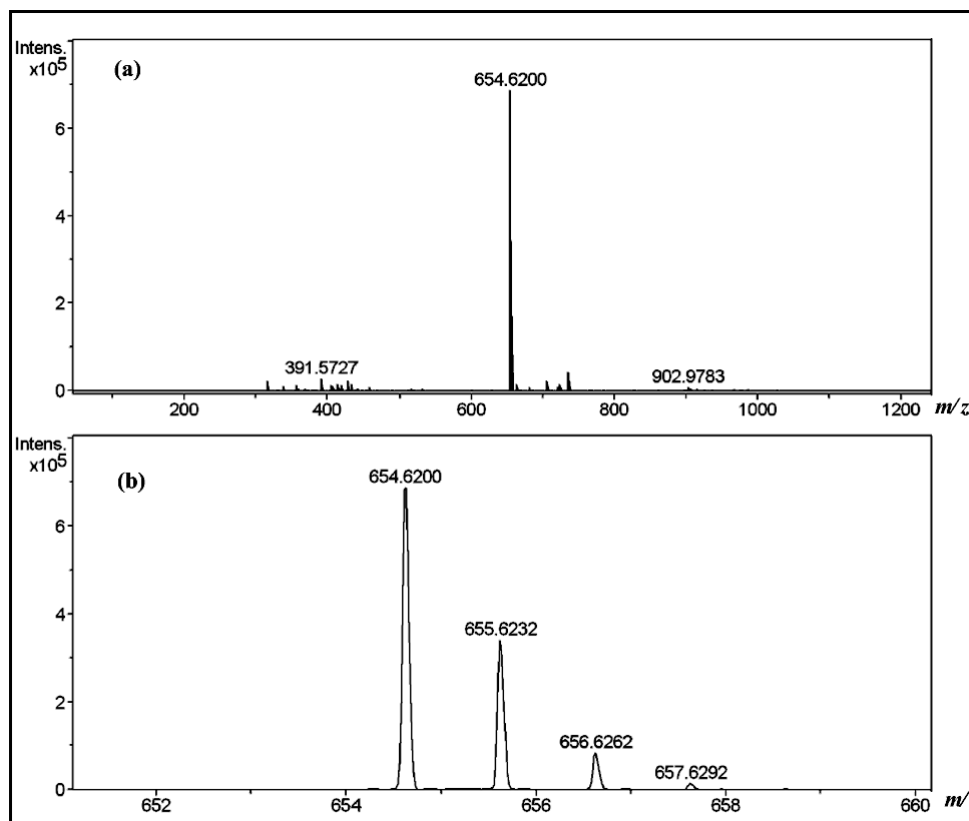


Figure 2.1. ESI-MS spectrum of porphyrin **1** in CH₃CN (a) shows the measured spectrum and (b) shows an expansion of the isotopic distribution pattern.

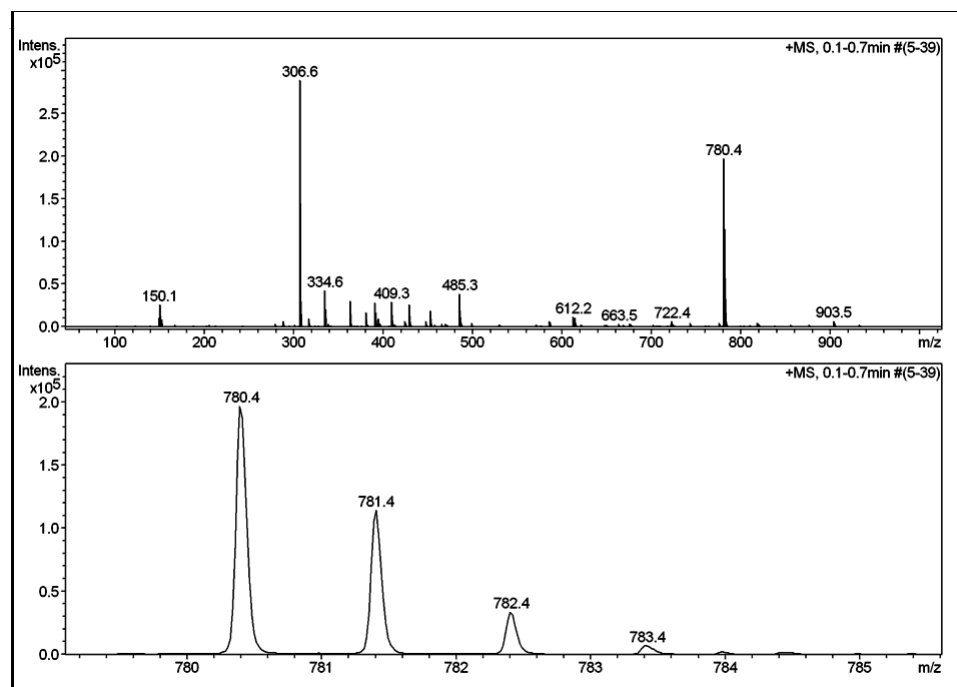


Figure 2.2. ESI-MS spectrum of porphyrin **2** in CH₃CN (a) shows the measured spectrum and (b) shows an expansion of the isotopic distribution pattern.

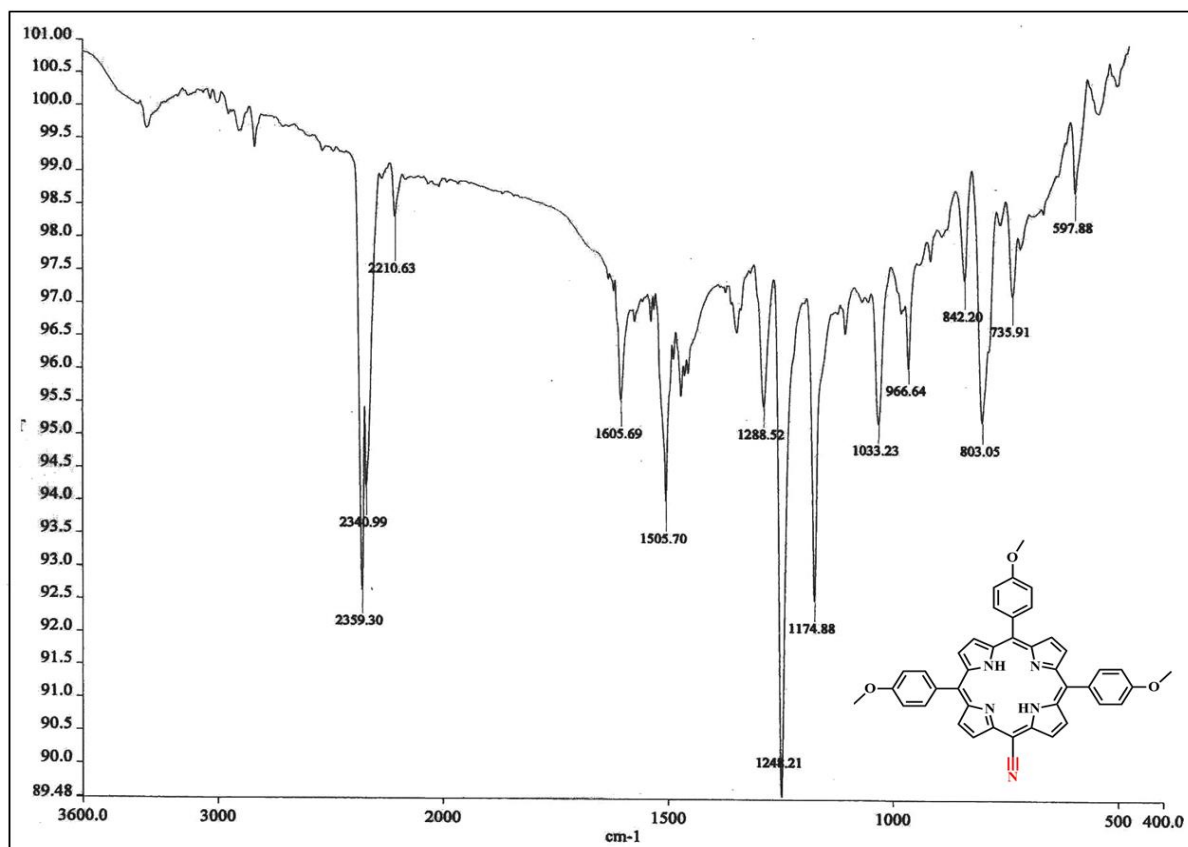


Figure 2.3. FTIR spectrum of porphyrin 1, as a KBr pellet.

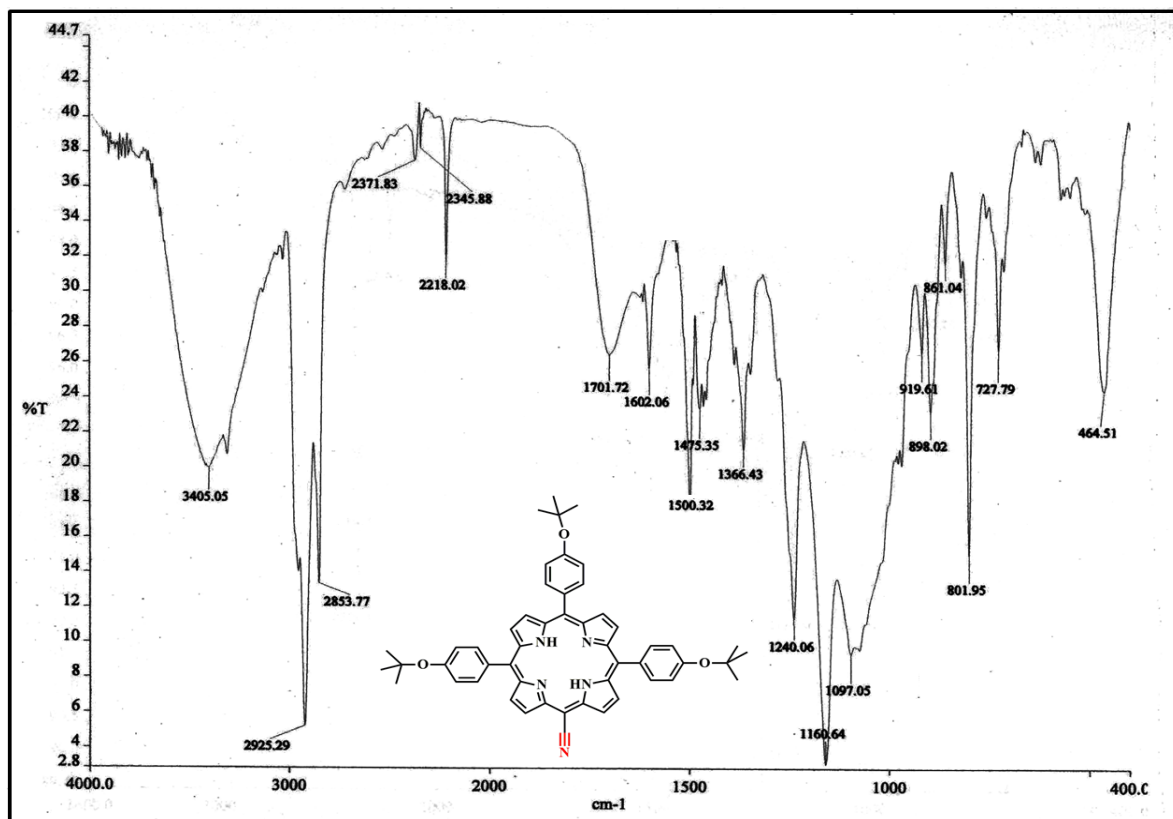


Figure 2.4. FTIR spectrum of porphyrin 2, as a KBr pellet.

resonance at 8.07–8.14 (6 H) and 7.27–7.34 (6 H) ppm respectively, relative to those in H₂TPP (8.28 and 7.75 ppm). The inner NH protons had resonance at –2.34 (2 H) ppm relative to H₂TPP (–2.79 ppm). The methoxy protons appeared at 4.09–4.12 (9 H) ppm.

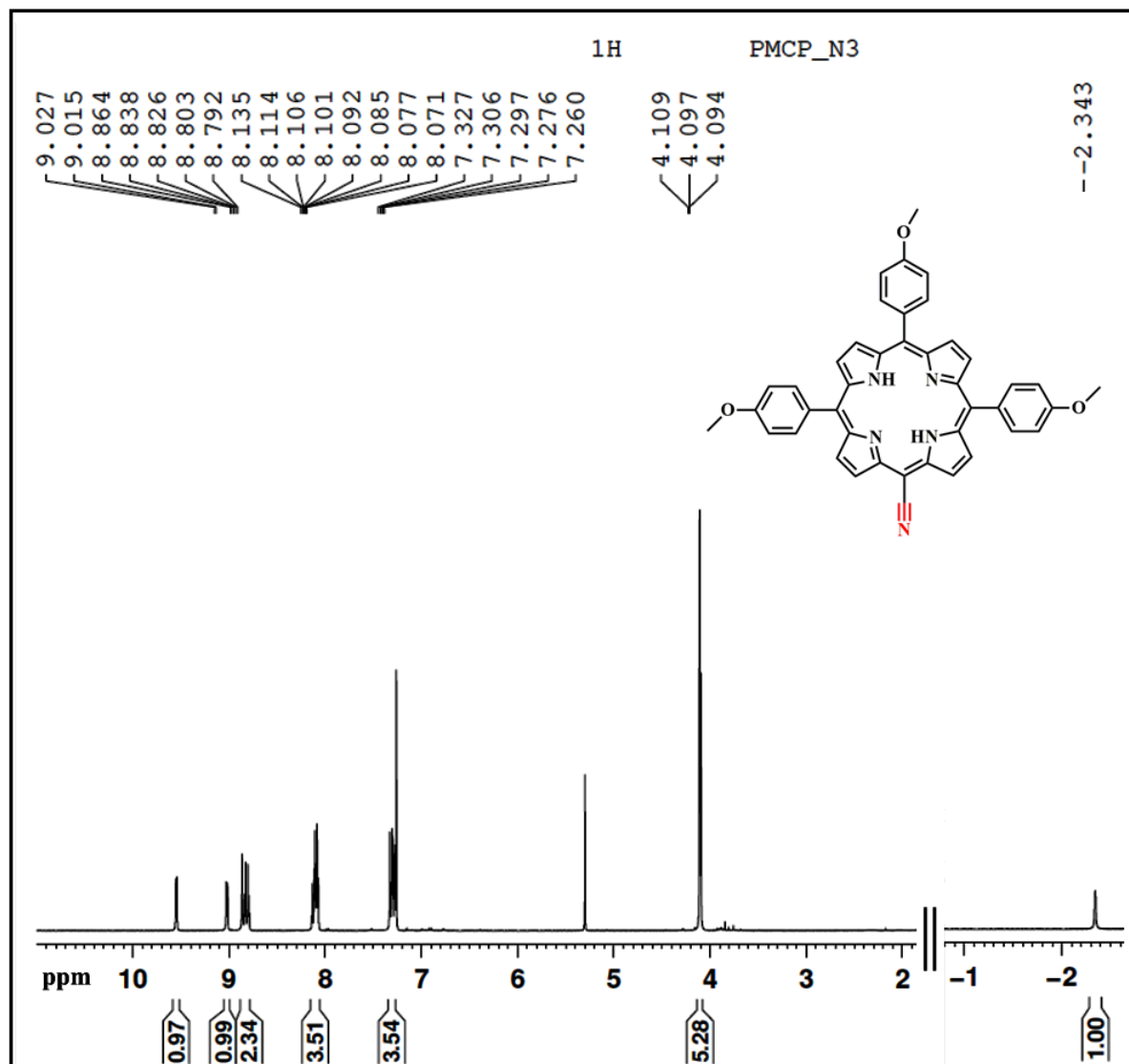


Figure 2.5. ¹H NMR spectrum of porphyrin **1** in CDCl₃.

Similarly, porphyrin **2** showed β -pyrrole resonance at 9.57 (2 H), 9.03 (2 H), and 8.70–8.84 (4 H) ppm relative to H₂TPP (8.85 ppm) in CDCl₃. The *ortho*- and *meta*-phenyl protons of the *meso*-aryl group were in resonance at 8.0–8.1 (6 H), and 7.35–7.43 (6 H) ppm respectively relative to those in H₂TPP (8.28 and 7.75 ppm). The inner NH protons had resonance at –2.36 (2 H) ppm relative to H₂TPP (–2.79 ppm). The tertiary butyloxy protons

appeared at 1.57–1.64 (27 H) ppm. The values matched well with the analogous H₂TPP derivative. These spectra showed the presence of both EDG and EWG groups in the porphyrin macrocycles. In toluene, porphyrin **1** and porphyrin **2** exhibited five major transitions (Figure 2.7.a and Figure 2.7.b). The Soret and Q-bands were observed at 425, 521, 559, 596, and 651 nm for porphyrin **1** and at 425, 522, 559, 594, and 649 nm for porphyrin **2**.

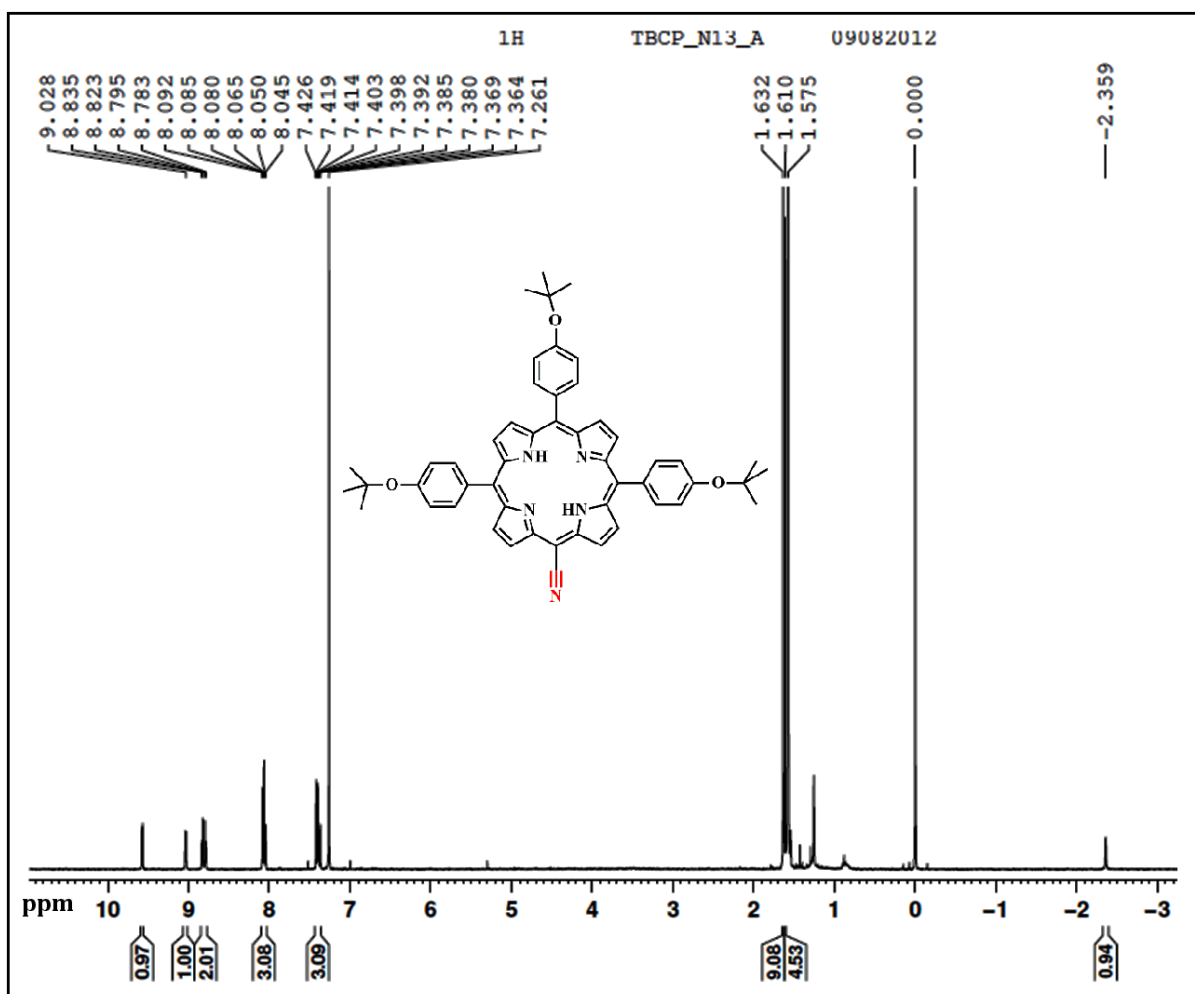


Figure 2.6. ¹H NMR spectrum of porphyrin **2** in CDCl₃.

Porphyrin **1** displayed strong fluorescence at 658 and 722 nm (Figure 2.7.a) with a quantum yield $\phi = 0.11$ at room temp in toluene solvent. The fluorescence lifetime of porphyrin **1** was estimated to be 7.56 ns. The porphyrin **2** displayed strong fluorescence at 656 nm and 719 nm (Figure 2.7.b) with a quantum yield $\phi = 0.10$ at room temp in toluene solvent. The fluorescence lifetime of porphyrin **2** was estimated to be 9.08 ns.

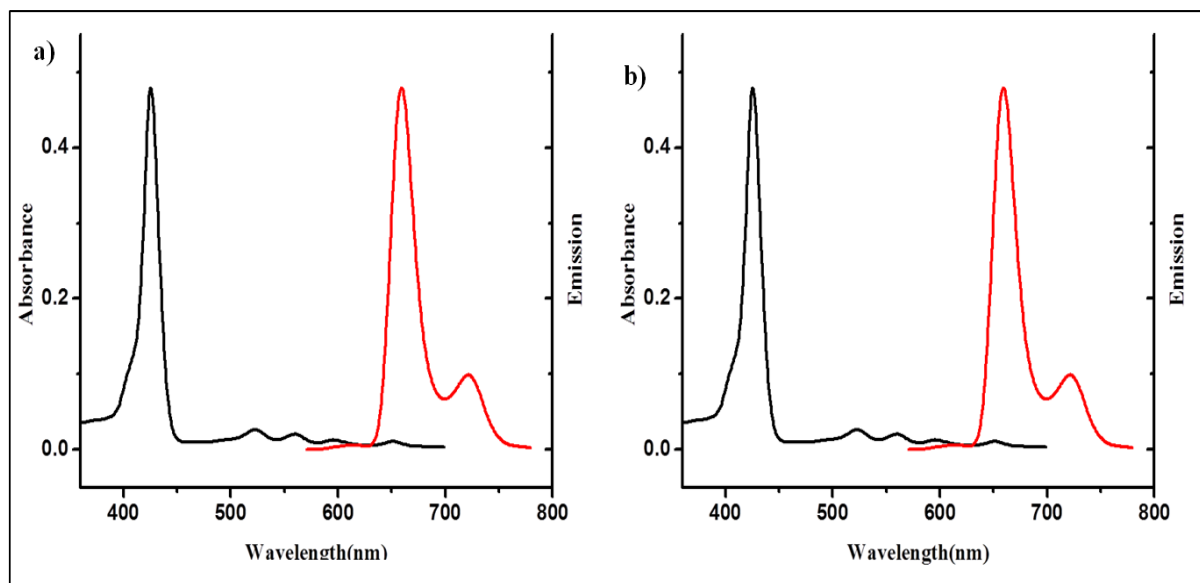


Figure 2.7. (a) Electronic absorption (—) and normalized emission (—) spectrum of porphyrin **1** in toluene. (b) Electronic absorption (—) and normalized emission (—) spectrum of porphyrin **2** in toluene.

2.3.2. X-Ray Analysis

The crystal structure of the representative *meso*-cyanoporphyrin **2** is shown in Figure 2.8. The crystal system was found to be triclinic with the unit cell having two porphyrin molecules. Important crystallographic parameters are presented in Table 2.1. The bond distances and angles agreed well with the standard reported data.³⁴⁻³⁶ The porphyrin ring was slightly ruffled due to the presence of the bulky *tert*-butoxy groups at the *para* position of the phenyl rings in the *meso* carbon of the porphyrin. The *meso*-aryl groups were deviated from the mean porphyrin plane by angles of 72.245°, 54.282° and 56.279°, which clearly indicated that the *tert*-butoxy groups played a major role in the distortion of the *meso*-aryl groups, and these values compared well with those for H₂TPP, an analogous porphyrin derivative.³⁴⁻³⁶ The pyrrole units were also deviated from the mean porphyrin plane by angles of 8.65°, 7.56°, 3.44°, and 4.44°, indicating the near-planar nature of the pyrrole units. The cyano-group was deviated from the mean porphyrin plane by an angle of 3.13°, indicating that the *meso* substituted cyano group was almost planar with the porphyrin ring. The C≡N bond distance was 1.163 Å, which matched well with the average C≡N bond distance available in

the literature.^{15,37} Several C–H··· π interactions in Figure 2.9.c along with intermolecular C–H···N, C–H···C and C–H···O interactions (Figure 2.9.a, 2.9.b, and 2.9.d) were observed in the crystal structure. The *meso*-cyanoporphyrins were stacked together and formed channel-like arrangements throughout the crystal lattice. The closest distance between two neighbouring porphyrin macro-cycle responsible for π - π stacking interactions was ~ 4.01 Å. This clearly indicated that there was a reasonably strong adjacent parallel plane π - π stacking interaction between the porphyrin molecules (Figure 2.9.f). The cyanide groups were aligned

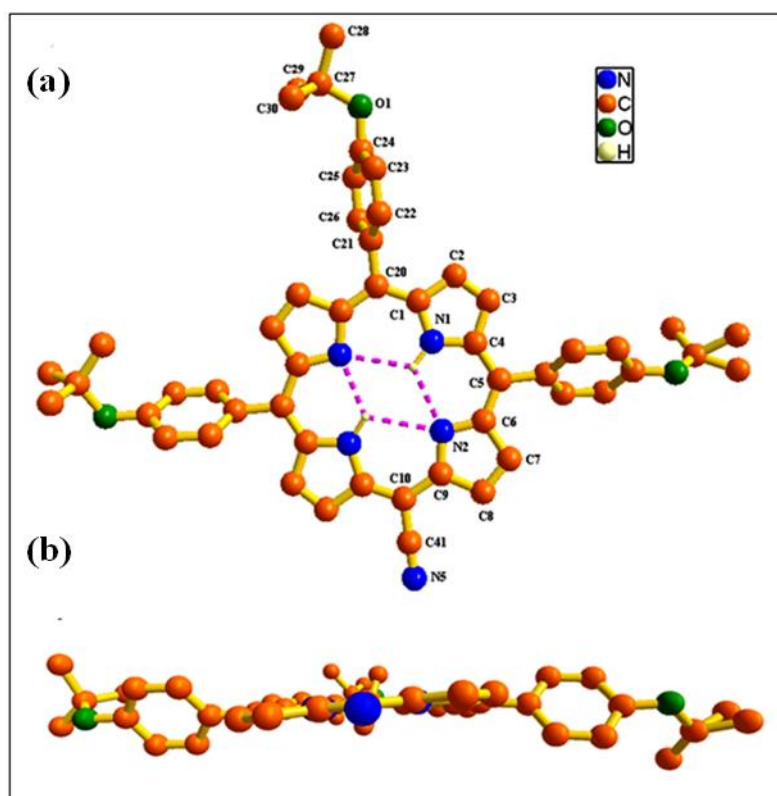


Figure 2.8. Single-crystal X-ray structure of porphyrin **2**, (a) top view with intramolecular hydrogen bonding interaction between the amine and imine units, (b) side view. Hydrogen atoms omitted for clarity.

in an opposite fashion to each other between the two adjacent porphyrins. The closest distance between two N-atoms of two cyanide group was ~ 9.5 Å (Figure 2.9.e). The shortest intermolecular distance between two porphyrin molecules responsible for C–H···O

interactions, C–H···C interactions, C–H···N interactions, and C–H··· π interactions were close to ~ 4.06 Å, ~ 3.09 Å, ~ 2.69 Å, and ~ 3.09 Å respectively. These clearly indicated that

Table 2.1. Crystallographic Data for porphyrin 2

Molecular formula	C ₅₁ H ₄₉ N ₅ O ₃
Fw	779.95
Radiation	MoK α
Crystal symmetry	Triclinic
Space group	P1
<i>a</i> (Å)	11.2663(3)
<i>b</i> (Å)	14.4132(4)
<i>c</i> (Å)	15.2221(4)
α (degree)	108.103(2)
β (degree)	95.829(2)
γ (degree)	92.046(2)
<i>V</i> (Å ³)	2331.39(11)
Z	2
μ (mm ⁻¹)	0.070
<i>T</i> (K)	293(2)K
<i>D</i> _{calcd} (g cm ⁻³)	1.111
2 θ range (deg)	2.84 to 51.08
<i>e</i> data (<i>R</i> _{int})	8674 (0.0639)
<i>R</i> ₁ (<i>I</i> > 2 σ (<i>I</i>))	0.0874
wR2	0.2428
GOF	0.963

fairly strong intermolecular C–H··· π interactions, C–H···O, C–H···N and C–H···C interactions were present between adjacent porphyrin molecules. It was assumed that the solid state structure was stable due to intermolecular parallel-displaced π - π stacking interactions, C–H··· π interactions, C–H···O, C–H···N and C–H···C interactions.³⁴⁻³⁶

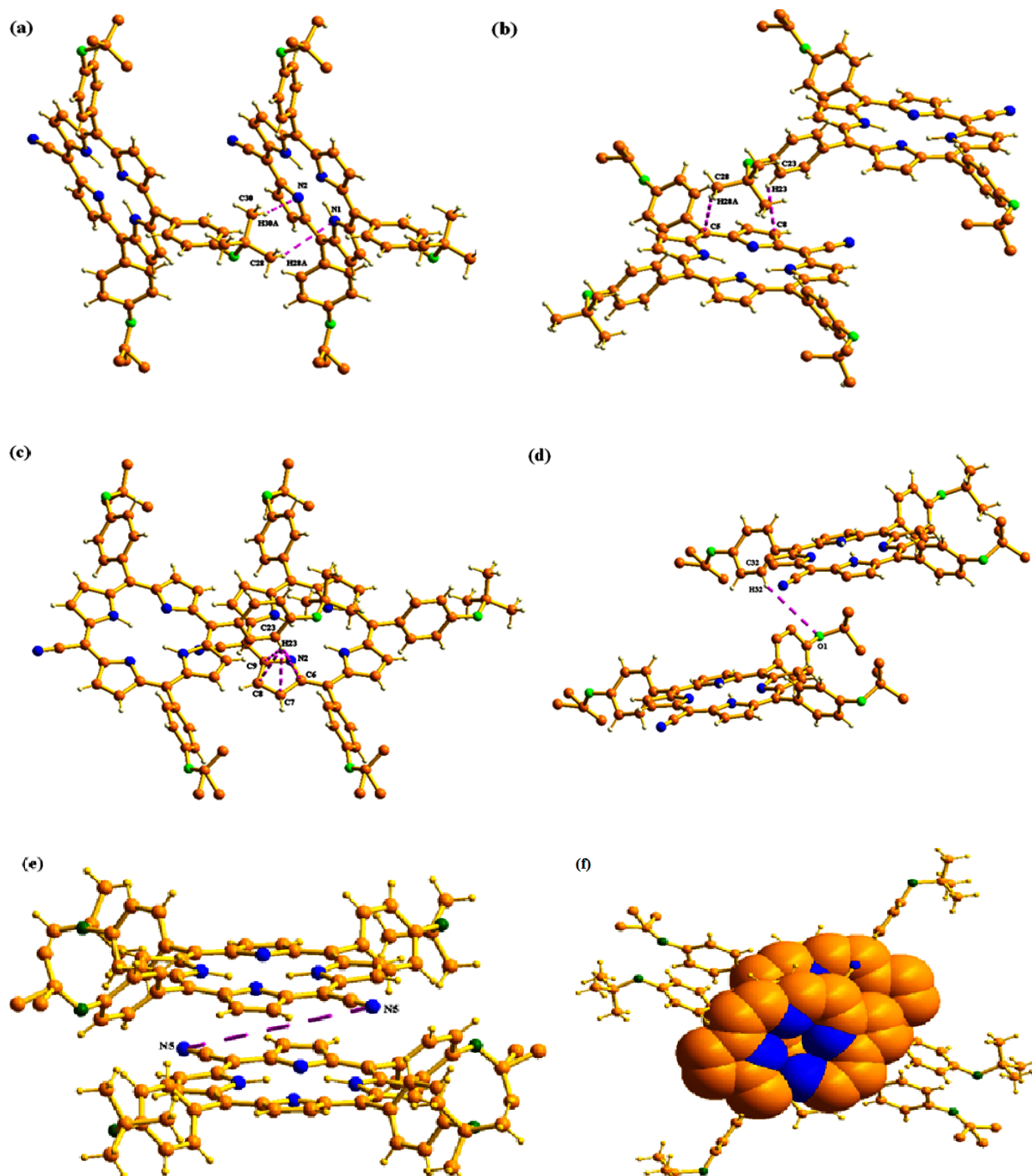


Figure 2.9. X-ray single crystal structure analysis of porphyrin **2**. (a) C-H \cdots N interactions, [2.69 Å, 163.43° and 3.12 Å, 137.47°] (b) C-H \cdots C interactions [3.09 Å, 134.66° and 3.53 Å, 168.61°] (c) C-H \cdots π stacking interactions [3.09 Å–3.22 Å] (d) C-H \cdots O interactions, [4.06 Å, 148°] (e) CN-CN distance, [9.5 Å] and (f) π - π stacking interactions [4.01 Å]. The entries in square brackets are the distances and the angles.

2.3.3. Mechanism

It was observed that the reagent grade methanol used by us contained traces of formaldehyde (0.002%). In a typical experiment 200 mL of methanol was used. Thus the amount of total

formaldehyde was 0.004 mL, i.e., equal to 0.108 mmol in the reaction mixture. Alternatively, addition of an aqueous solution of formaldehyde in a suitable molar ratio could also lead to the formation of the targeted *meso*-cyanoporphyrin. It was reported earlier that the combination of H₂O/HCl/MeOH system and DDQ favours the formation of corrole.^{32,33} However traces of the symmetric porphyrin were always obtained. We were unable to detect the traces of porphine, but we were able to detect the presence of tetrapyrane in GC-EIMS (Figure 2.10). Upon oxidation, tetrapyrane resulted in corrole. The presence of di(1*H*-pyrrol-

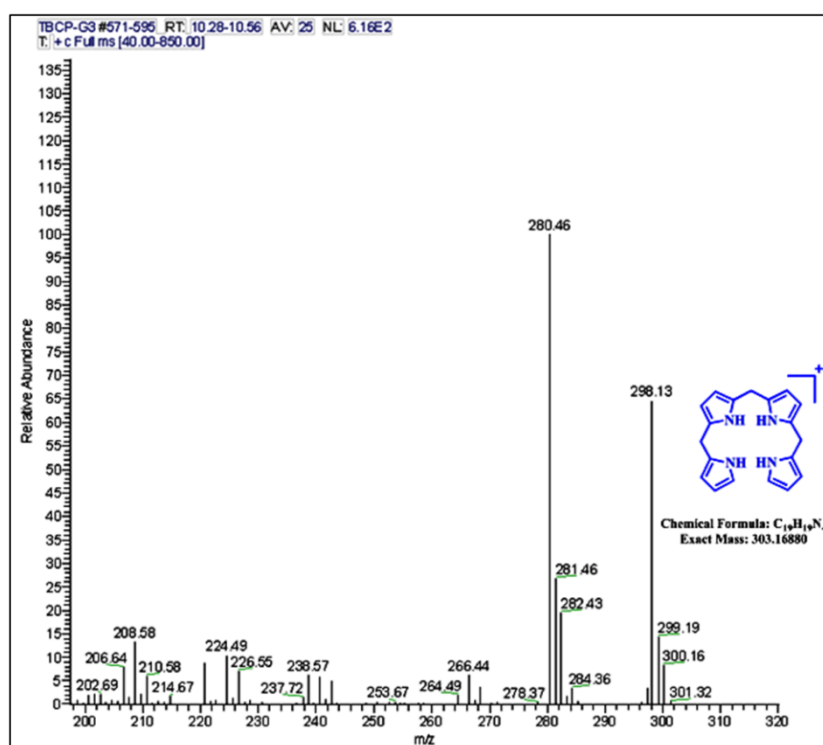
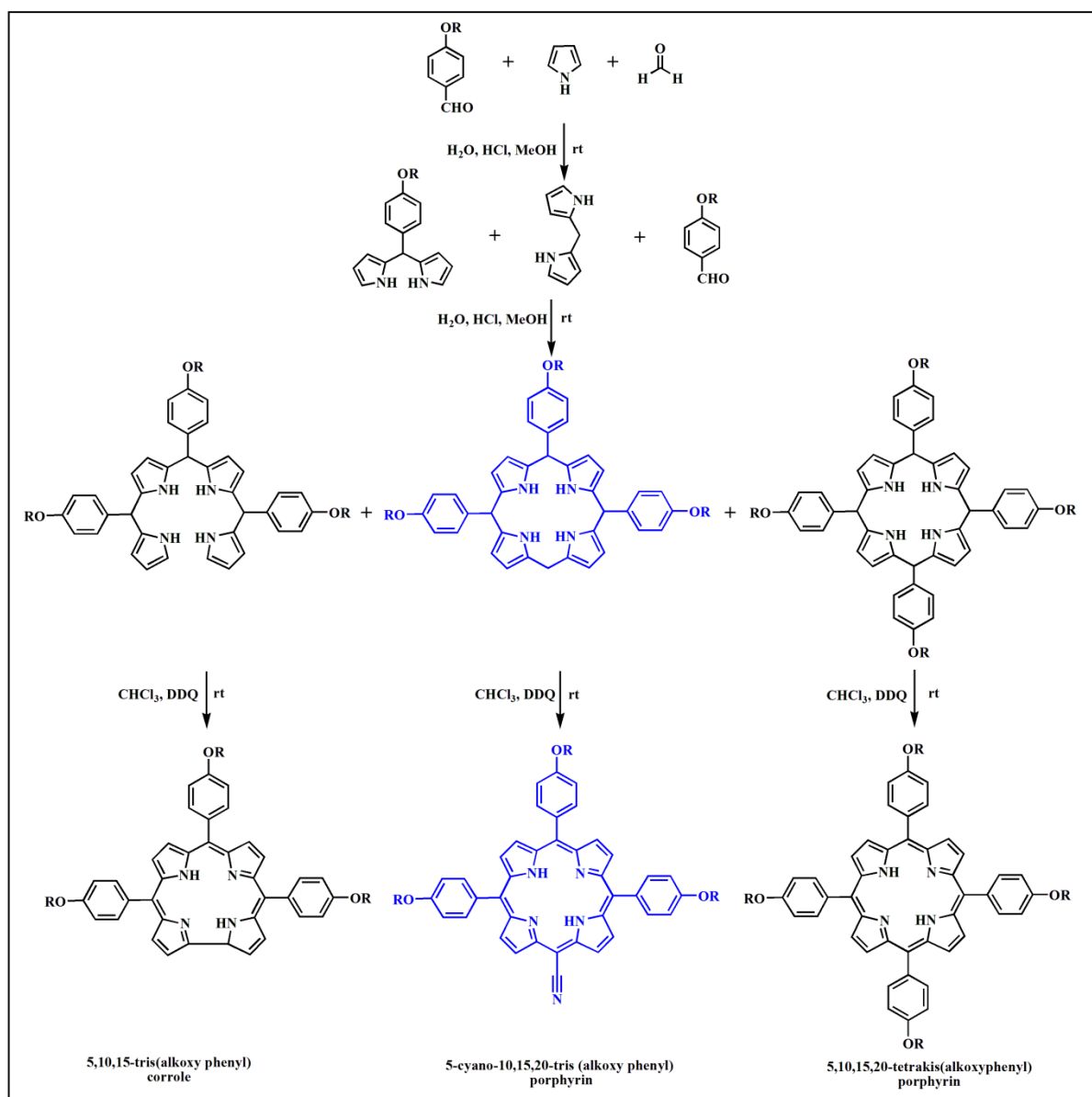


Figure 2.10. Mass spectrum (GC-EIMS) of tetrapyrane detected by GC of the reaction mixture.

2-yl)methane and unsubstituted tetrapyrane further confirmed the presence of the formyl group in the reaction mixture. Incidentally 5, 10, 15, 20-tetrakis (alkoxyphenyl)porphyrin was never obtained when 4-tertiarybutyloxy benzaldehyde was used. However the corresponding symmetric porphyrin was always obtained when 4-methoxy benzaldehyde was used. The combination of the H₂O/HCl/MeOH system and DDQ always resulted in the formation of 5,10,15-tris(alkoxyphenyl)corrole in low yields (2-3%). However the combination of

H₂O/HCl/MeOH system and chloranil resulted in a varied mixture of 5,10,15-tris(alkoxyphenyl)corrole (4-5%) and 5,10,15,20-tetrakis(alkoxyphenyl)porphyrin (2-3%). In this case formation of 5-cyano-10,15,20-tris(alkoxyphenyl)porphyrins was not observed. This clearly showed that the *meso*-cyano group comes exclusively from DDQ. It was observed that depending on the quality of methanol solvent used, the yield of 5-cyano-10, 15, 20-tris(alkoxyphenyl)porphyrins, 5,10,15,20-tetrakis(alkoxyphenyl)porphyrin and 5,10,15-tris(alkoxyphenyl)corrole varied. In an ultrapure methanol, the yield of our desired compound drastically decreased and correspondingly the yield of the symmetric porphyrin and corrole reached up to 3-4%. Based on GC-Mass analysis of the reaction intermediates (Scheme 2.3) the following mechanism has been proposed for the formation of *meso*-cyanoporphyrin. Three different intermediates (Figures 2.11, 2.12, 2.14, and 2.16; and one product (Figures 2.11, 2.13, and 2.15) have been identified by gas chromatography-mass spectrometry (GC-EIMS) during the acid catalyzed condensation reaction of pyrrole and the corresponding *para*-alkoxy benzaldehyde. The overall reaction proceeds in two steps: (i) formation of a porphyrinogen, and (ii) conversion of the porphyrinogen to *meso*-cyanoporphyrin by DDQ. Stepwise addition of H₂O/HCl/MeOH to a mixture of pyrrole and the corresponding *para*-alkoxybenzaldehyde, e.g., 4-*tert*-butoxy benzaldehyde, results in the formation of a dipyrromethane, namely 5-(4-*tert*-butoxyphenyl)dipyrromethane (Figure 2.14). It is observed that another dipyrromethane is formed by the condensation of pyrrole with formaldehyde (Figure 2.16), and presumably promoted by the H₂O/HCl/MeOH mixture. Although formaldehyde was not deliberately added to the reaction mixture, di(1*H*-pyrrol-2-yl)methane formed in the reaction vessel. The probable reason for its formation is the presence of traces of formaldehyde as an impurity in the solvent, methanol. In the next step both the dipyrromethanes, 5-(4-*tert*-butoxy phenyl)dipyrromethane, dipyrromethane, and the corresponding aldehyde, e.g. 4-*tert*-butoxybenzaldehyde, condense and form the desired



Scheme 2.3. Mechanistic presentation of the formation of cyanoporphyrins.

intermediate compound, 5,10,15-tri(4-*tert*-butoxyphenyl)porphyrinogen (Figure 2.13 & 2.15). Hydrogen atoms at the *meso* positions of the 5,10, 15-tri(4-*tert*-butoxyphenyl)porphyrinogen are highly susceptible to oxidation. In the second step DDQ not only oxidizes the porphyrinogen to the corresponding porphyrin but also performs the cyanation reaction simultaneously. It has been assumed that the reaction proceeds *via* the formation of an adduct between DDQ and the porphyrin^{38,39} and subsequent intermolecular transfer of a cyanide

ion.^{40,41} Further research is going on in our laboratory to elucidate the detailed mechanism of the formation of cyanoporphyrin.

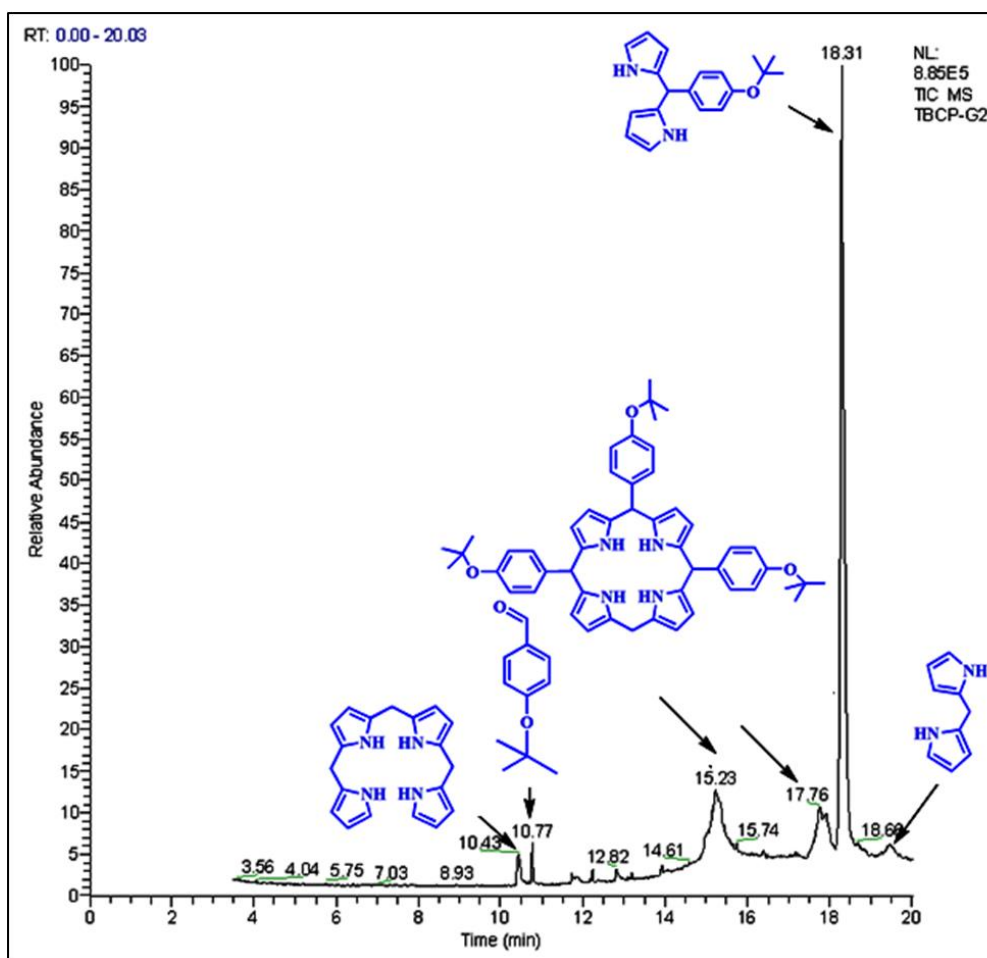


Figure 2.11. GC-EIMS analysis of the reaction mixture: 4-*tert*-butoxybenzaldehyde and pyrrole were dissolved in (1:1) MeOH and water mixture. After addition of conc. HCl, the reaction mixture was stirred continuously at room temperature. Aliquots of this reaction mixture were taken after two hours interval and were monitored by GC-EIMS analysis.

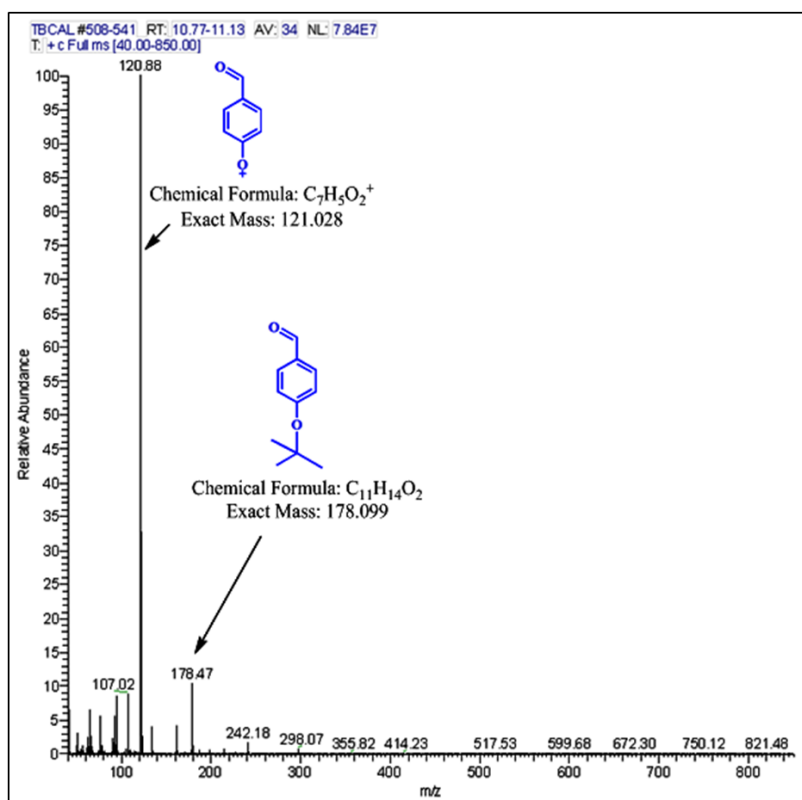


Figure 2.12. Mass spectrum (GC-EIMS) of 4-*tert*-butoxybenzaldehyde detected by GC of the reaction mixture.

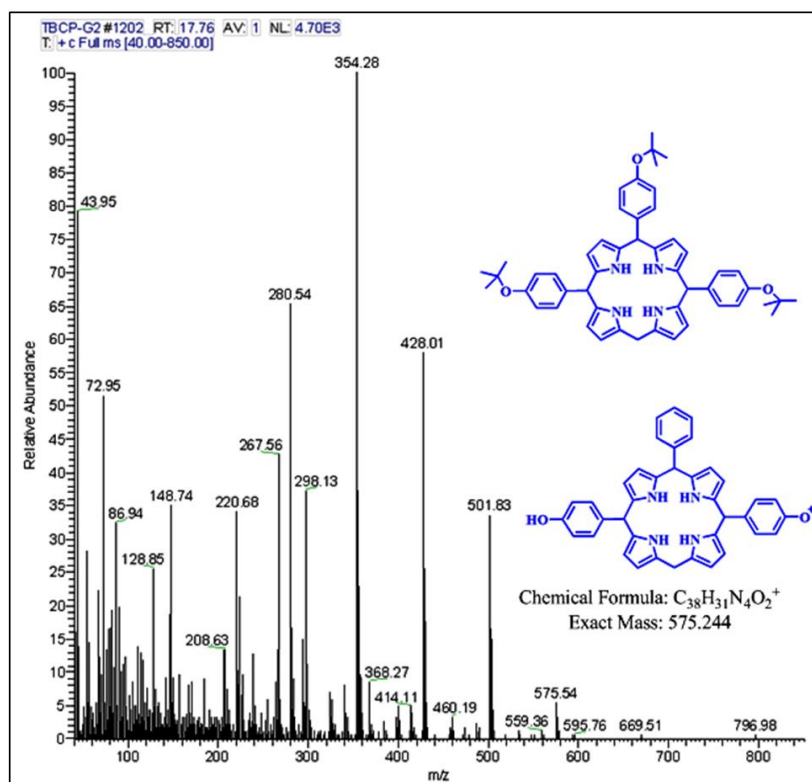


Figure 2.13. Mass spectrum (GC-EIMS) of 5, 10, 15-tri(4-*tert*-butoxy phenyl)porphyrinogen detected by GC of the reaction mixture.

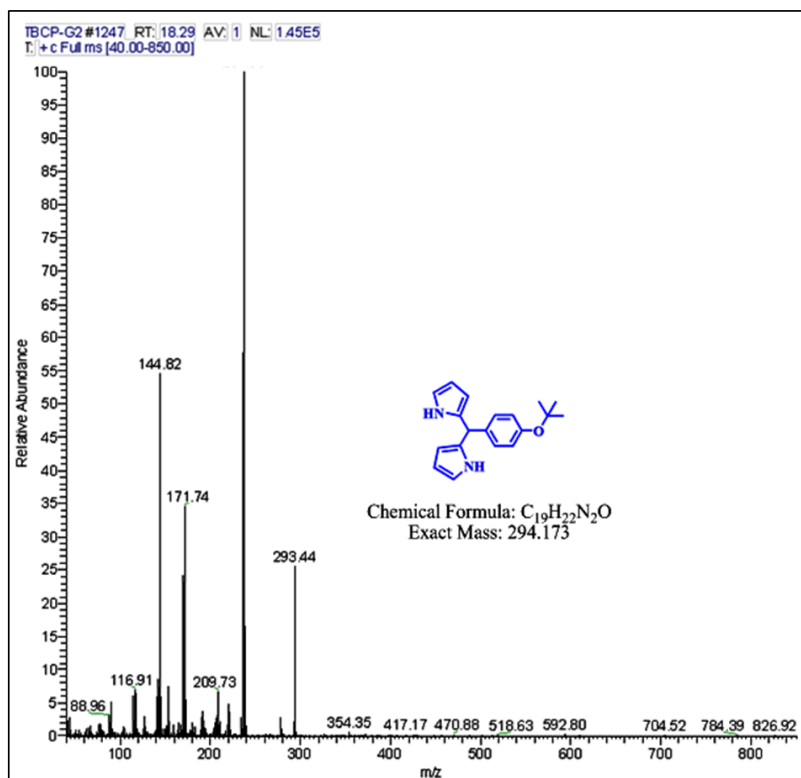


Figure 2.14. Mass spectrum (GC-EIMS) of 5-(4-*tert*-butoxy phenyl)dipyrromethane detected by GC of the reaction mixture.

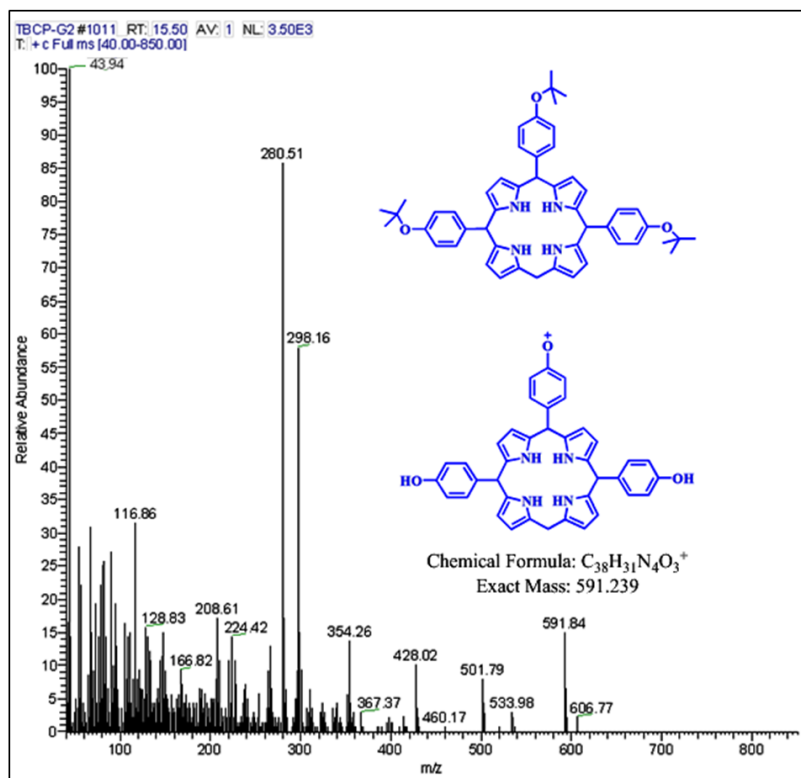


Figure 2.15. Mass spectrum (GC-EIMS) of 5,10,15-tri(4-*tert*-butoxy phenyl)porphyrinogen detected by GC of the reaction mixture.

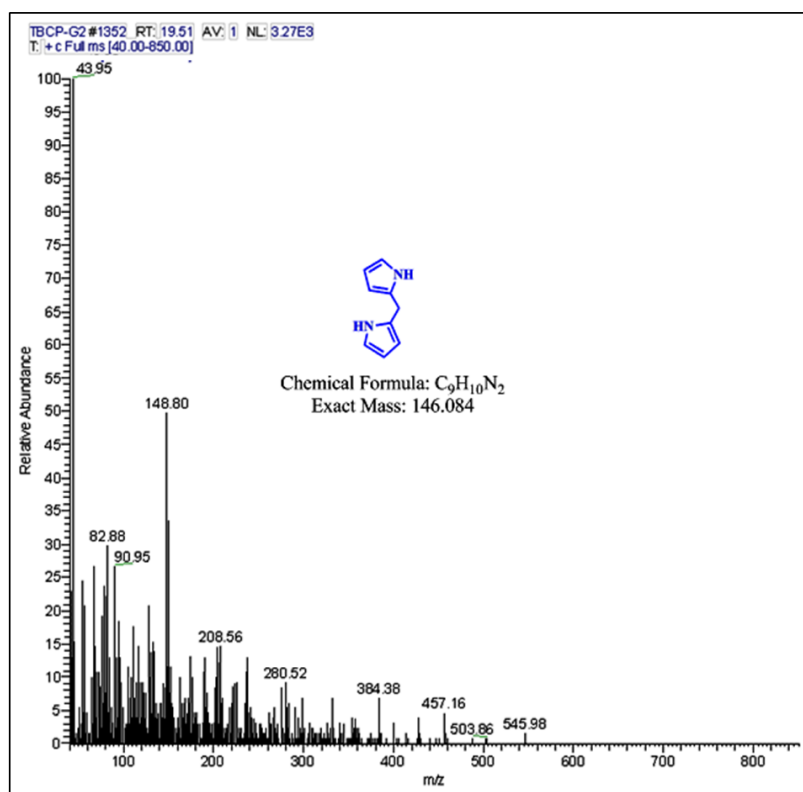


Figure 2.16. Mass spectrum (GC-EIMS) of dipyrromethane detected by GC of the reaction mixture.

2.4. Conclusions

In conclusion, we have developed an entirely new route to synthesize cyano substituted porphyrins. The new methodology does not need any porphyrin or metalloporphyrin based starting material. In addition to the new route for the synthesis of the cyano-porphyrins, one representative crystal structure, (porphyrin **2**), and their spectroscopic properties have also been described. The use of the $H_2O/HCl/MeOH$ system to synthesize porphyrins is completely unconventional and the use of DDQ as sole reagent in cyanation reaction is unique. Although at present our approach is limited to the nature of aldehydes, further studies are proceeding in this direction which will make it a very useful route to synthesize various substituted porphyrin-based derivatives.

2.5 Experimental Section

2.5.1 Materials and Methods

The precursor compounds 4-tertiarybutyloxy benzaldehyde, pyrrole, and DDQ (2, 3-dichloro-5,6-dicyano-1,4-benzoquinone) were purchased from Sigma-Aldrich, USA. 4-Methoxy benzaldehyde was purchased from Merck, India. All other chemicals and solvents were reagent grade and were used as received. For spectroscopy and electrochemical studies, HPLC grade solvents were used.

2.5.2 Physical Measurements

UV–Vis spectral studies were performed on a Perkin-Elmer LAMBDA-750 spectrophotometer. Emission spectral studies were performed on a Perkin Elmer, LS 55 spectrophotometer using an optical cell of 1 cm path length. The fluorescence quantum yields were determined using tetraphenylporphyrin, [TPP] as a reference. Time resolved fluorescence measurements were carried out using a time-correlated single photon counting (TCSPC) spectrometer (Edinburgh, OB 920). The elemental analyses were carried out with a Perkin-Elmer 240C elemental analyzer. GC-EIMS spectra were taken on a Thermo Scientific ITQ 900 spectrometer. FTIR spectra were recorded on a Perkin-Elmer spectrophotometer with samples prepared as KBr pellets. The NMR measurements were carried out using a Bruker AVANCE 400 NMR spectrometer. Tetramethylsilane (TMS) was the internal standard. Electrospray mass spectra were recorded on a Bruker Micro TOF-QII mass spectrometer.

2.5.3 Crystal Structure Determination

Single crystals of the porphyrin **2** were grown by slow diffusion of a solution of the porphyrin in acetonitrile into benzene, followed by slow evaporation under atmospheric conditions. The crystal data of porphyrin **2** was collected on a Bruker Kappa APEX II CCD diffractometer at 293 K. Selected data collection parameters and other crystallographic results are summarized

in Table 2.1. All data were corrected for Lorentz polarization and absorption effects. The program package SHELXTL⁴² was used for structure solution and full matrix least squares refinement on F^2 . Hydrogen atoms were included in the refinement using the riding model. Contributions of H atoms for the water molecules were included, but not fixed. Disordered solvent molecules were taken out using the SQUEEZE⁴³ command in PLATON.

2.5.4 Synthesis of Porphyrin 1

In a 1L round bottomed flask, 4-methoxy benzaldehyde (0.679 g, 5 mmol) and pyrrole (670 μ L, 10 mmol) were dissolved in 200mL MeOH. Reagent grade MeOH was a better choice for this synthesis. In the case of extra pure MeOH, one drop (0.05 mL) of formaldehyde solution can be added. Water (200 mL) was immediately added to this reaction mixture. After the addition of conc. HCl (36%, 4.25 mL), the reaction mixture was stirred continuously for 3h at room temperature. During the course of the reaction, the color of the mixture changed from orange to dark green to dark brown. The progress of the reaction was monitored periodically by TLC. For this purpose, aliquots from the reaction mixture were removed and extracted by using CHCl_3 , washed a couple of times with water and then oxidized by DDQ in CHCl_3 solution. Migration of TLC plates (silica, 90% CH_2Cl_2 + 10% hexane) and illumination under UV light showed three bright red fluorescent bands. The lower one was for the symmetric porphyrin, the middle one for cyanoporphyrin and the upper band was for corrole. $R_f = 0.5$ (silica, 90% CH_2Cl_2 + 10% hexane) for cyanoporphyrin. The product was then extracted from the water-methanol mixture using CHCl_3 . The organic layer was collected, washed thoroughly with water and dried using anhydrous Na_2SO_4 . The volume of the CHCl_3 solution was made up to 300 mL. DDQ (0.573g, 2.5 mmol) was then added to this solution and the reaction mixture was stirred for an hour in dark condition. After one hour the TLC was repeated and the same pattern of three fluorescent bands was observed, showing no further progress of the reaction with time. The solvent was dried and the compound was filtered

through a column of silica. The final purification was done using column chromatography (silica, 100-200 mesh, 90% CH₂Cl₂ + 10% hexane as eluent). Five distinct bands were observed during chromatographic purification of the crude reaction mixture. The first yellow color fraction was identified in comparison with an authentic sample as DDQ. The second black color fraction was never identified. The third green color fraction with red fluorescence was identified as corrole. Fourth red fraction with bright red fluorescence was identified as desired cyanoporphyrin. The fifth red band was eluted with pure CH₂Cl₂. The crude fourth fraction was subsequently crystallized from a solvent mixture of acetone and hexane. The final form of the pure compound was obtained as a pink-red crystalline material.

For **porphyrin 1**: Yield: 3.5% (29 mg). Anal. Calcd. for C₄₂H₃₁N₅O₃ (**1**): C, 77.17; H, 4.78; N, 10.71. Found: C, 77.28; H, 4.59; N, 10.85%. λ_{max}/nm ($\epsilon/M^{-1}cm^{-1}$) in toluene: 425 (320000), 521 (17333), 559 (13333), 596 (8600), 651 (4000). IR (cm⁻¹) $\nu_{C\equiv N}$: 2211 cm⁻¹. ¹H NMR (400 MHz, CDCl₃, 298K) δ : 9.55 (d, $J = 4.77$ Hz, 2 H), 9.02 (d, $J = 5.13$ Hz, 2 H), 8.78 - 8.88 (m, 4 H), 8.07-8.14 (m, 6 H), 7.27-7.34 (m, 6 H), 4.09-4.12 (m, 9 H), -2.34 (s, 2 H). ¹³C NMR (100 MHz, CDCl₃, 298K) δ : 159.9, 159.5, 135.7, 135.7, 134.8, 134.1, 133.4, 125.4, 122.5, 122.5, 119.9, 112.7, 112.5, 112.3, 84.2, 55.8, 55.7, 55.7. The electrospray mass spectrum in acetonitrile (Figure 2.1) showed the peaks centred at $m/z = 654.62$ corresponding to $[M+H]^+$ (calculated molecular mass: 653.72). M.p>300°C. The porphyrin **1** displayed strong fluorescence at 658 nm and 722 nm (Figure 2.7.a) with a quantum yield $\phi = 0.11$ at room temp in toluene solvent. The fluorescence lifetime of porphyrin **1** was estimated to be 7.56 ns.

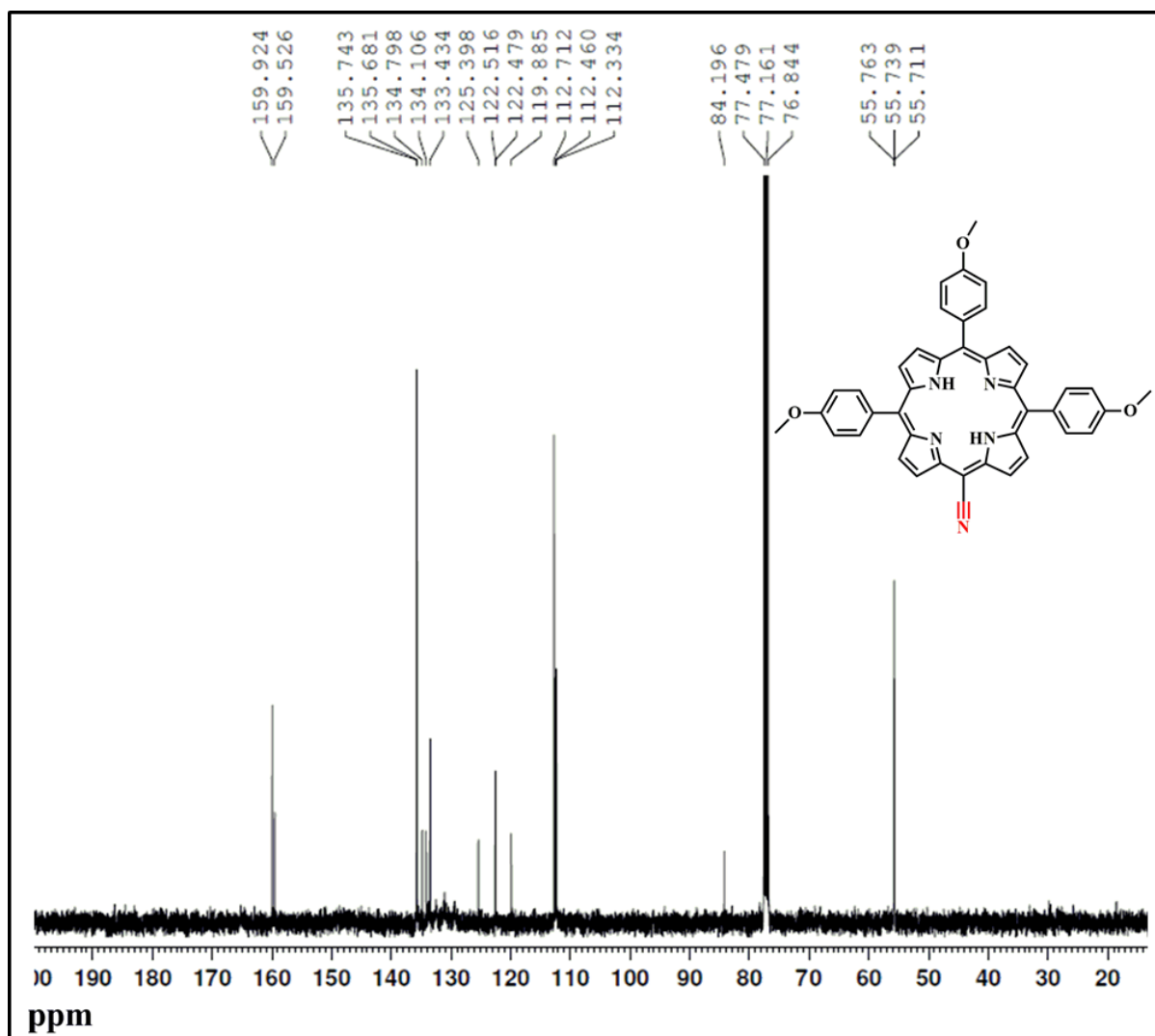


Figure 2.17. ^{13}C NMR spectrum of porphyrin **1** in CDCl_3 .

2.5.5 Synthesis of Porphyrin 2

In a 1L round bottomed flask, 4-tertiarybutyloxy benzaldehyde (0.89g, 5 mmol) and pyrrole (670 μL , 10 mmol) were dissolved in 200 mL MeOH. Reagent grade MeOH was a better choice for this synthesis. In case of extra pure MeOH, one drop (0.05 mL) of formaldehyde solution can be added. Water (200 mL) was immediately added to this reaction mixture. After the addition of conc. HCl (36%, 4.25 mL), the reaction mixture was stirred continuously for three hours at room temperature. During the course of the reaction, the mixture changed color from orange to dark green to dark brown. The progress of the reaction was monitored periodically by TLC. For this purpose, aliquots from the reaction mixture were removed and

extracted using CHCl_3 , washed a couple of times with water and oxidized by DDQ in CHCl_3 solution. Migration of TLC plates (silica, 90% CH_2Cl_2 + 10% hexane) and illumination under UV light showed two bright red fluorescent spots. The lower one was for cyanoporphyrin and the upper one was for corrole. $R_f = 0.2$ (silica, 90% CH_2Cl_2 + 10% hexane) for the cyanoporphyrin. After this reaction, the product was extracted from a water-methanol mixture using CHCl_3 . The organic layer was collected, washed thoroughly with water and dried using anhydrous Na_2SO_4 . The volume of the CHCl_3 solution was made up to 300 mL. DDQ (0.573g, 2.5 mmol) was then added to this solution and the reaction mixture was stirred for an hour in dark condition. After one hour, the TLC was repeated and the same pattern of two fluorescent bands was observed, showing no further progress of the reaction with time. The solvent was dried and the compound was filtered through a column of silica. The final purification was done using column chromatography (silica, 100-200 mesh, 90% CH_2Cl_2 + 10% hexane as eluent). Four distinct bands were observed during the chromatographic purification of the crude reaction mixture. The first yellow colour fraction was identified in comparison with an authentic sample as DDQ. The second black colour fraction was never identified. The third green colour fraction with red fluorescence was identified as corrole and the fourth red fraction with bright red fluorescence was identified as the desired cyanoporphyrin. This crude fourth fraction was subsequently crystallized from a solvent mixture of acetone and hexane. The final form of pure compound was obtained as a pink red crystalline material.

For **porphyrin 2**: Yield: 2.1% (20 mg). Anal. Calcd. for $\text{C}_{51}\text{H}_{49}\text{N}_5\text{O}_3$ (**2**): C, 78.53; H, 6.33; N, 8.98. Found: C, 78.63; H, 6.46; N, 8.85%. λ_{max}/nm ($\epsilon/M^{-1}\text{cm}^{-1}$) in toluene: 425(386000), 522(15867), 559(10667), 594(4667), 649(2667). IR (cm^{-1}) $\nu_{\text{C}=\text{N}}$: 2218 cm^{-1} . ^1H NMR (400 MHz, CDCl_3 , 298K) δ : 9.57 (d, $J=4.95$ Hz, 2 H), 9.03 (d, $J=4.95$ Hz, 2 H), 8.70-8.84 (m, 4 H), 8.0-8.1 (m, 6 H), 7.35-7.43 (m, 6 H), 1.57-1.64 (m, 27 H), -2.36 (m, 2 H). ^{13}C

NMR (100 MHz, CDCl₃, 298K) δ : 156.01, 155.98, 136.50, 135.85, 135.26, 135.17, 125.38, 122.56, 122.46, 122.23, 84.37, 79.31, 79.30, 29.85, 29.81, 29.51, 29.32, 29.30. The

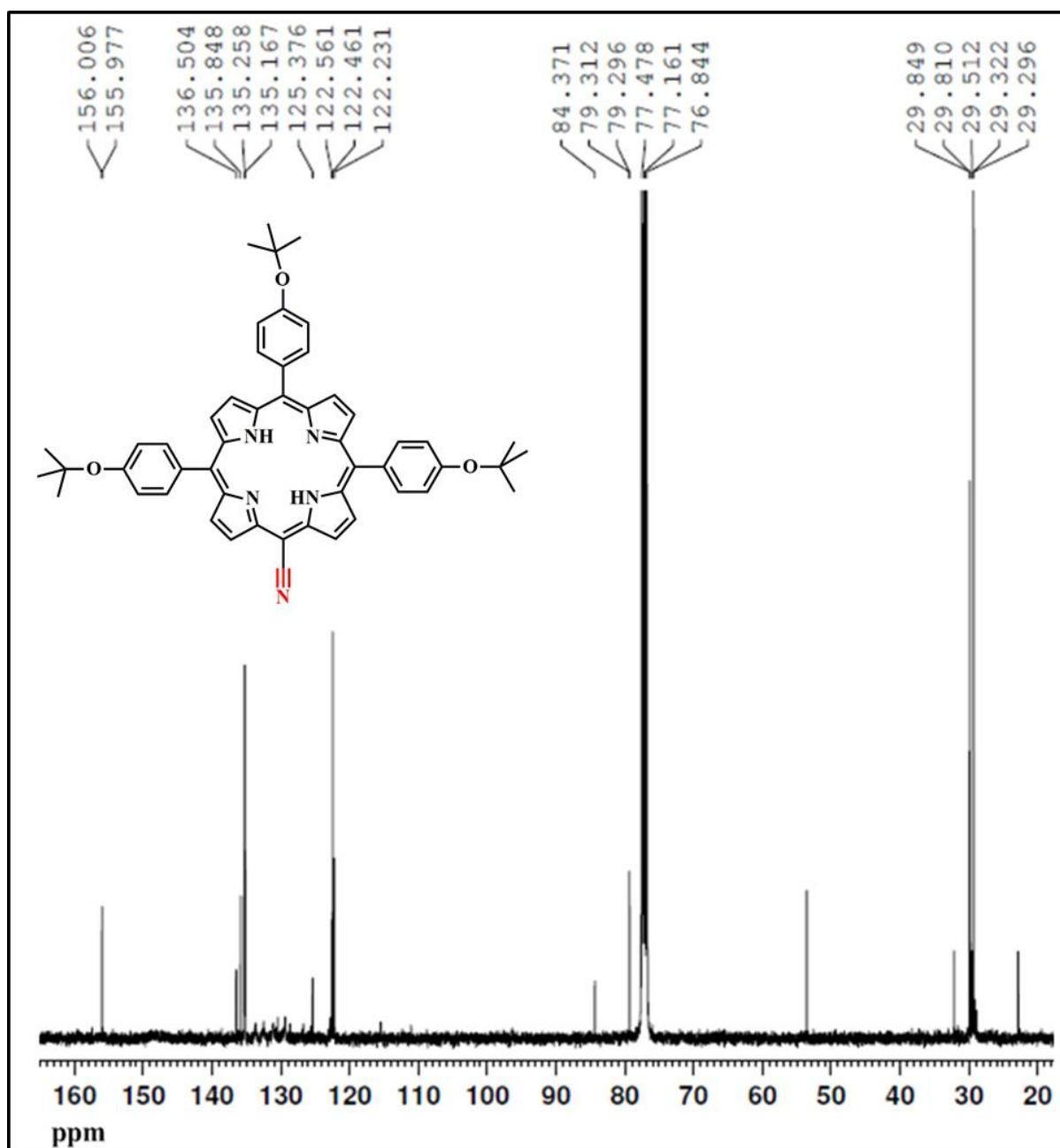


Figure 2.18. ¹³C NMR spectrum of porphyrin 2 in CDCl₃

electrospray mass spectrum in acetonitrile (Figure 2.2) showed the peaks centered at $m/z = 780.4$ corresponding to $[2+H]^+$ (calculated molecular mass:779.38). M.p>300°C. The porphyrin 2 displayed strong fluorescence at 656 nm and 719 nm (Figure 2.7.b) with a

quantum yield $\phi = 0.10$ at room temp in toluene. The fluorescence lifetime of porphyrin **2** was estimated to be 9.08 ns.

References

1. Kadish, K. M.; Smith, K. M.; Guillard, R., *The Porphyrin Handbook*. Academic Press: San Diego, **1999-2003**; vol. 1-20.
2. Rappoport, Z., *The Chemistry of the Cyano Group*. Interscience Publishers: London, **1970**.
3. Larock, R. C., *Comprehensive Organic Transformations*. 2nd ed.; Wiley-VCH: New York, **1999**.
4. Takanami, T.; Hayashi, M.; Chijimatsu, H.; Inoue, W.; Suda, K., *Org. Lett.*, **2005**, 7, 3937-3940.
5. Callot, H. J., *Tetrahedron Lett.*, **1973**, 14, 4987-4990.
6. Callot, H. J., *Bull. Soc. Chim. Fr.*, **1974**, 1492-1496.
7. Richeter, S.; Jeandon, C.; Kyritsakas, N.; Ruppert, R.; Callot, H. J., *J. Org. Chem.*, **2003**, 68, 9200-9208.
8. Inhoffen, H. H.; Fuhrhop, J.-H.; Voigt, H.; Brockmann, H., *Jr. Liebigs, Ann. Chem.*, **1966**, 133-145.
9. Johnson, A. W.; Oldfield, D., *J. Chem. Soc.C*, **1966**, 794-798.
10. Smith, K. M.; Barnett, G. H.; Evans, B.; Martynenko, Z., *J. Am. Chem. Soc.*, **1979**, 101, 5953-5961.
11. Callot, H. J.; Louati, A.; Gross, M., *Tetrahedron Lett.*, **1980**, 21, 3281-3284.
12. Wu, G.-Z.; Leung, H.-K.; Gan, W.-X., *Tetrahedron*, **1990**, 46, 3233-3244.
13. Smith, K. M.; Goff, D. A.; Simpson, D. J., *J. Am. Chem. Soc.*, **1985**, 107, 4946-4954.
14. Sharman, W. M.; Lier, J. E. V., *J.Porphyrins Phthalocyanines*, **2000**, 04, 441-453.
15. DiMagno, S. G.; Lin, V. S.-Y.; Therien, M. J., *J. Am. Chem. Soc.*, **1993**, 115, 2513-2515.
16. DiMagno, S. G.; Lin, V. S.-Y.; Therien, M. J., *J. Org. Chem.*, **1993**, 58, 5983-5993.

17. Chan, K. S.; Zhou, X.; Au, M. T.; Tam, C. Y., *Tetrahedron*, **1995**, *51*, 3129-3136.
18. Boyle, R. W.; Johnson, C. K.; Dolphin, D. J., *Chem. Soc., Chem. Commun.*, **1995**, 527-528.
19. Hyslop, A. G.; Kellett, M. A.; Iovine, P. M.; Therien, M. J., *J. Am. Chem. Soc.*, **1998**, *120*, 12676-12677.
20. Shanmugathasan, S.; Johnson, C. K.; Edwards, C.; Matthews, E. K.; Dolphin, D.; Boyle, R. W., *J. Porphyrins Phthalocyanines*, **2000**, *4*, 228-232.
21. Deng, Y.; Chang, C. K.; Nocera, D. G., *Angew Chem., Int. Ed.*, **2000**, *39*, 1066-1068.
22. Vaz, B.; Alvarez, R.; Nieto, M.; Paniello, A. I.; de Lera, A. R., *Tetrahedron Lett.*, **2001**, *42*, 7409-7412.
23. Chng, L. L.; Chang, C. J.; Nocera, D. G., *J. Org. Chem.*, **2003**, *68*, 4075-4078.
24. Chen, Y.-J.; Lee, G.-H.; Peng, S.-M.; Yeh, C.-Y., *Tetrahedron Lett.*, **2005**, *46*, 1541-1544.
25. Kurotobi, K.; Osuka, A., *Org. Lett.*, **2005**, *7*, 1055-1058.
26. Hata, H.; Shinokubo, H.; Osuka, A., *J. Am. Chem. Soc.*, **2005**, *127*, 8264-8265.
27. Takanami, T.; Hayashi, M.; Hino, F.; Suda, K., *Tetrahedron Lett.*, **2003**, *44*, 7353-7357.
28. Chen, Y.; Zhang, X. P., *J. Org. Chem.*, **2003**, *68*, 4432-4438.
29. Gao, G.-Y.; Colvin, A. J.; Chen, Y.; Zhang, X. P., *Org. Lett.*, **2003**, *5*, 3261-3264.
30. Gao, G.-Y.; Chen, Y.; Zhang, X. P., *Org. Lett.*, **2004**, *6*, 1837-1840.
31. Gao, G.-Y.; Colvin, A. J.; Chen, Y.; Zhang, X. P., *J. Org. Chem.*, **2004**, *69*, 8886-8892.
32. Král, V.; Vašek, P.; Dolensky, B., *Collect. Czech. Chem. Commun.*, **2004**, *69*, 1126-1136.
33. Koszarna, B.; Gryko, D. T., *J. Org. Chem.*, **2006**, *71*, 3707-3717.

34. Silvers, S. J.; Tulinsky, A., *J. Am. Chem. Soc.*, **1967**, *89*, 3331-3337.
35. Byrn, M. P.; Curtis, C. J.; Khan, S. I.; Sawin, P. A.; Tsurumi, R.; Strouse, C. E., *J. Am. Chem. Soc.*, **1990**, *112*, 1865-1874.
36. Sugiura, K.; Ushiroda, K.; Tanaka, T.; Sawada, M.; Sakata, Y., *Chem. Lett.*, **1997**, 927-928.
37. Orpen, A. G.; Brammer, L.; Allen, F. H.; Kennard, O.; Watson, D. G.; Taylor, R., in: *Structure Correlation* (Eds. Bürgi, H. -B., Dunitz, J. D.), VCH Publishers: Weinheim, Germany, **1994**; vol. 2.
38. Kano, K.; Hayakawa, T.; Hashimoto, S., *Bull. Chem. Soc. Jpn.*, **1991**, *64*, 778-784.
39. Mohajer, D.; Dehghani, H., *J. Chem. Soc., Perkin Trans. 2*, **2000**, 199-205.
40. Saito, I.; Shimosono, K.; Matsuura, T., *J. Am. Chem. Soc.*, **1983**, *105*, 963-970.
41. Bury, A.; Bougeard, P.; Corker, S. J.; Johnson, M. D.; Perlmann, M., *Chem. Soc. Perkin Trans. 2*, **1982**, 1367-1372.
42. Sheldrick, G., *Acta Crystallographica Section A*, **2008**, *64*, 112-122.
43. Sluis, P. V. d.; Spek, A. L., *Acta Crystallogr., Sect. A: Found. Crystallogr.*, **1990**, *46*, 194-201.

CHAPTER 3

Synthesis, Electron Transports, and Charge Storage Properties of Fullerene-Zinc Porphyrin Hybrid Nanodiscs

- 3.1 Abstract
- 3.2 Introduction
- 3.3 Results and Discussion
 - 3.3.1 Synthesis and Characterization
 - 3.3.2 Growth Mechanism
 - 3.3.3 X-ray Structural Studies of **ZnTANP**
 - 3.3.4 Electronic Spectra
 - 3.3.5 X-ray Photoelectron Spectroscopy (XPS)
 - 3.3.6 X-ray Diffraction (XRD)
 - 3.3.7 *I-V* Characteristics
 - 3.3.8 *C-V* Characteristics
- 3.4 Conclusions
- 3.5 Experimental Section
 - 3.5.1 Materials
 - 3.5.2 Characterization
 - 3.5.3 Crystal Structure Determination
 - 3.5.4 Preparation of C₆₀-ZnTANP Hybrid Material

3.1 Abstract



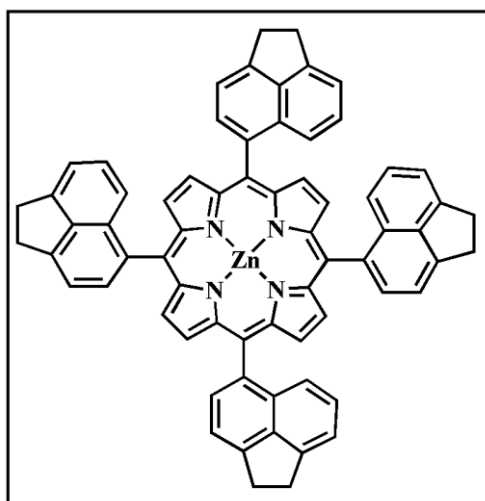
A donor (D)-acceptor (A) based system has been developed with the help of a newly synthesized Zn-porphyrin complex and C_{60} fullerene. A series of spectroscopic methods, absorption spectroscopy (UV-Vis-NIR), powder X-ray diffraction (XRD), and X-ray photoelectron spectroscopy (XPS) measurements confirm the existence of a charge transfer based complex between Zn-porphyrin and C_{60} fullerene. By using this D-A based system, circular discs like nano-objects have been generated. With the help of these nano objects, a diode has been fabricated. Current-voltage (I-V) and the capacitance-voltage (C-V) analyses of the diode were performed. The critical role of the Ag- C_{60} -Zn-porphyrin and C_{60} -Zn-porphyrin- SiO_x interfaces is clearly understood from the I-V characteristic of the present device. Existence of a hysteresis loop in the C-V plot indicates that the device is indeed suitable for charge storage applications.

3.2 Introduction

Due to their unique physical and chemical properties, fullerenes have found extensive applications in many areas, including *n*-type semiconductors,¹ solar cells,² organic field effect transistors,³ superconductor,⁴ and medicine.⁵ The major route towards the synthesis of various self-assembled fullerene systems involves their chemical modifications by attachment of various functional groups.⁶⁻¹⁰ However, the controlled synthesis of nano- and micro-structures, bearing unmodified fullerene, is still a challenging task. Similarly, porphyrin based materials have also been extensively studied as photoconductors.¹¹ Uses of porphyrin based nano-architectures as electron transport materials are also explored.¹² Fullerene (C₆₀), with triply degenerate lowest unoccupied molecular orbitals (LUMO), which are susceptible to six electrons reduction under ambient conditions, and zinc-porphyrin, with a large excess of π -electron density and a closed shell central metal like zinc, are known to be a potential donor-acceptor pair.¹³ These porphyrin-fullerene dyads are known to exhibit rich physical properties,¹⁴ viz. metallic,¹⁵ magnetic,¹⁶ luminescent,¹⁷ and nonlinear optical (NLO) properties.¹⁸ Recently, polymer (D)-fullerene (A) pair has been successfully used in organic photovoltaic devices and was observed that the device performance was highly dependent on the morphology of each of the components.¹⁹⁻²¹ Thus, it can be assumed that the donor (D)-acceptor (A) based nano-architectures will have tremendous potential for the development of various micro/nano-sized devices. In this context, porphyrin-fullerene dyads will be a perfect choice to design various nano-architectures and test their suitability for various practical applications in materials science.

Till date, only limited information is available regarding the nano-architectures bearing porphyrin-fullerene dyads.²²⁻²⁸ Very recently, Wakahara *et al.*²⁹ synthesized fullerene-cobalt porphyrin hybrid nanosheets which exhibit ambipolar characteristics. Kamat *et al.*³⁰ have prepared fullerene-porphyrin nanoclusters and explored its efficacy for the

generation of photocurrent. Valli *et al.*²⁵ prepared thin films of porphyrin-fullerene and measured its effectiveness in solar energy harvesting. Nishino *et al.*³¹ has demonstrated that a single fullerene-porphyrin pair can act as a molecular rectifier. Few recent reports also demonstrate the usefulness of Langmuir-Blodgett (LB) films composed of fullerene–porphyrin layers as efficient current rectifier.^{32,33} To the best of our knowledge, a porphyrin (D)-fullerene (A) based nano-architecture has never been exploited as a metal-insulator-semiconductor (MIS) diode with potential implications in charge storage.³⁴ A novel zinc-porphyrin complex, [5,10,15,20-tetrakis(1,2-dihydro-5-acenaphthylenyl)porphinato]zinc (II), ZnTANP has been synthesized for the first time. The structure of ZnTANP is shown in Scheme 3.1. ZnTANP, which has a flat concave aromatic surface in the close packed 3-D



Scheme 3.1. Molecular structures of the ZnTANP.

structure, was used to form supramolecular assemblies with the C_{60} molecule. Herein we report the synthesis and characterization of novel C_{60} -ZnTANP hybrid materials. Well-defined circular disc-like 3D nanostructures were obtained from C_{60} -ZnTANP solutions in benzene under suitable experimental conditions. By using these C_{60} -ZnTANP circular discs, a diode was fabricated having the following configuration Ag/ C_{60} -ZnTANP circular discs/*p*-Si/Ag. The current rectification properties of this MIS-type diode and its application as a charge storage device have also been explored in this work.

3.3 Results and Discussion

3.3.1 Synthesis and Characterization

Synthesis of H₂TANP

Anhydrous dichloromethane (40 mL) was taken in a 100 mL round bottom flask under nitrogen atmosphere. To this dichloromethane solvent freshly distilled pyrrole (144 μ L, 2.08 mmol) and 5-acenaphthene carboxaldehyde (380 mg, 2.08 mmol) was added. After few minutes TFA (220 mg, 1.93 mmol) was added to this reaction mixture. The reaction mixture was then stirred for another 2 h at inert atmosphere. Finally DDQ (1.16 g, 5.1 mmol) was added to this mixture and it was stirred for 3 h in open air. Final purification was done by using a silica gel column. The yield was 90 mg (19%). Anal. Calcd (found) for C₆₈H₄₆N₄ (H₂TANP): C, 88.86 (88.95); H, 5.04 (5.14); N, 6.10 (5.91). UV-Vis (dichloromethane) λ_{max}/nm ($\epsilon/M^{-1}cm^{-1}$): 427(343000), 517(22940), 552(7490), 590(6761), 647(2699). ¹H NMR (400 MHz, CDCl₃) δ : 2.29 (s, 2 H), 3.66-3.71 (m, 16 H), 6.85-7.01 (m, 4 H), 7.11-7.19 (m, 4 H), 7.28-7.33 (m, 4 H), 7.60-7.67 (m, 4 H), 8.14-8.23 (m, 4 H), 8.55 (d, $J=4.13$ Hz, 8 H). The electrospray mass spectrum in acetonitrile showed the peaks centered at $m/z=919.35$ corresponding to $[M+H]^+$ (calculated molecular mass=918.37). M.p>300°C. H₂TANP displayed strong fluorescence at 655 nm, and 718 nm. The fluorescence lifetime of H₂TANP was estimated to be 10.03 ns.

Synthesis of ZnTANP

H₂TANP, (27 mg, 0.03 mmol) was dissolved in 20 mL of chloroform in a 100 mL R.B. flask. A methanolic (10 mL) solution of Zn(OAc)₂ · 2H₂O (20 mg, 0.091 mmol) was added to this chloroform solution of the porphyrin. Then the mixture was refluxed for 2 h. The colour of the solution changes from purple to pink red during this process. The solvent mixture was removed by using a rotary evaporator. The crude product was dissolved in chloroform (60 mL) and was washed thoroughly with distilled water. Then the solution was

dried by using anhydrous sodium sulphate and was purified by using silica gel column chromatography using CH_2Cl_2 and hexane mixture as an eluent. The yield was 23mg (80%). Anal. Calcd (found) for $\text{C}_{68}\text{H}_{44}\text{N}_4\text{Zn}$: C, 83.13 (83.28); H, 4.51 (4.64); N, 5.70 (5.85). UV-Vis (dichloro methane) $\lambda_{\text{max}}/\text{nm}$ ($\epsilon/\text{M}^{-1}\text{cm}^{-1}$): 428(371320), 550(22740), 588(3098). ^1H NMR (400 MHz, CDCl_3) δ : 3.63-3.72 (m, 16 H), 6.82-7.00 (m, 4 H), 7.09-7.16 (m, 4 H), 7.27 - 7.28 (d, $J=6.60$ Hz, 4 H), 7.61-7.65 (m, 4 H), 8.15-8.26 (m, 4 H), 8.63-8.67 (m, 8 H). (Figure 3.1) ^{13}C NMR (101 MHz, CDCl_3) δ : 151.16, 151.12, 151.10, 151.06, 146.33, 145.67, 138.66, 135.82, 135.34, 135.30, 134.60, 134.50, 134.47, 132.12, 128.17, 123.33, 123.29, 119.18, 118.45, 118.40, 118.05, 30.87, 30.57, 30.20, 29.86, 29.82, 29.52. The electrospray mass spectrum in acetonitrile (Figure 3.2) showed the peaks centered at $m/z = 980.86$ corresponding to $[\text{M}+\text{H}]^+$ (calculated molecular mass: 980.28). M.p>300°C. ZnTANP displayed strong fluorescence at 600 nm and 648 nm. The fluorescence lifetime of ZnTANP was estimated to be 1.02 ns. Purity and identity of the ZnTANP is demonstrated by its

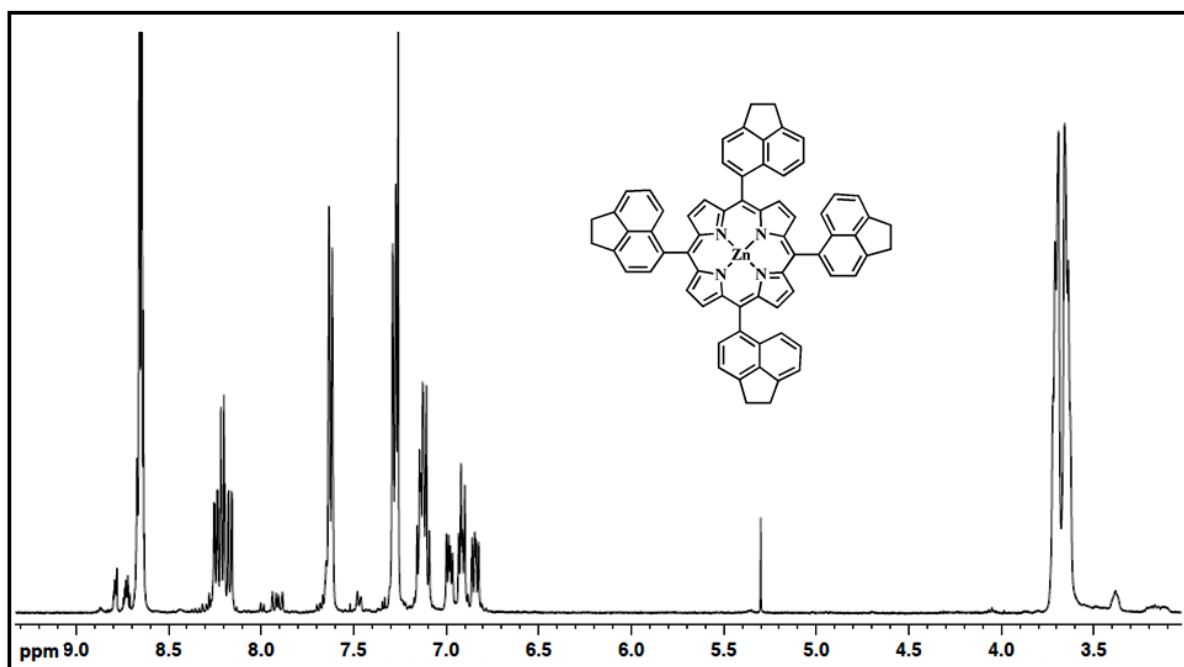


Figure 3.1. ^1H NMR spectrum of ZnTANP in CDCl_3 .

satisfactory elemental analyses, ^1H NMR, and by the electrospray mass spectral data (Figure 3.1 & 3.2). ZnTANP exhibited two successive well-resolved reversible oxidative couples at

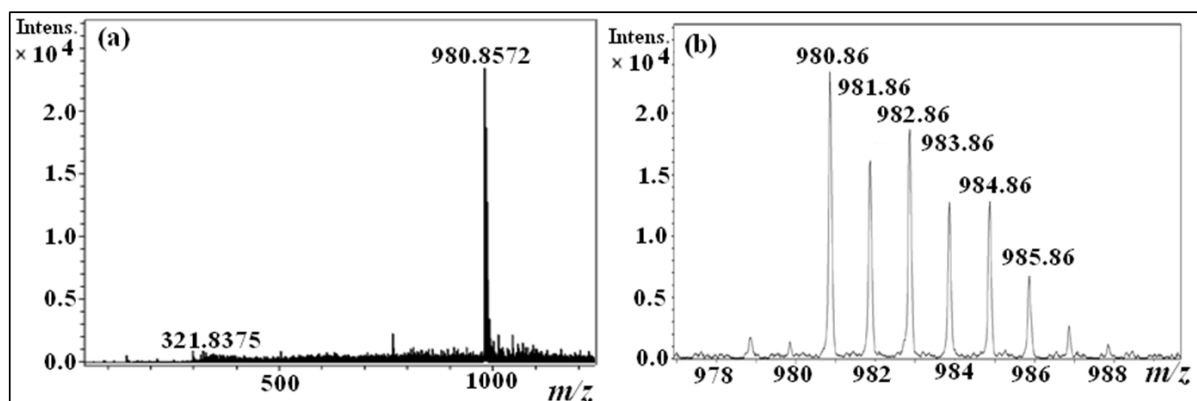


Figure 3.2. ESI-MS spectrum of ZnTANP in CH_3CN shows the (a) measured spectrum and (b) isotopic distribution pattern.

0.27V and 0.51 V. It also showed one well-defined reductive couple at -1.91 V vs ferrocene/ferricinium. The C_{60} -ZnTANP hybrid material was synthesized by slight modifications of a protocol (see Experimental Section) developed by Wakahara *et al.*²⁹ Novel C_{60} -ZnTANP circular discs were synthesized by evaporating a solution of C_{60} -ZnTANP hybrid material in benzene on the silicon substrates by applying spin coating method. Scanning electron microscopy (SEM) images of C_{60} -ZnTANP circular disc-like objects

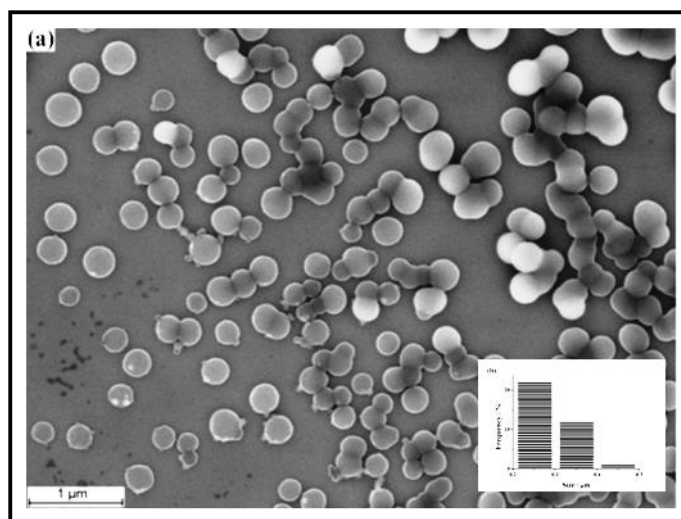


Figure 3.3. (a) SEM images of the C_{60} -ZnTANP circular disc, (b) size distribution histograms of circular discs (inset).

are shown in Figure 3.3, which shows a uniform distribution. The average size of the discs is ~ 250 nm in diameter. Energy dispersive X-ray spectroscopic (EDX) analysis was also performed to analyze the composition of the circular discs. This clearly demonstrates the presence of C, N, and Zn in percentages very near to the 1:1 complex between C_{60} and ZnTANP in the hybrid material (Figure 3.4). Thus, it could be tentatively assigned as 1:1 complex formation between C_{60} and ZnTANP.

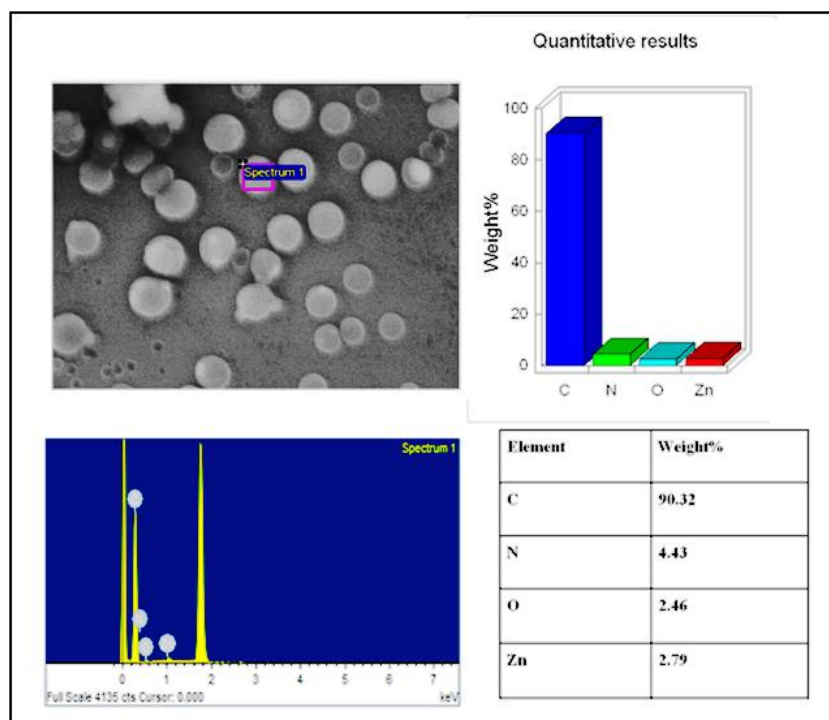


Figure 3.4. EDX spectrum of the C_{60} -ZnTANP circular disc grown on *p*-Si substrate.

3.3.2 Growth Mechanism

In order to get an insight into the growth mechanism, the drying processes of the C_{60} -ZnTANP hybrid material in benzene solution and also several other key conditions (which affects the drying processes), viz. drying inside the desiccators, drying in open air etc. were carefully monitored. In addition, both drop casting and spin coating methods were also performed. The main purpose of all these experiments was to capture few intermediate structures. Careful observations revealed that in few of these cases C_{60} -ZnTANP circular discs were obtained with varying sizes. However, in few of the selected sets we were able to

capture a series of intermediate sized nanoparticles. It was also observed that when the drying process was very fast, a sizeable number of nanoparticles, having disc-like shapes, were also obtained with their average diameter much lesser than the final nanodiscs. In addition, a series of fused dimers and trimers of nanodiscs were also obtained. Based on all these intermediate structures, a tentative mechanism has been proposed towards the formation of C_{60} -ZnTANP circular nanodiscs. It is assumed that during the evaporation process of the C_{60} -ZnTANP hybrid materials in benzene, initially smaller sized nanoparticles are formed. Then these smaller particles assemble and form smaller sized discs. Finally these smaller sized nano-discs aggregate further and form bigger sized nanodiscs as shown in Figure 3.5.

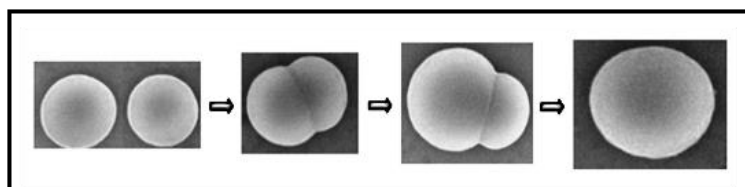


Figure 3.5. Plausible mechanism of C_{60} -ZnTANP circular nanodisc formation *via* aggregations of smaller sized nanodiscs.

3.3.3 X-ray Structural Studies of ZnTANP

The crystal structure analysis of ZnTANP was performed to analyze its tendency to form supramolecular assemblies. The crystal structure of ZnTANP is shown in Figure 3.6. Important crystallographic parameters are presented in Table 3.1.³⁵⁻³⁸ From the crystal structure analysis of ZnTANP, it is observed that the molecules are stacked together by various weak van der Waals forces like π - π stacking interaction (~ 0.364 nm), C-H \cdots N interactions (~ 0.267 nm) and form closely packed 3D structures in the packing diagram (Figure 3.7).³⁵⁻³⁸

Along the crystallographic c -axis it appears that these 3D structures have flat aromatic surfaces. It is assumed that these flat aromatic surfaces facilitate the formation of supramolecular assemblies with the C_{60} molecules.

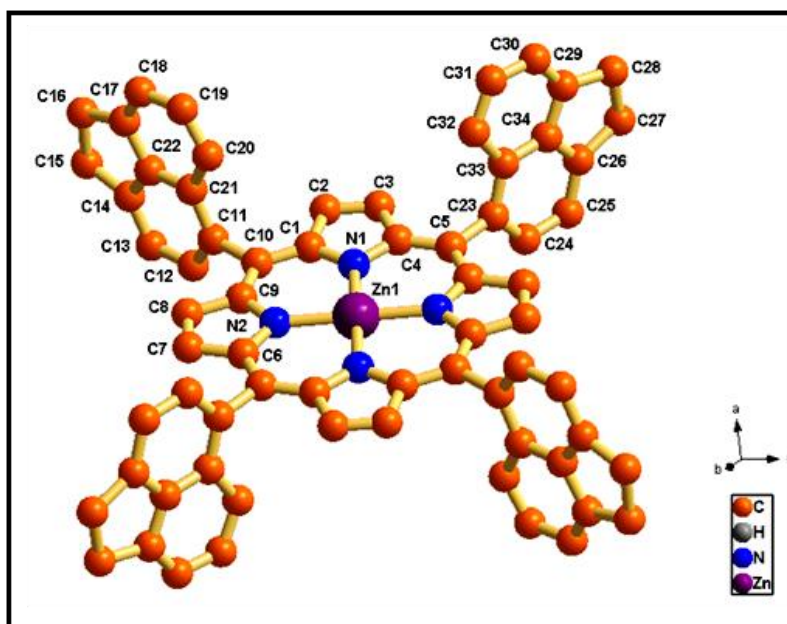


Figure 3.6. Single-crystal X-ray structure of ZnTANP.

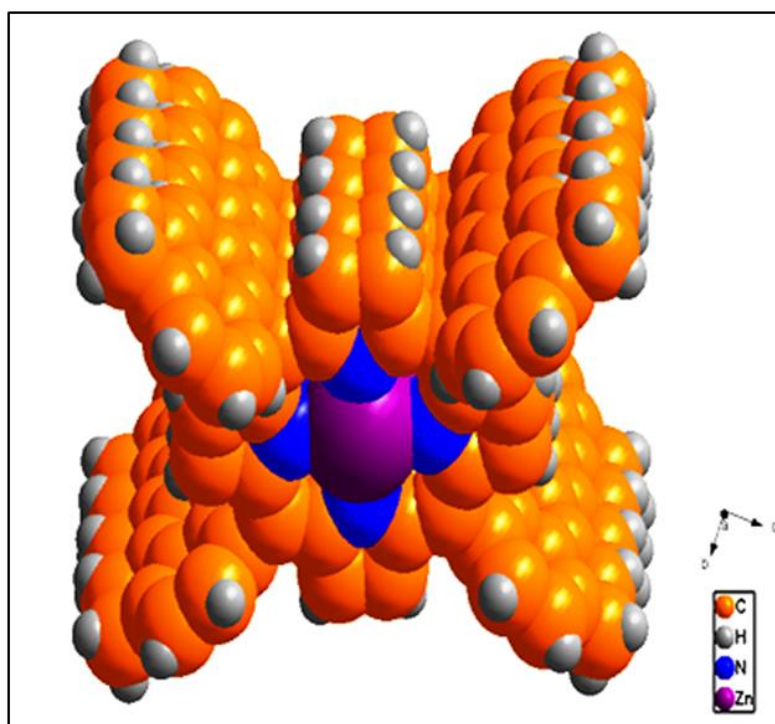


Figure 3.7. Orientation of zinc atoms in single-crystal X-ray structure of ZnTANP when viewed along *c*-axis.

Table 3.1. Crystallographic data for ZnTANP

Molecular formula	C ₃₄ H ₂₂ N ₂ Zn _{0.5}
Fw	491.22
Radiation	MoK α
Crystal symmetry	Triclinic
Space group	P -1
<i>a</i> (Å)	8.393(5)
<i>b</i> (Å)	11.628(5)
<i>c</i> (Å)	14.178(5)
<i>a</i> (deg)	90.808(5)
β (deg)	91.990(5)
γ (deg)	93.628(5)
<i>V</i> (Å ³)	1379.9(11)
<i>Z</i>	2
μ (mm ⁻¹)	0.489
<i>T</i> (K)	293(2) K
<i>D</i> _{calcd} (g cm ⁻³)	1.182
2 θ range (deg)	4.86 to 48.38
<i>e</i> data (<i>R</i> _{int})	4305 (0.0364)
<i>R</i> ₁ (<i>I</i> >2 σ (<i>I</i>))	0.0967
wR2	0.2467
GOF	1.098

3.3.4 Electronic Spectra

In order to confirm the charge-transfer (CT) complex formation, the UV-Vis-NIR spectroscopy was used to monitor the charge-transfer transitions between ZnTANP and C₆₀. Moderately weak absorption band in the visible region with maxima at around 860 nm in the C₆₀-ZnTANP hybrid material was observed (Figure 3.8).

This moderately weak band has been ascribed as charge transfer (CT) band from ZnTANP→C₆₀ and is well supported by previous reports.³⁹⁻⁴¹ The CT transition energy corresponding to the absorption band at around 860 nm is equivalent to 1.44 eV.

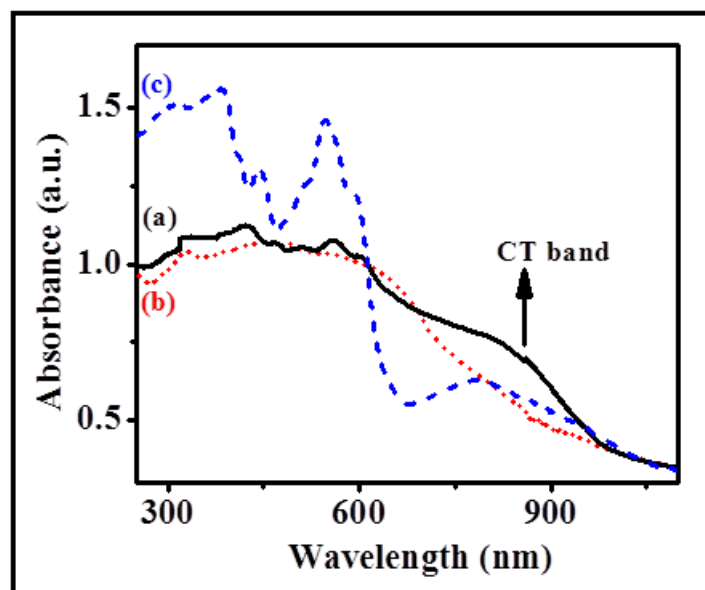


Figure 3.8. UV-Vis-NIR spectra of the (a) C_{60} -ZnTANP hybrid material (—), (b) C_{60} powder (⋯), and (c) ZnTANP powder (---).

3.3.5 X-Ray Photoelectron Spectroscopy (XPS)

XPS has been used to estimate the change in the distribution of electron density of hetero-atoms of the donors (ZnTANP) upon formation of hybrid material (C_{60} -ZnTANP). As all the four nitrogen atoms of ZnTANP are chemically equivalent, they give rise to a single peak in the N 1s region of the XP spectrum (Figure 3.9.I) and the binding energy of N atoms is 398.43 eV. Similarly there is only one Zn atom in the ZnTANP, which exhibits only one signal at the Zn 2P_{3/2} region of the XP spectrum (Figure 3.9.II). The binding energy of the coordinated Zn atom is 1021.32 eV. However in the XP spectrum of C_{60} -ZnTANP hybrid material a positive shift is observed for both N 1s (1.7 eV) and Zn 2P_{3/2} (0.3 eV) peaks and it clearly indicates the formation of a charge transfer based complex (Figures 3.9.I & 3.9.II).⁴²

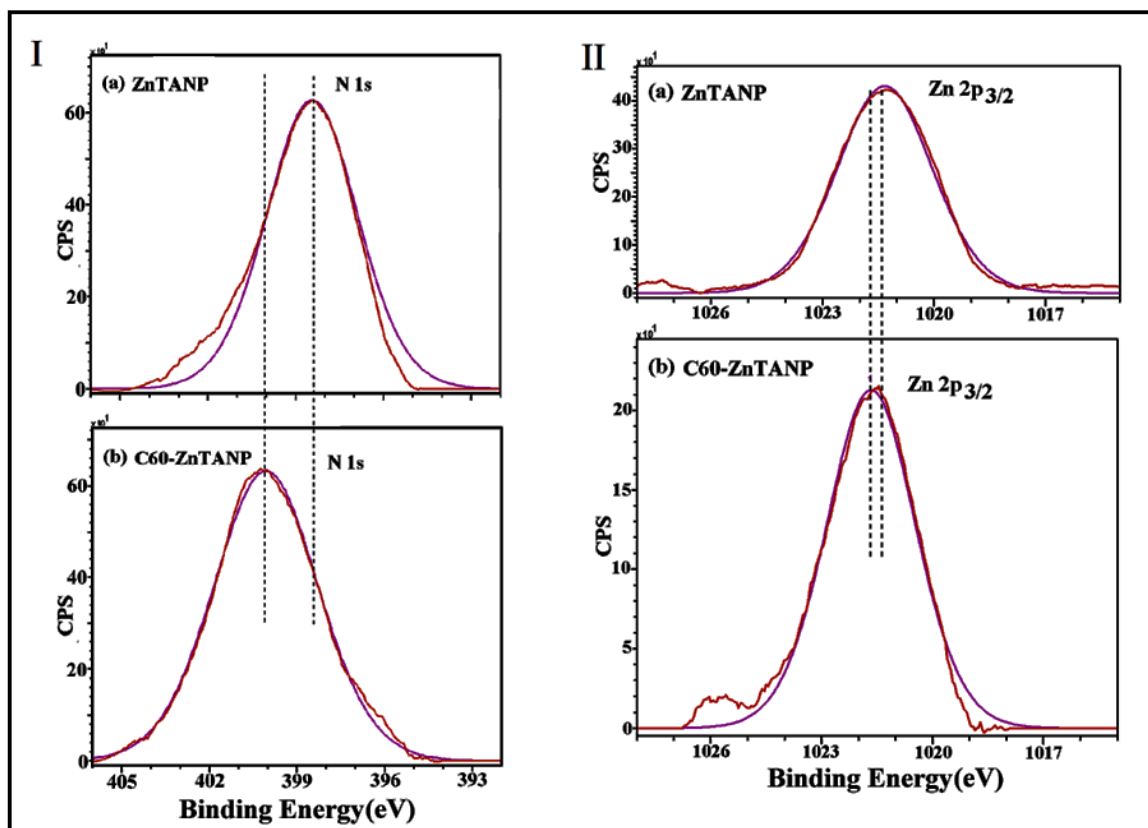


Figure 3.9.I. N1s region of the X-ray photo electron spectrum of (a) ZnTANP powder, and (b) C₆₀–ZnTANP hybrid materials. **Figure 3.9.II.** Zn2p_{3/2} region of the X-ray photo electron spectrum of (a) ZnTANP powder and (b) C₆₀–ZnTANP hybrid materials.

3.3.6 X-Ray Diffraction (XRD)

The C₆₀–ZnTANP circular discs were characterized by X-ray diffraction (XRD) measurements. XRD patterns of the ZnTANP, C₆₀-fullerene and C₆₀–ZnTANP circular discs are shown in Figure 3.10. The XRD pattern of the C₆₀–ZnTANP circular discs is entirely different from both the starting materials ZnTANP and C₆₀-fullerene. For C₆₀-fullerene, characteristic eight peaks are observed⁴³ and indexed as (111), (220), (311), (222), (331), (420), (422), and (511) / (333) and are typical of its fcc structure. C₆₀–ZnTANP circular discs exhibit few broad and few sharp and intense peaks. It appears that overlapping of C₆₀-fullerene and ZnTANP signals occurs and results in the broadening of the spectrum. However, the characteristic peaks of both C₆₀-fullerene and ZnTANP are present on the C₆₀–ZnTANP circular discs.

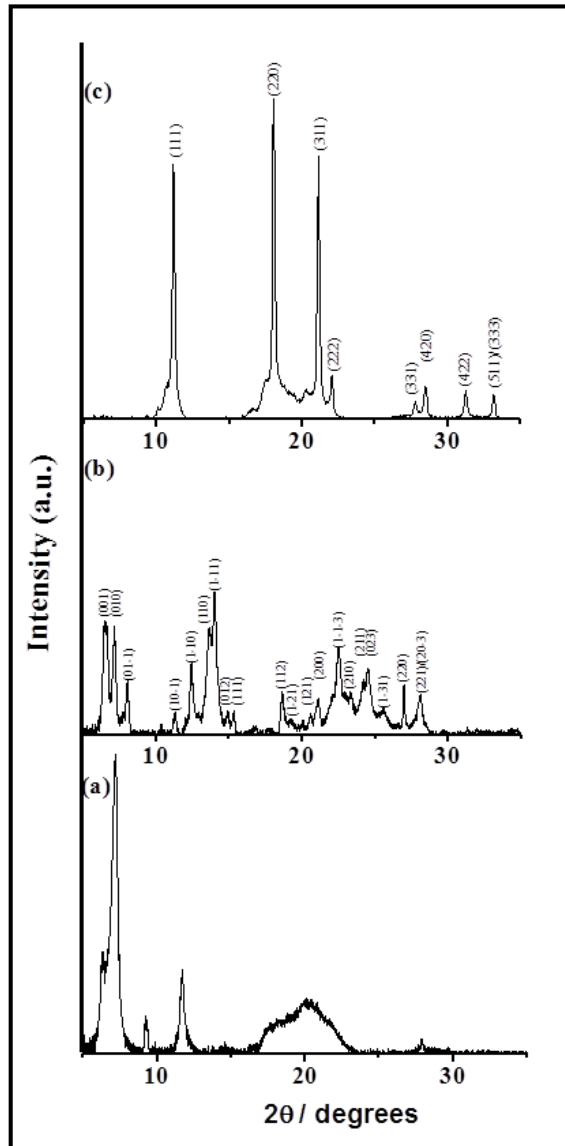


Figure 3.10. XRD patterns of the (a) C_{60} -ZnTANP circular discs, (b) ZnTANP powder and (c) C_{60} powder.

3.3.7 I - V Characteristics

In order to analyze the current-voltage (I - V) characteristics, two types of diodes have been fabricated with the following configurations (see the Experimental methods): (1) Ag/ C_{60} -ZnTANP circular discs/ p -Si/Ag and (2) pristine Si based heterojunction diode (Ag/ p -Si/Ag). A non-ideal rectifying current-voltage characteristics has been observed in both the cases in Figure 3.11.a.⁴⁴ The turn-on potential (V_T) and reverse break down voltage increases from 2.15 V to 3.15 V and 2.08 V to 8.17 V, respectively, for C_{60} -ZnTANP based diode in

comparison to pristine silicon based diode. The rectification ratio (r) of a diode is expressed by $r = I_f / I_r$, where I_f is the forward current, and I_r is the reverse current.⁴⁴ By using this equation, a rectification factor of 100 is obtained at 3 V. The composition of the first diode (*vide supra*), clearly points towards a MIS (metal, insulator layer, and semiconductor) diode.⁴⁴ By adding an insulating layer (native oxide layer on a Si substrate), the characteristics of the diode was found to change drastically. Upon applying a bias voltage, the interfacial state (it exists between the junction of SiO_x {native oxide layer} and C_{60} -ZnTANP circular discs) is getting charged and an additional field is generated.⁴⁴ Thermionic emission theory has been frequently used to explain the characteristics of the MIS diode.⁴⁴ The characteristics of such a diode can be easily approximated by the following I - V equation as: $I = I_0 \exp(qV/nk_B T)$ when $V > 3k_B T/q$, where q is the unit charge, V is the voltage (applied), k_B is Boltzmann constant, n is the ideality factor, and T is the temperature.^{44, 45} The following equation $\{n = [q/k_B T][dV/d(\ln I)]\}$ has been frequently used to calculate the ideality factor (n) of the diode.^{44, 45} The ideality factor (n) of the present diode has been found to be ~ 1.46 . The n value indicates that the present diode is not an ideal Schottky barrier diode; instead it is a MIS-type diode.⁴⁴ As both the charge trapping and charge recombination processes are absent in the ideal situation,⁴⁶ the ideality factor of the diode is thus equals to unity. The I - V curve of the present diode has two parts: (a) a linear region, and (b) an exponential region. The linear behaviour is predominantly observed up to the voltage of 1.4 V and the exponential behaviour is observed in the following region; $1.4 < V_f < 3.15\text{V}$. The exponential behavior, which is observed at the higher forward bias voltages ($1.4 < V_f < 3.15\text{V}$), is fully dictated by the diode characteristics, however the linear behavior, which is observed at the lower voltage sides ($V_o = 1.4\text{ V}$), is certainly not controlled by the diode characteristics fully and is dependent on certain other factors.⁴⁷ Information regarding the recombination processes and the shape of the interfaces (i.e. internal bulk morphology) are obtained from the ideality

factor (n). Ideality factor (n), and the reverse saturation current (I_0) controls the I - V characteristics of a device in the exponential region.⁴⁵ In fact, the Ag/C₆₀-ZnTANP/SiO_x/ p -Si/Ag structure has four interfaces: (i) Ag-C₆₀-ZnTANP, (ii) C₆₀-ZnTANP-SiO_x, (iii) SiO_x- p -Si, and (iv) p -Si-Ag. The electrical properties of heterostructure (Ag/C₆₀-ZnTANP/SiO_x/ p -Si/Ag) diodes are solely dependent on the interface. Thus it is highly possible that the presence of SiO_x- p -Si and p -Si-Ag interfaces can also influence the diode characteristics. To rule out that possibility, we have constructed a device; Ag/SiO_x/ p -Si/Ag, and checked its I - V characteristics. The obtained symmetric I - V characteristic clearly ruled out the involvement

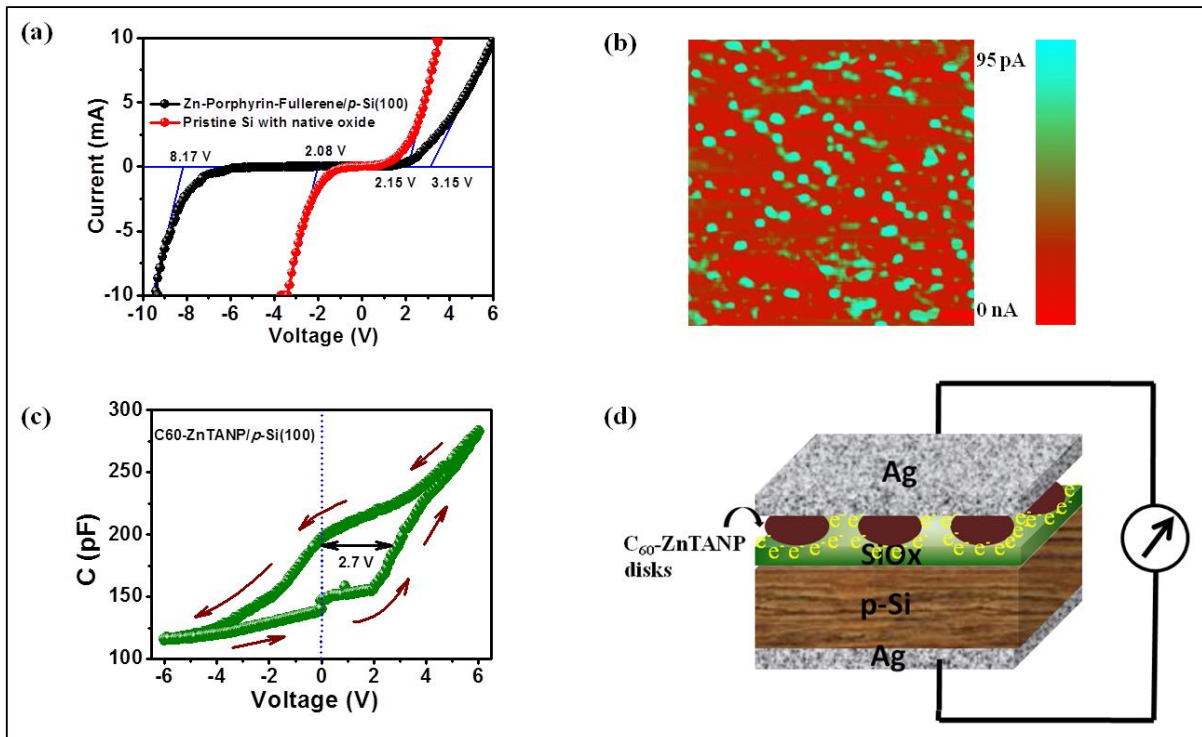


Figure 3.11. (a) Nonlinear I - V characteristics of Ag/C₆₀-ZnTANP circular discs/ p -Si/Ag diodes. The black solid line represents the I - V characteristics of Ag/C₆₀-ZnTANP circular discs/ p -Si/Ag diodes and the red line are for the Ag/ p -Si/Ag diodes. (b) CAFM micrographs (2 μ m \times 2 μ m) of C₆₀-ZnTANP circular discs deposited on Si. (c) A voltage dependent capacitance of Ag/C₆₀-ZnTANP circular discs/ p -Si/Ag hetero structure diode. (d) Charge transport across the potential barriers is shown schematically for the hetero-structure diode Ag/C₆₀-ZnTANP circular discs/ p -Si/Ag.

of SiO_x- p -Si and p -Si-Ag interfaces. This clearly indicates that the electrical characteristic of the Ag/C₆₀-ZnTANP/SiO_x/ p -Si/Ag diode is largely controlled by Ag-C₆₀-ZnTANP and C₆₀-

ZnTANP-SiO_x interfaces. Thus the depletion region in the C₆₀-ZnTANP circular discs/SiO_x/Si interface controls the exponential region of the *I-V* characteristics in the device. To garner further support and to understand the current conduction pathways in the device, CAFM measurements were carried out. Stable images were obtained after scanning the different regions of the device with repeating cycles and it was confirmed that the C₆₀-ZnTANP circular discs are bound strongly at the device surface. CAFM current maps at 10 V bias show bright spots with ~100 pA intensity (Figure 3.11.b). These observed bright spots in Figure 3.11.b are assigned as leakage current and are responsible for the conduction properties in the device.

3.3.8 *C-V* Characteristics

The critical role of the interface is clearly understood from the *I-V* characteristic of the present device and this phenomenon has tempted us to measure the charge storage capability of our device. The corresponding *C-V* curves have been obtained by sweeping a voltage from inversion to accumulation regions of the C₆₀-ZnTANP circular disc containing layer on Si surface (Figure 3.11.c) at room temperature.

In general, hysteresis behavior in the capacitance-voltage plot gives a first-hand idea about the suitability of a device in charge storage applications.⁴⁸ Thus, here, the observed counter-clock wise hysteresis is a clear signature of the charge-trapping phenomena and a positive shift in voltage (~2.7 V) indicates that those trapped charges are electrons only.⁴⁸ It's worth mentioning here that in the Ag/SiO₂/Si junction, there no such hysteresis window is observed and it clearly indicates that charge trapping phenomena is nowhere involved in the SiO₂ and Si interface. Carrier injection model has been successfully employed to explain this kind of hysteresis curve and it is further inferred that the polarity of the bias voltage is fully responsible for the injection of electrons and holes.⁴⁸ Thus it can be concluded that the trapped electrons residing in the sandwiched C₆₀-ZnTANP circular discs or at the interface of

the C₆₀-ZnTANP circular discs/SiO_x are responsible for this hysteresis phenomena. It is obvious that because of the very low thickness (~2 nm) of the native oxide layer, the other alternatives, like SiO_x/Si interface, or the oxide layers are clearly ruled out from the perspectives of charge storage capabilities. Thus it is evident that the trapped charges can reside only at the C₆₀-ZnTANP circular discs/SiO_x interface. A schematic description of the device is shown in Figure 3.11.d.

Thus in the forward cycle electrons are trapped at the interface and in the reverse cycle they are neutralized by holes. These trapped electrons at the interface generate an additional electric field and thus helps to reduce the barrier height from 2.7 to 0.97 eV. As a result of this, the lowering of turn-on potential occurred. Thus the occurrence of hysteresis could be attributed due to the influence of C₆₀-ZnTANP circular discs/SiO_x interfacial state. It has been assumed that the charge transfer across the circular discs occurred *via* tunnelling mechanisms. The amount of charge density trapped in the C₆₀-ZnTANP circular discs/SiO_x interface can be easily estimated with the help of following equation: $N_t = \epsilon_0 K \Delta V_{FB} / et$ where, ϵ_0 is the permittivity of free space, K is the dielectric constant of C₆₀ (~4.5), ΔV_{FB} is the shifting of flat-band voltage, e is the electronic charge, and t is the thickness of silica layer.⁴⁸ The rough amount of charge density stored in the C₆₀-ZnTANP circular discs/SiO_x interface is estimated to be $2.24 \times 10^{12} \text{ cm}^{-2}$.

3.4 Conclusions

In conclusion, a donor (D)-acceptor (A) based hybrid material having 1:1 composition of C₆₀-ZnTANP was synthesized by using a simple protocol. Circular disc-like 3D objects with an average size distribution of 250 nm were generated by using drop-casting method. By using these circular disc-like nano-architectures, a MIS-type diode was fabricated with the following composition: Ag/C₆₀-ZnTANP circular discs/p-Si/Ag. The *I-V* characteristic of the device was measured and it shows a non-ideal rectifying behaviour. *C-V* measurements were

also performed to analyze the charge storage properties of these circular discs. The observed counter-clock wise hysteresis in the C - V measurement is a clear signature of the charge-trapping phenomena and a positive shift in voltage (~ 2.7 V) indicates that those trapped charges are electrons only. The rough amount of charge density stored in the C_{60} -ZnTANP circular discs/ SiO_x interface is estimated to be 2.24×10^{12} cm^{-2} . CAFM current maps at 10 V bias show bright spots with ~ 100 pA intensity. These bright spots are attributed as leakage current and are responsible for the conduction properties in the device. However, as the p -Si substrate is not fully covered by the nanodiscs, thus the possibility of other conduction pathways (Ag/ p -Si/Ag) in the device also cannot be ruled out completely (*vide supra*). Thus our results reveal that the circular disc-like nano-architectures made from C_{60} -ZnTANP hybrid materials strongly influence the diode characteristics but its true nature cannot be ascertained accurately.

3.5 Experimental Section

3.5.1 Materials

The precursors pyrrole, benzonitrile, DDQ (2,3-dichloro-5,6-dicyano-1,4-benzoquinone), 5-acenapthene carboxaldehyde, C_{60} , Toluene and TEAP (tetraethyl ammonium perchlorate) were purchased from Aldrich, USA. $Zn(OAc)_2$, $2H_2O$ and isopropyl alcohol were purchased from Merck, India. Other chemicals were of reagent grade. Hexane and CH_2Cl_2 were distilled from KOH and CaH_2 , respectively. For spectroscopy and electrochemical studies HPLC grade solvents were used. 5,10,15,20-tetrakis(1,2-dihydro-5-acenaphthylenyl) porphyrin, H_2TANP was prepared by slight modification of an earlier reported synthetic protocol (see results and discussion).⁴⁹

3.5.2 Characterization

UV-Vis spectral studies were performed on a Perkin-Elmer LAMBDA-750 spectrophotometer. Emission spectral studies were performed on a Perkin Elmer, LS 55

spectrophotometer using optical cell of 1 cm path length. The fluorescence quantum yields were determined using tetraphenylporphyrin, [TPP] as a reference. Time resolved fluorescence measurements were carried out using a time-correlated single photon counting (TCSPC) spectrometer (Edinburgh, OB 920). The elemental analyses were carried out with a Perkin-Elmer 240C elemental analyzer. The NMR measurements were carried out using a Bruker AVANCE 400 NMR spectrometer. Chemical shifts are expressed in parts per million (ppm) relative to residual chloroform ($\delta = 7.26$). Fourier transformed infrared (FTIR) spectra were recorded on a Perkin-Elmer spectrophotometer with samples prepared as KBr pellets. Electrospray mass spectra were recorded on a Bruker Micro TOF-QII mass spectrometer. Cyclic voltammetry measurements were carried out using a CH Instruments model CHI1120A electrochemistry system. A glassy-carbon working electrode, a platinum wire as an auxiliary electrode and a saturated calomel reference electrode (SCE) were used in a three-electrode configuration. Tetraethyl ammonium perchlorate (TEAP) was the supporting electrolyte (0.1M) and the concentration of the solution was 10^{-3} M with respect to the complex. The oxidation and reduction processes at the positive and negative side of the SCE reference electrode were measured by using a glassy-carbon working electrode. The half wave potential E_{298}^0 was set equal to $0.5(E_{pa} + E_{pc})$, where E_{pa} and E_{pc} are anodic and cathodic cyclic voltammetric peak potentials, respectively. The scan rate used was 100 mVs^{-1} . For the fabrication of Ag/C₆₀-ZnTANP circular discs/p-Si/Ag diode, p-type Si was used as a substrates. The substrates were cleaned sequentially by de-ionized water, methanol, and finally with acetone by using an ultrasonic bath with average immersion time of 10–15 min. For electrical measurements, p-Si (100) (thickness = 500 μm) with native oxide (SiO_x) layer of about 2 nm thickness were used as a substrate and as a bottom electrode. On this SiO_x, desired order of C₆₀-ZnTANP was drop-casted and a silver paste was used to make electrical contacts on the top of C₆₀-ZnTANP films and on the back side of the Si substrates. In this

way a hybrid structure was fabricated. The formation of Ag/C₆₀–ZnTANP/Si/Ag hetero-structure diodes was verified by measuring *I-V* characteristics with a source meter (Keithley, 2410). The charge storage properties of this hetero-structure diode were investigated by performing capacitance-voltage (*C-V*) measurements at a frequency of 1 MHz by using HP 4284A precision LCR meter. All the measurements were carried out on several sets of samples to ensure the repeatability and reproducibility of the data. Conducting atomic force microscopy (CAFM) was used to measure the local electrical property of the samples. CAFM was carried out by *ex-situ* AFM (Asylum Research, MFP3D) in the contact mode with a Pt coated Si cantilever (from NT-MDT) having a radius of curvature of ~35 nm. For each sample, several images were taken from different regions to check the uniformity and to estimate the average conduction areas. Powder X-ray diffraction (XRD) patterns of the samples were recorded on a Bruker DAVINCI D8 ADVANCE diffractometer equipped with Cu-K α radiation source with $\lambda = 0.15406$ nm. XPS measurements of the sample were performed by using a monochromatic Mg K α X-ray source (XPS VG Microtech). SEM images of the nanoparticles were captured by using a field emission gun scanning electron microscope (FEGSEM) system (Zeiss, Germany make, Supra 55).

3.5.3 Crystal Structure Determination

Single crystals of ZnTANP were grown by slow diffusion of a solution of the metal complexes in diethyl ether into dichloromethane, followed by slow evaporation under atmospheric conditions. The crystal data of ZnTANP were collected on a Bruker Kappa APEX II CCD diffractometer at 293 K. Selected data collection parameters and other crystallographic results are summarized in Table 3.1. All data were corrected for Lorentz polarization and absorption effects. The program package SHELXTL⁵⁰ was used for structure solution and full matrix least squares refinement on F^2 . Hydrogen atoms were included in the refinement using the riding model. Contributions of H atoms for the water molecules were

included but were not fixed. Disordered solvent molecules were taken out using SQUEEZE⁵¹ command in PLATON.

3.5.4 Preparation of C₆₀–ZnTANP Hybrid Material

The C₆₀–ZnTANP hybrid material was synthesized by following a standard protocol developed by Wakahara *et al.*²⁹ In a standard protocol, a 10 mL C₆₀ saturated toluene solution was prepared as a stock solution in a 10 mL volumetric flask. Aliquot of 4 mL was taken from this solution and was mixed with 8.5 mg of ZnTANP in a glass bottle. The solution mixture was then stirred well at room temperature by using ultrasonication. The resulting mixture was kept at a refrigerator (4°C) for 1 h. 8 mL of isopropyl alcohol was added slowly to this mixture; the combined solution was shaken vigorously and was kept in fridge again for overnight. The resulted precipitate was collected, washed thoroughly with toluene, and dried in a vacuum.

References

1. Yamaoka, H., *JETI*, **2011**, *59*, 37-42.
2. Camaioni, N.; Garlaschelli, L.; Geri, A.; Maggini, M.; Possamai, G.; Ridolfi, G., *J.Mater.Chem.*, **2002**, *12*, 2065-2070.
3. Irimia-Vladu, M.; Marjanovic, N.; Vlad, A.; Ramil, A. M.; Hernandez-Sosa, G.; Schwoödiauer, R.; Bauer, S.; Sariciftci, N. S., *Adv.Mater. (Weinheim, Ger.)*, **2008**, *20*, 3887-3892.
4. Riccò, M.; Bisbiglia, M.; De Renzi, R.; Bolzoni, F., *Solid State Commun.*, **1997**, *101*, 413-416.
5. Bosi, S.; Da Ros, T.; Spalluto, G.; Prato, M., *Eur. J. Med. Chem.*, **2003**, *38*, 913-923.
6. Nakanishi, T.; Schmitt, W.; Michinobu, T.; Kurth, D. G.; Ariga, K., *Chem. Commun.(Cambridge, U. K.)*, **2005**, 5982-5984.
7. Nakanishi, T.; Ariga, K.; Michinobu, T.; Yoshida, K.; Takahashi, H.; Teranishi, T.; Möhwald, H.; G. Kurth, D., *Small*, **2007**, *3*, 2019-2023.
8. Nakanishi, T.; Michinobu, T.; Yoshida, K.; Shirahata, N.; Ariga, K.; Möhwald, H.; Kurth, D. G., *Adv. Mater.(Weinheim, Ger.)*, **2008**, *20*, 443-446.
9. Wang, J.; Shen, Y.; Kessel, S.; Fernandes, P.; Yoshida, K.; Yagai, S.; Kurth, D. G.; Möhwald, H.; Nakanishi, T., *Angew.Chem.,Int.Ed.*, **2009**, *48*, 2166-2170.
10. Nakanishi, T.; Miyashita, N.; Michinobu, T.; Wakayama, Y.; Tsuruoka, T.; Ariga, K.; Kurth, D. G., *J.Am.Chem.Soc.*, **2006**, *128*, 6328-6329.
11. Shimidzu, T.; Segawa, H.; Wu, F.; Nakayama, N., *J. Photochem. Photobiol., A*, **1995**, *92*, 121-127.
12. Schwab, A. D.; Smith, D. E.; Bond-Watts, B.; Johnston, D. E.; Hone, J.; Johnson, A. T.; de Paula, J. C.; Smith, W. F., *Nano Lett.*, **2004**, *4*, 1261-1265.
13. Giguere, J.-B.; Morin, J.-F., *Org. Biomol. Chem.*, **2012**, *10*, 1047-1051.

14. V. Konarev, D.; N. Lyubovskaya, R., *Russ.Chem. Rev.*, **1999**, 68, 19-38.
15. Moriyama, H.; Kobayashi, H.; Kobayashi, A.; Watanabe, T., *Chem. Phys. Lett.*, **1995**, 238, 116-121.
16. Stephens, P. W.; Cox, D.; Lauher, J. W.; Mihaly, L.; Wiley, J. B.; Allemand, P.-M.; Hirsch, A.; Holczer, K.; Li, Q.; Thompson, J. D.; Wudl, F., *Nature (London)*, **1992**, 355, 331-332.
17. Kveder, V. V.; Steinman, E. A.; Narymbetov, B. Z.; Khasanov, S. S.; Rozenberg, L. P.; Shibaeva, R. P.; Bazhenov, A. V.; Gorbunov, A. V.; Maksimuk, M. Y.; Konarev, D. V.; Lyubovskaya, R. N.; Ossipyan, Y. A., *Chem.Phys.*, **1997**, 216, 407-415.
18. Kajzar, F.; Okada-Shudo, Y.; Meritt, C.; Kafafi, Z., *Synth. Met.*, **1998**, 94, 91-98.
19. Campoy-Quiles, M.; Ferenczi, T.; Agostinelli, T.; Etchegoin, P. G.; Kim, Y.; Anthopoulos, T. D.; Stavrinou, P. N.; Bradley, D. D. C.; Nelson, J., *Nat. Mater.*, **2008**, 7, 158-164.
20. Hoppe, H.; Sariciftci, N. S., *J. Mater. Chem.*, **2006**, 16, 45-61.
21. Peet, J.; Senatore, M. L.; Heeger, A. J.; Bazan, G. C., *Adv. Mater. (Weinheim, Ger.)*, **2009**, 21, 1521-1527.
22. Zhang, X.; Takeuchi, M., *Angew. Chem. ,Int. Ed., Engl*, **2009**, 48, 9646-9651.
23. Boyd, P. D. W.; Reed, C. A., *Acc. Chem. Res*, **2005**, 38, 235-242.
24. Tashiro, K.; Aida, T., *Chem. Soc. Rev.*, **2007**, 36, 189-197.
25. Sgobba, V.; Giancane, G.; Conoci, S.; Casilli, S.; Ricciardi, G.; Guldi, D. M.; Prato, M.; Valli, L., *J. Am. Chem. Soc.*, **2007**, 129, 3148-3156.
26. Georgakilas, V.; Pellarini, F.; Prato, M.; Guldi, D. M.; Melle-Franco, M.; Zerbetto, F., *Proc. Natl. Acad. Sci. U. S. A.*, **2002**, 99, 5075-5080.
27. Yamaguchi, T.; Ishii, N.; Tashiro, K.; Aida, T., *J. Am. Chem. Soc.*, **2003**, 125, 13934-13935.

28. Yoshimoto, S.; Tsutsumi, E.; Honda, Y.; Murata, Y.; Murata, M.; Komatsu, K.; Ito, O.; Itaya, K., *Angew. Chem., Int. Ed.*, **2004**, *43*, 3044-3047.
29. Wakahara, T.; D'Angelo, P.; Miyazawa, K. i.; Nemoto, Y.; Ito, O.; Tanigaki, N.; Bradley, D. D. C.; Anthopoulos, T. D., *J. Am. Chem. Soc.*, **2012**, *134*, 7204-7206.
30. Hasobe, T.; Imahori, H.; Fukuzumi, S.; Kamat, P. V., *J. Phys. Chem. B*, **2003**, *107*, 12105-12112.
31. Nishino, T.; Ito, T.; Umezawa, Y., *Proc. Natl. Acad. Sci. U. S. A.*, **2005**, *102*, 5659-5662.
32. Metzger, R. M.; Baldwin, J. W.; Shumate, W. J.; Peterson, I. R.; Mani, P.; Mankey, G. J.; Morris, T.; Szulczewski, G.; Bosi, S.; Prato, M.; Comito, A.; Rubin, Y., *J. Phys. Chem. B*, **2003**, *107*, 1021-1027.
33. Koiry, S. P.; Jha, P.; Aswal, D. K.; Nayak, S. K.; Majumdar, C.; Chattopadhyay, S.; Gupta, S. K.; Yakhmi, J. V., *Chem. Phys. Lett.*, **2010**, *485*, 137-141.
34. Rahaman, S.; Maikap, S.; Tien, T.-C.; Lee, H.-Y.; Chen, W.-S.; Chen, F.; Kao, M.-J.; Tsai, M.-J., *Nanoscale Res. Lett.*, **2012**, *7*, 345.
35. Sinha, W.; Deibel, N.; Agarwala, H.; Garai, A.; Schweinfurth, D.; Purohit, C. S.; Lahiri, G. K.; Sarkar, B.; Kar, S., *Inorg. Chem.*, **2014**, *53*, 1417-1429.
36. Sinha, W.; Deibel, N.; Garai, A.; Schweinfurth, D.; Anwar, S.; Purohit, C. S.; Sarkar, B.; Kar, S., *Dyes and Pigments*, **2014**, *107*, 29-37.
37. Sinha, W.; Kumar, M.; Garai, A.; Purohit, C. S.; Som, T.; Kar, S., *Dalton Trans.*, **2014**, *43*, 12564-12573.
38. Sinha, W.; Sommer, M. G.; Deibel, N.; Ehret, F.; Sarkar, B.; Kar, S., *Chem. -Eur. J.*, **2014**, *20*, 15920-15932.

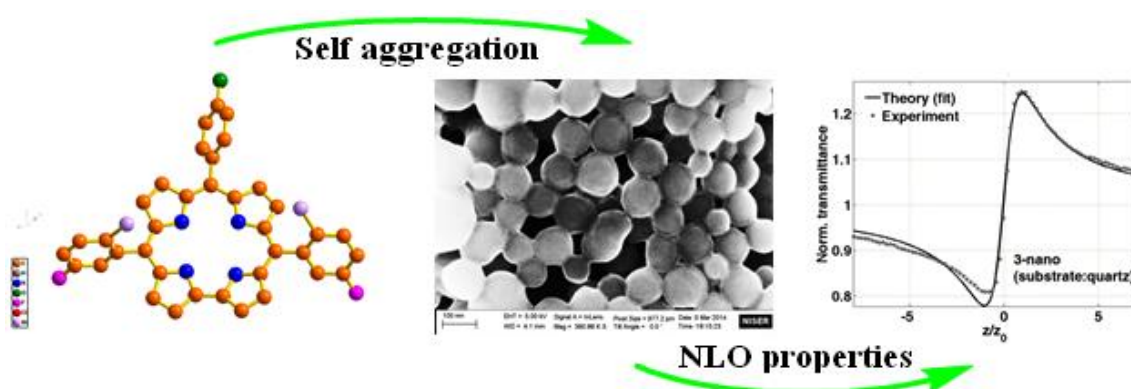
39. Konarev, D. V.; Kovalevsky, A. Y.; Li, X.; Neretin, I. S.; Litvinov, A. L.; Drichko, N. y. V.; Slovokhotov, Y. L.; Coppens, P.; Lyubovskaya, R. N., *Inorg. Chem.*, **2002**, *41*, 3638-3646.
40. Imahori, H.; Tkachenko, N. V.; Vehmanen, V.; Tamaki, K.; Lemmetyinen, H.; Sakata, Y.; Fukuzumi, S., *J. Phys. Chem. A*, **2001**, *105*, 1750-1756.
41. Tkachenko, N. V.; Guenther, C.; Imahori, H.; Tamaki, K.; Sakata, Y.; Fukuzumi, S.; Lemmetyinen, H., *Chem. Phys. Lett.*, **2000**, *326*, 344-350.
42. Kretschmann, A.; Walz, M.-M.; Flechtner, K.; Steinruck, H.-P.; Gottfried, J. M., *Chem. Commun. (Cambridge, U. K.)*, **2007**, 568-570.
43. Wang, L.; Liu, B.; Liu, D.; Yao, M.; Hou, Y.; Yu, S.; Cui, T.; Li, D.; Zou, G.; Iwasiewicz, A.; Sundqvist, B., *Adv. Mater. (Weinheim, Ger.)*, **2006**, *18*, 1883-1888.
44. Sze, S. M.; Ng, K. K., *Physics of Semiconductor Devices*. Wiley 2006.
45. Kumar, M.; Kanjilal, A.; Som, T., *AIP Adv.*, **2013**, *3*, 092126.
46. Farag, A. A. M.; El-Shazly, E. A. A.; Abdel Rafea, M.; Ibrahim, A., *Sol. Energy Mater. Sol. Cells*, **2009**, *93*, 1853-1859.
47. Gedikpınar, M.; Çavaş, M.; Alahmed, Z. A.; Yakuphanoglu, F., *Superlattices Microstruct.*, **2013**, *59*, 123-132.
48. Patil, S.; Datar, S.; Rekha, N.; Asha, S. K.; Dharmadhikari, C. V., *Nanoscale*, **2013**, *5*, 4404-4411.
49. Zhilina, Z. I.; Vodzinskii, S. V.; Andronati, S. A., *Ukr. Khim. Zh. (Russ. Ed.)*, **1990**, *56*, 1084-1088.
50. Sheldrick, G., *Acta Crystallogr., Sect. A*, **2008**, *64*, 112-122.
51. Van, d. S. P.; Spek, A. L., *Acta Crystallogr., Sect. A*, **1990**, *A46*, 194-201.

CHAPTER 4

A Comparative Study of Optical Nonlinearities of *trans*-**A₂B**-Corroles in Solution and in Aggregated State

- 4.1 Abstract
- 4.2 Introduction
- 4.3 Results and Discussion
 - 4.3.1 Synthesis and Characterization
 - 4.3.2 Structures
 - 4.3.3 Electronic Spectra
 - 4.3.4 Emission Spectra
 - 4.3.5 Self aggregates of **1-3**
 - 4.3.6 Measurements of NLO properties
 - 4.3.7 Theoretical model for analyzing NLO responses
 - 4.3.8 Results
- 4.4 Conclusions
- 4.5 Experimental Section
 - 4.5.1 Materials
 - 4.5.2 Physical Measurements
 - 4.5.3 Crystal Structure Determination
 - 4.5.4 NLO measurement

4.1 Abstract



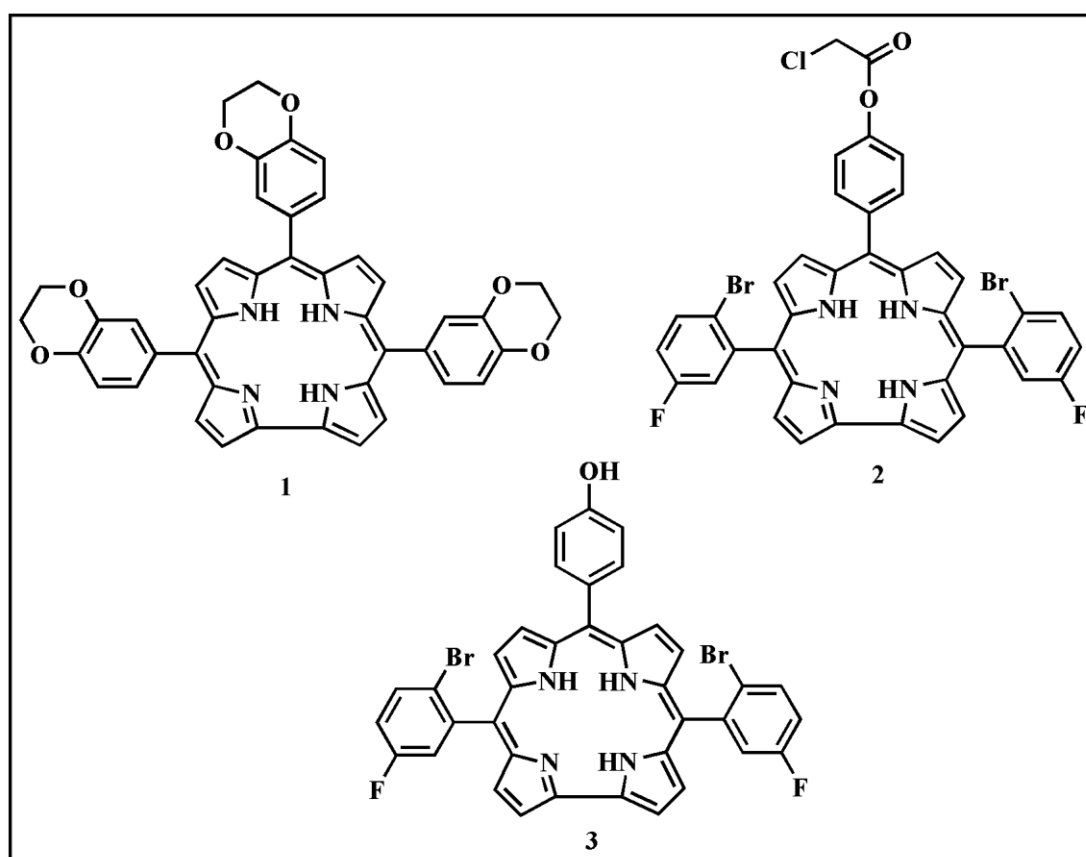
A series of novel A_3 -corrole and $trans$ - A_2B -corroles have been synthesized with the aim of developing organic materials with improved nonlinear optical (NLO) properties. All three newly synthesized corroles have been characterized by various spectroscopic techniques including single crystal X-ray structural analysis of the representative one. The crystal structure analysis of 10-(4-hydroxyphenyl)-5,15-bis(2-bromo-5-fluorophenyl) corrole shows several $O-H\cdots N$ interactions. The self-aggregates of all three corroles were prepared on a silicon wafer as well as on a quartz substrate by using a drop-casting method in a dichloromethane and methanol (1:2) solvent mixture. In all three free base corroles, well defined and nicely organized three-dimensional objects with diameter of ca. 320 nm (nano hollow-spheres), 450 nm (nanobulbs), and 120 nm (nanodiscs) were obtained. The NLO properties (nonlinear refractive index, n_2 and two-photon absorption coefficient, β) of all of the corrole derivatives in toluene solution and in aggregated form were measured by the Z-scan technique. The nonlinear refractive indices, n_2 of the free base corroles (in toluene solution) were found out to be $-16.8 \times 10^{-18} \text{ m}^2/\text{W}$, $-7.8 \times 10^{-18} \text{ m}^2/\text{W}$ and $-25.9 \times 10^{-18} \text{ m}^2/\text{W}$ respectively and for the corresponding aggregates (nanoparticles of the free base corroles), it was found out to be $-1.1 \times 10^{-15} \text{ m}^2/\text{W}$, $-1.9 \times 10^{-15} \text{ m}^2/\text{W}$, and $71.8 \times 10^{-15} \text{ m}^2/\text{W}$ respectively. Similarly, the two-photon absorption coefficient, β of all the synthesized free base corroles

(in toluene solution) were found out to be 5.7×10^{-15} m/W, 1.9×10^{-15} m/W and 17.2×10^{-15} m/W respectively and for the corresponding aggregates (nanoparticles), the values were 4.0×10^{-13} m/W, 2.0×10^{-13} m/W, and 444.0×10^{-13} m/W respectively. These NLO properties of the free base corrole derivatives (in solution and in aggregates) have been explored with a specific aim to identify the possibility of their applications in ultrafast switching devices for use in high-speed fiber-optic communications and photonic integrated circuits.

4.2 Introduction

Molecules with large nonlinear optical (NLO) coefficients have found extensive applications in a wide-range of optoelectronic devices and in fiber-optic communication systems in the form of switches and routers.¹⁻⁶ The NLO properties of various organic molecules in terms of nonlinear refractive index (n_2), nonlinear or two-photon absorption (β), electro-optic and thermo-optic manifestations, dispersion properties *etc.* are being widely investigated in order to achieve rapid and error-free switching and routing.⁷⁻⁹ Among the organic NLO materials, π -conjugated organic molecules such as porphyrin based materials are in the fore front due to very large polarizable electron density and therefore, exhibit non-resonant and ultrafast NLO responses.¹⁰⁻¹⁴ The NLO properties of a large number of porphyrin based macrocycles, such as, porphyrins, phthalocyanines, and π -extended porphyrins have been widely investigated.¹⁰⁻¹³ Among these porphyrin based macro-cycles, corrole based materials have been rarely explored.^{15,16} When compared to analogous porphyrins, corroles are contracted version with one methine carbon less.¹⁷ This structural change imparts smaller cavity size of corrole compared to analogous porphyrin derivatives.¹⁷ Previous literature reports suggest that corrole has highly conjugated π -electron density and it shows different photophysical properties compared to its porphyrin counterpart.¹⁸⁻²⁰ Due to the clear superiority than its porphyrin analogues and also the discovery of a facile synthetic methodology of corrole synthesis generated a tremendous interest in the development of novel corrole based materials for various applications.²¹⁻²³ Only a few literature reports show the interesting NLO properties of corrole based systems. Rebane *et al.*¹⁵ has observed for the first time that compared to porphyrin, corrole shows larger two-photon cross sections due to lack of inversion center. Rao *et al.*¹⁶ has demonstrated the third-order NLO properties for two free base corrole derivatives and their corresponding germanium and phosphorous complexes. To the best of our knowledge, all the existing literature reports are related to the measurement of

NLO properties of A_3 -corroles only, however no studies have yet been done regarding the measurements of relatively more complicated *trans*- A_2B -corrole systems. Although the NLO properties of corroles are more promising than its porphyrin analogues, there have been very few attempts made to obtain a comparative account on NLO properties of corroles in aggregated state in addition to its solution phase NLO properties. The present work describes the synthesis of one novel A_3 -corrole and two novel *trans*- A_2B -corroles namely, 5,10,15-tris [3,4-(1,4-dioxan)phenyl]corrole, **1**, 10-[4-(chloroacetoxy)phenyl]-5,15-bis(2-bromo-5-fluoro phenyl)corrole, **2**, and 10-(4-hydroxyphenyl)-5,15-bis(2-bromo-5-fluorophenyl)corrole, **3** (Scheme 4.1). Various oxygenated functional groups are incorporated in the peripheral phenyl rings of the free base corrole derivatives, keeping in mind that these substituents



Scheme 4.1. Structure of the FB corroles **1-3**.

might influence the formation of different sized and shaped self-assembled aggregates. Use of self-assembled porphyrins/corroles based systems in the design of improved NLO

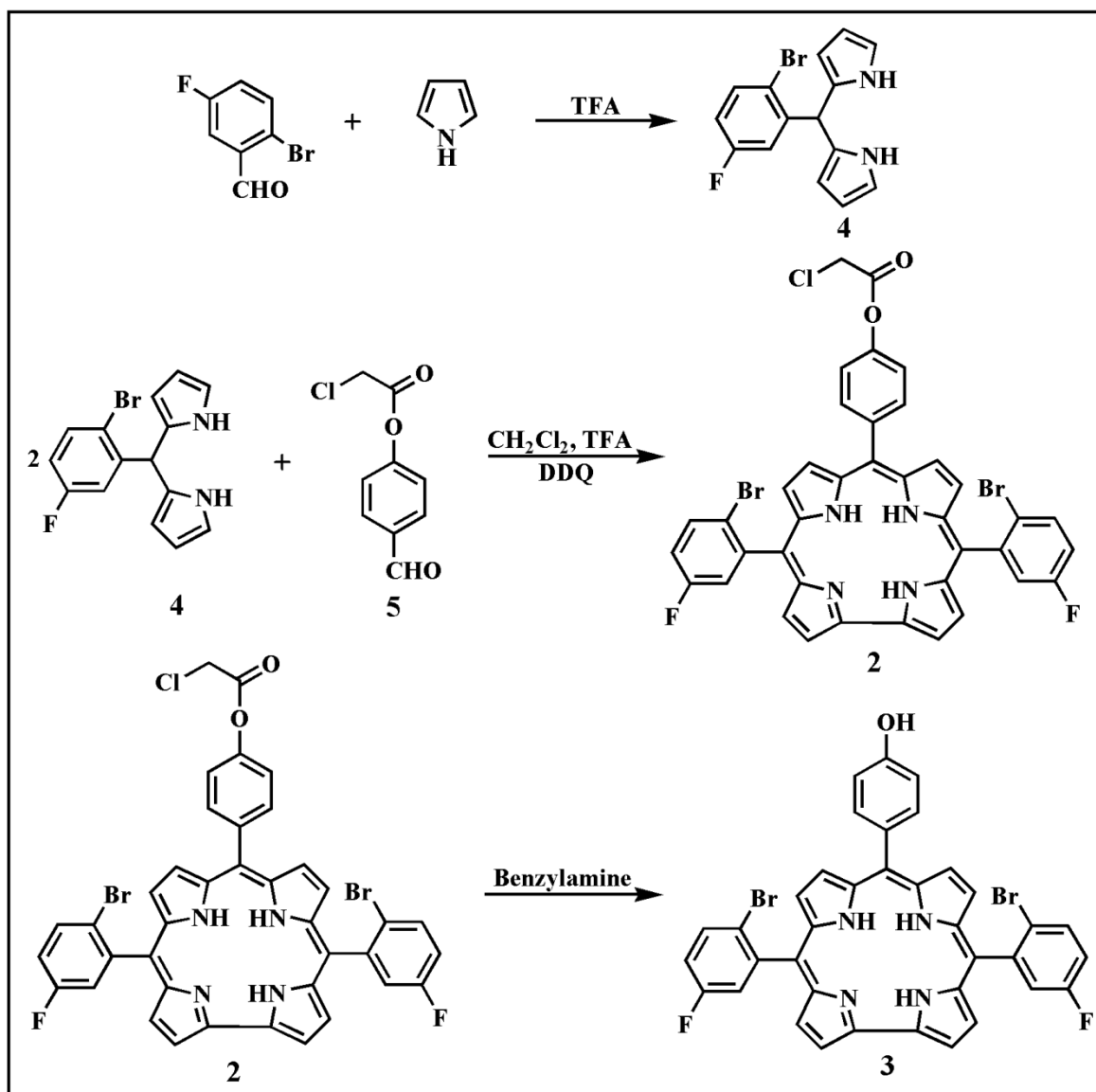
materials are borne out from the fact that there exists an induced electronic interaction among the adjacent porphyrins/corroles molecules. Theoretical calculations have also predicted the enhanced values of NLO responses upon self-aggregation.⁶ Third order NLO responses are found to increase markedly as the electron density in the macrocycle adds on. Thus electron releasing groups at the peripheral phenyl rings of the macrocycles would be a better choice for the same. Thus a series of electron donating substituents (1, 4-dioxan, 4-chloroacetoxy, and hydroxy) at the *para*-position of the phenyl rings are introduced.¹¹

In addition to the synthesis and spectral characterization of **1-3**, the crystal structures of **3**, and NLO properties of **1-3** in solution state are also reported here. The present work also describes the synthesis of the aggregates of all the three FB (free base) corroles. In addition to the synthesis and characterization of the aggregates, the NLO properties of the aggregates are also studied and compared with the measurements in solution state.

4.3 Results and Discussion

4.3.1 Synthesis and Characterization

Synthesis of FB corrole, **1**, was achieved by following a general synthetic procedure of corrole synthesis.^{22, 23} For the synthesis of FB corrole, **2**, a synthetic procedure developed by Gryko *et al.* was followed.²⁴ For this purpose, 4-(chloroacetoxy)benzaldehyde, **5** was prepared by following an earlier reported synthetic protocol.²⁵ A dipyrromethane derivative namely, 2,2'-((2-bromo-5-fluorophenyl)methylene)bis(1H-pyrrole), **4** was also synthesized. In the next step, both the dipyrromethane and the 4-(chloroacetoxy) benzaldehyde were reacted in presence of TFA in dichloromethane solvent and subsequent oxidation with DDQ resulted the formation of **2**. Synthesis of FB corrole, **3**, was achieved after the de-protection of chloroacetoxy group in **2** with the help of benzyl amine (Scheme 4.2). Purity and identity of all the three FB corroles are demonstrated by their satisfactory elemental analyses and by the electrospray mass spectra (see Experimental Section).



Scheme 4.2. Synthesis of **3**.

4.3.2 Structures

The crystal structure of the FB corrole, **3** is shown in Figure 4.1. The crystal system is monoclinic and the unit cell has four corrole molecules. Important crystallographic parameters are presented in Table 4.1. Bond distances and angles agree well with the previously reported other FB corrole molecules.²⁶⁻²⁹

In the packing diagram of **3**, it has been observed that the inter-planar distance between the two corrole planes is $\sim 3.51 \text{ \AA}$. It appears that the two corrole molecules overlap appreciably with each other and forms sandwich type of configuration with two

hydroxyphenyl groups of two different corrole units are *trans* to each other. In addition to the strong sandwich type of π - π stacking interactions mediated by the central aromatic rings, another kind of moderately strong parallel displaced π - π stacking interactions has also been observed among the corrole units through the phenyl rings at the *meso*-positions of corrole. The dihedral angles observed among the phenyl groups and the corrole ring are found to be

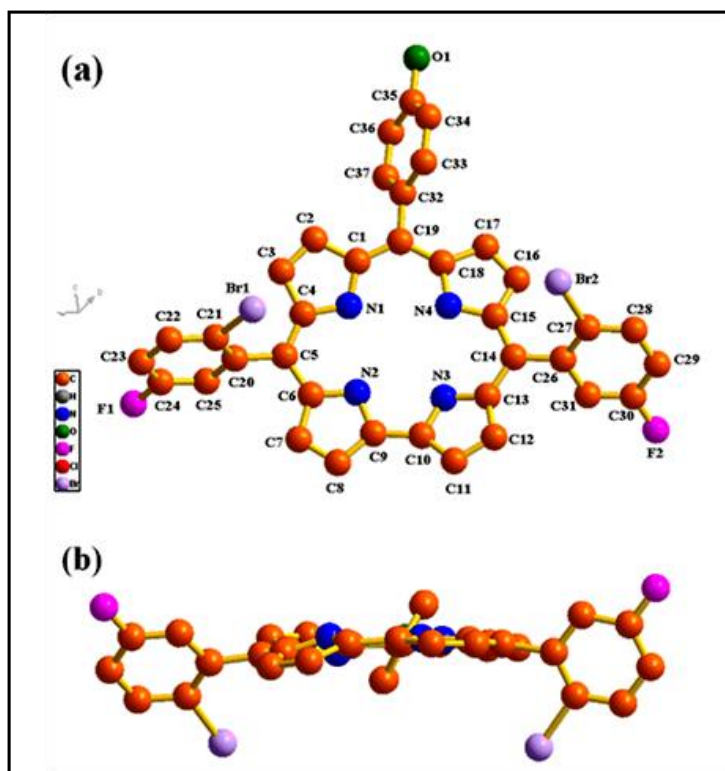


Figure 4.1. Single-crystal X-ray structure of **3**, (a) top view (b) side view. Hydrogen atoms omitted for clarity.

42.65°, 59.17°, and 67.84° and match well with those for analogous corrole derivatives.^{24, 26-}

²⁹ The deviation observed among the pyrrole rings from the mean corrole plane range from ~8.03°–23.55°. The crystal structure analyses of **3** show several O—H···N interactions. The OH group of the hydroxyphenyl moiety of one corrole appears to undergo hydrogen-bonding with the amine and imine nitrogen atoms of other corrole ring. The shortest distance responsible for this kind of hydrogen bonding interactions is 2.86 Å [bonding parameters of

Table 4.1 Crystallographic data for **3**

Compound code	3
Molecular Formula	C ₃₇ H ₂₂ Br ₂ F ₂ N ₄ O, 2CH ₂ Cl ₂
<i>F</i> _w	906.26
Radiation	MoK α
Crystal Symmetry	Monoclinic
Space group	P 2 ₁ /c
<i>a</i> (Å)	15.5405(10)
<i>b</i> (Å)	13.9867(9)
<i>c</i> (Å)	18.1492(13)
α (deg)	90
β (deg)	113.329(4)
γ (deg)	90
<i>V</i> (Å ³)	3622.4(4)
<i>Z</i>	4
μ (mm ⁻¹)	2.583
<i>T</i> (K)	293(2) K
<i>D</i> _{calcd} (g cm ⁻³)	1.662
2 θ range (deg)	4.08 to 51.46
<i>e</i> data (<i>R</i> _{int})	6673 (0.1189)
<i>R</i> ₁ (<i>I</i> >2 σ (<i>I</i>))	0.0674
w <i>R</i> ₂ (all data)	0.1900
GOF	1.023
Largest diff. peak and hole(e \cdot Å ⁻³)	2.384 and -1.531

O–H \cdots N; H \cdots N: 2.129Å; O \cdots N: 2.86 Å; \angle O–H \cdots N: 148.3°]. This kind of hydrogen bonding interactions among the corrole units leads to supramolecular assemblies. Thus the solid state structure gets some extra stability due to the favorable intermolecular O–H \cdots N interactions and extensive π - π stacking interactions (Fig. 4.2).^{24, 26-29}

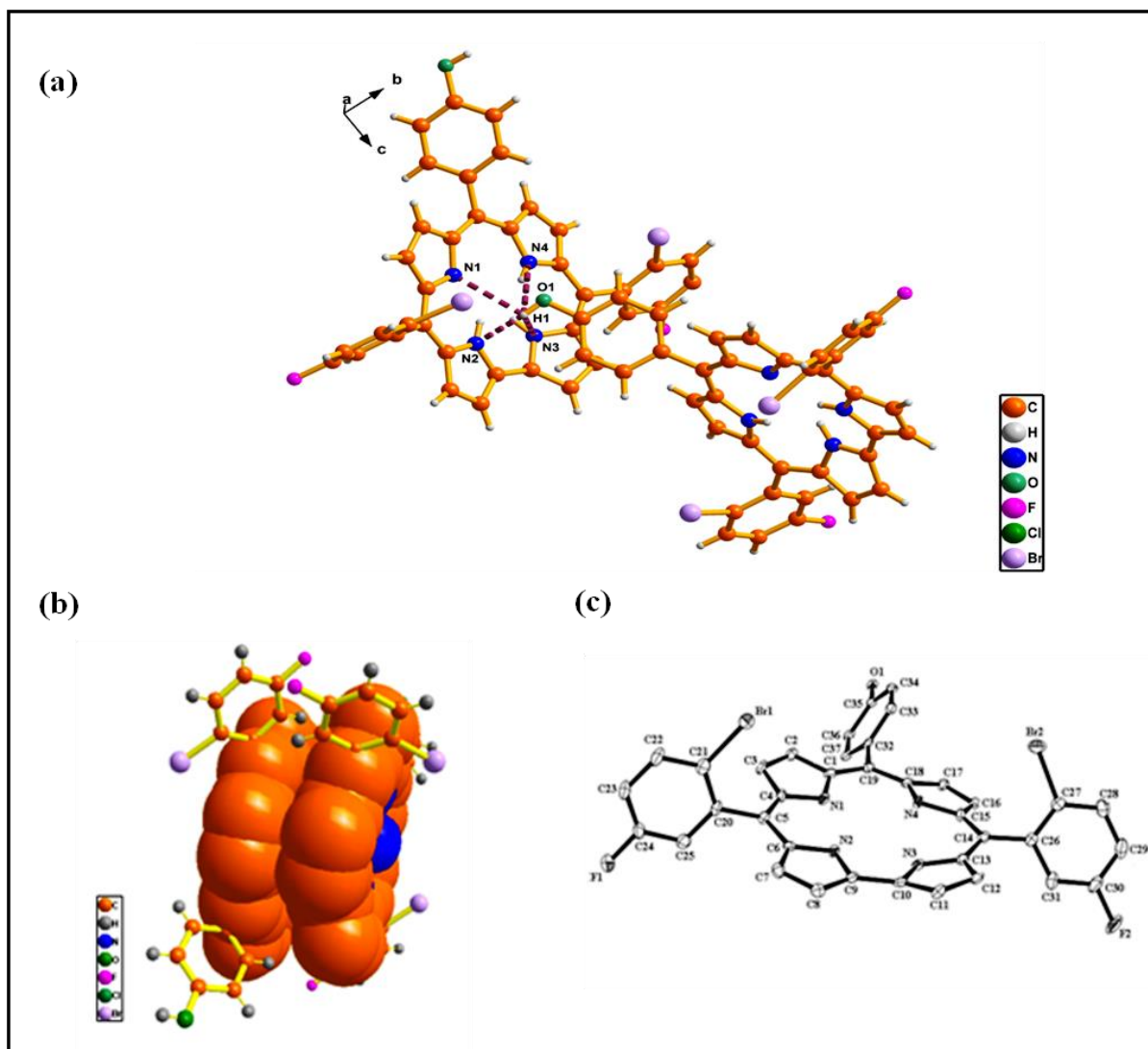


Figure 4.2. X-ray single crystal structure analysis of 10-(4-hydroxyphenyl)-5, 15-bis (2-bromo-5-fluorophenyl) corrole, **3**, (a) O—H···N interactions, [2.86 Å] (b) π - π stacking interactions [3.51 Å]. The entries in square brackets are the distances, and (c) ORTEP diagram of **3**. Solvent molecules are removed for clarity. Ellipsoids are drawn at 30% probability.

4.3.3 Electronic Spectra

The electronic absorption spectral data of **1-3** in dichloromethane are presented in Table 4.2 (Figure 4.3). The spectral profiles of these FB corroles can be easily explained with the help of Gouterman four-orbital model.³⁰ The Soret and Q-bands were observed at 418, 577, 620, and 654 nm respectively, for **1**, 409, 564, 607, and 643nm respectively, for **2**, and 410, 563, 608, and 638 nm respectively, for **3**. The observed band positions, spectral shapes and molar

extinction coefficients of these corrole derivatives matched well with previously reported other corroles.³¹⁻³⁴

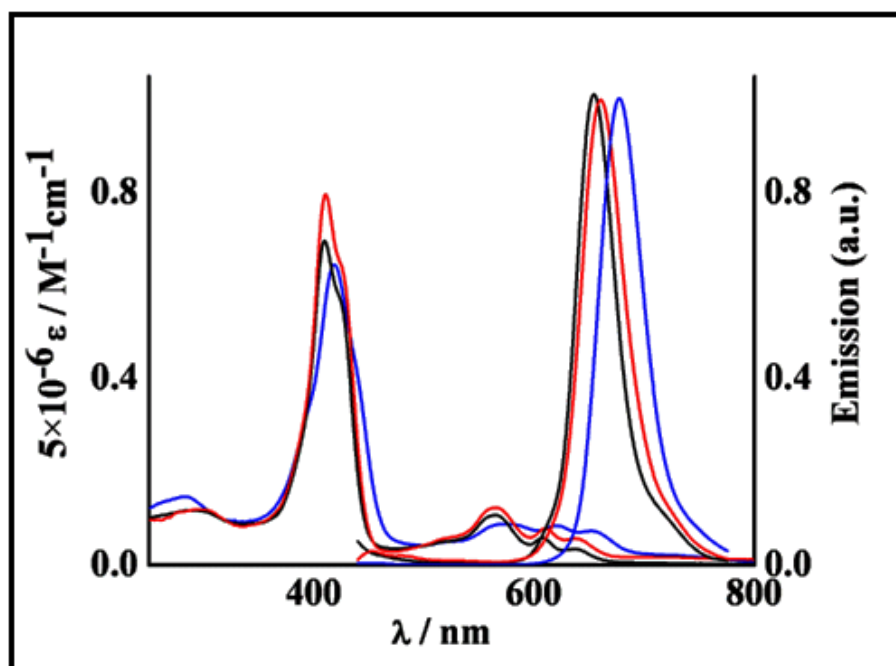


Figure 4.3. Electronic absorption and normalized emission spectrum of **1**, (blue line), **2**, (black line), and **3**, (red line) in CH_2Cl_2 .

4.3.4 Emission Spectra

The emission spectra of the compounds **1-3** in CH_2Cl_2 showed strong emissions in the red-region of the visible spectra. **1-3** displayed strong fluorescence with fluorescence maxima (λ_{max}) at 676, 654, and 661 nm upon excitation at their respective Soret bands (Figure 4.3, Table 4.2). The fluorescence lifetime of **1-3** were estimated to be 2.00, 0.43, and 0.34 ns respectively (Figure 4.4, Table 4.2). The quantum yields of **1-3** were obtained as 0.16, 0.04, and 0.04 respectively (Table 4.2).

The spectral positions, shapes and decay profiles matched nicely with the previously reported other FB corrole derivatives. Earlier report also suggests that this kind of emission occurs from the lowest lying singlet excited state in the FB corrole derivatives.^{35,36}

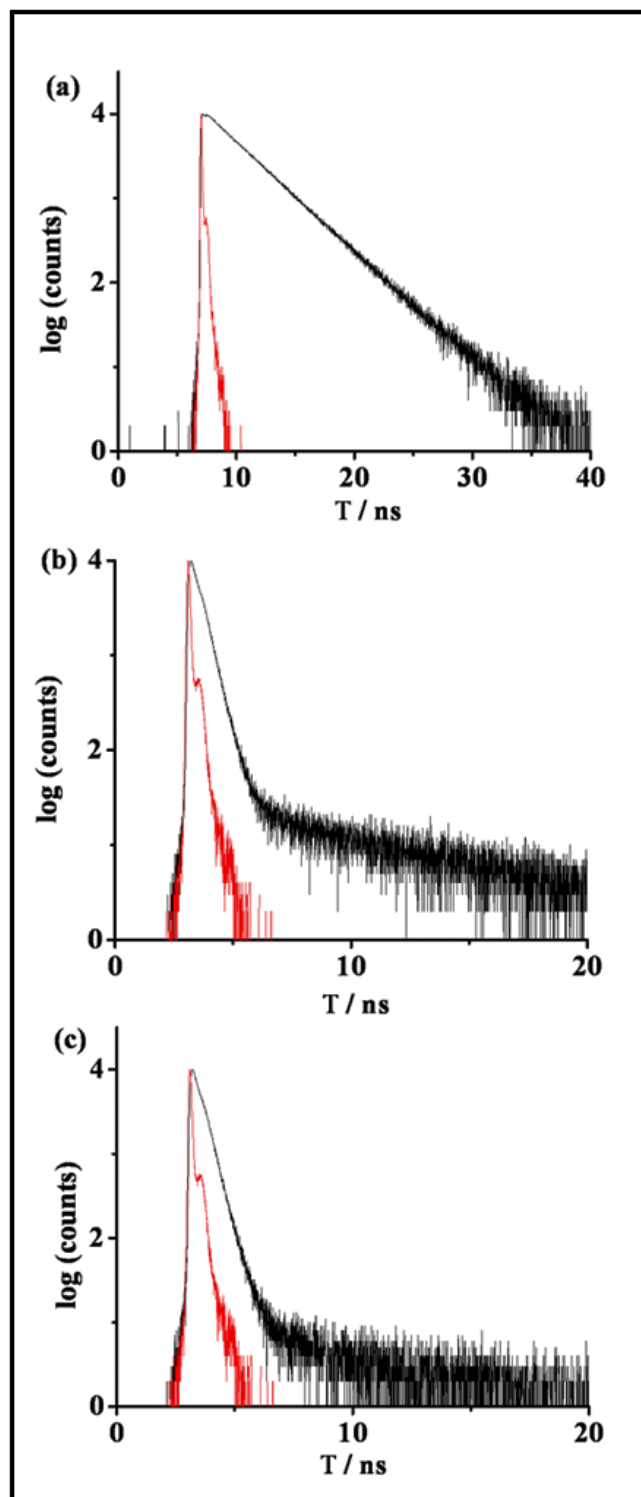


Figure 4.4. Fluorescence decay profiles of (a) **1**, (—); $\lambda_{em} = 676$ nm, (b) **2**, (—); $\lambda_{em} = 654$ nm, and (c) **3**, (—); $\lambda_{em} = 661$ nm. The black line represent experimental data, whereas the red line represents best fit.

Table 4.2. Fluorescence data^a of compounds 1-3.

Compound	Soret (nm)	Emission Maxima (nm) ^b	Φ_F^c	τ (ns)
1	418	676	0.16	2.00
2	409	654	0.04	0.43
3	410	661	0.04	0.34

^aIn dichloromethane. ^bExcited at the Soret band. ^cQuantum yields were calculated by following a standard protocol and by using H₂TPP as a reference compound.¹⁸

4.3.5 Self-aggregates of 1-3

The self-aggregates of all the three FB corroles were prepared on a silicon wafer as well as on a quartz substrate by using drop-casting method in a dichloromethane and methanol (1:2) solvent mixture. The generated aggregates were then examined by using SEM. The SEM images of the aggregates are shown in Figure 4.5, 4.6, and 4.7 respectively. Well defined and nicely organized three-dimensional objects with diameter of ca. 320 nm for **1** (Figure 4.5),

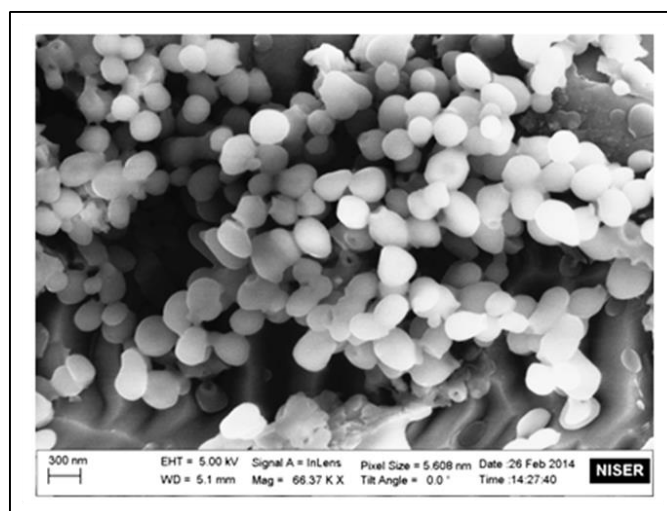


Figure 4.5. SEM images in dichloromethane-methanol mixture of **1**; nano hollow-spheres are seen

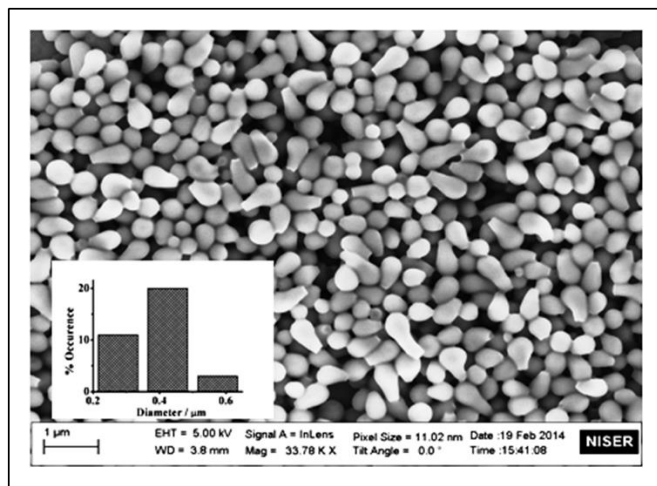


Figure 4.6. SEM images in dichloromethane-methanol mixture of **2**; nanobulbs are seen. Inset shows particle size distribution histograms of nanobulbs.

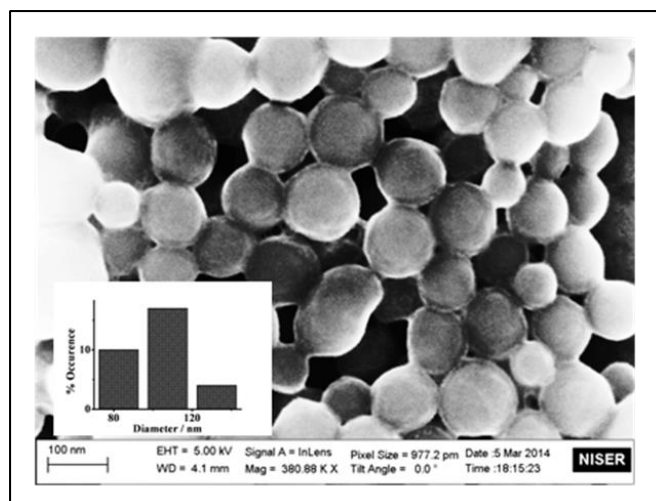


Figure 4.7. SEM images in dichloromethane-methanol mixture of **3**; nanodiscs are seen. Inset shows particle size distribution histograms of nanodiscs.

450 nm for **2** (Figure 4.6), and 120 nm for **3** (Figure 4.7) were obtained. In case of corrole **1**, it was nano hollow-spheres, for **2**, it was nanobulbs, and for **3**, it was nanodiscs. The observed shapes of the aggregates of all the three FB corroles, **1-3**, can be correlated with the help of a model proposed by Srinivasarao *et al.*³⁷ This model predicts the formation of three dimensional objects in the drop casting method wherein a solvent/solvent-mixture is used to dissolve the solid materials provided that one of the solvent components must be denser than water and the material has a significant level of intermolecular interactions in the solid state. Single crystal X-ray structure analysis of **3** eventually supports the existence of a significant

level of intermolecular interactions. It is highly likely that a similar type of intermolecular interactions also exists among the other two corrole molecules. The solute-solvent interaction ultimately changes the thermodynamics and the kinetics of the aggregation processes and leads to the generation of differently sized and shaped aggregates.³⁷⁻⁴⁰ To analyze the composition of the nano-aggregates, EDX analysis of the individual nanoparticles of FB corroles, **1-3**, was performed (Figure 4.8, 4.9, and 4.10). All the constituent elements of **1-3**

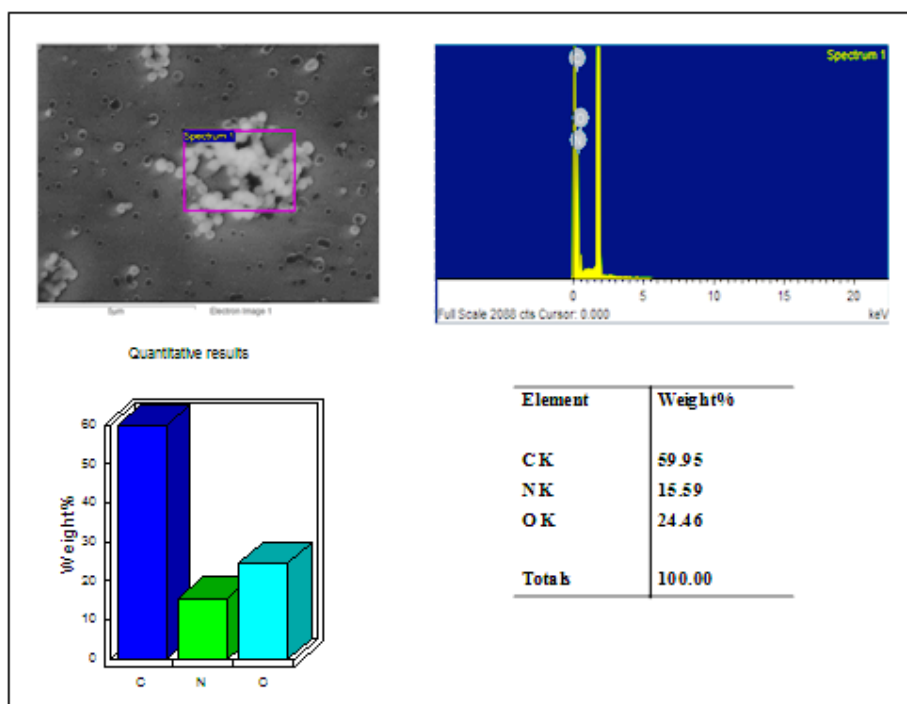


Figure 4.8. EDX elemental analysis obtained from the nano hollow-spheres of **1** showing the presence of the entire constituent elements: C, N, and O.

are present in those nanoparticles and their weight percentages are also very close to their actual weight percentages in the **1-3** molecules. It is worthwhile to mention here that in a dichloromethane and methanol (1:2) solvent mixture, there is no significant changes observed in the absorbance and emission spectra of the FB corroles **1-3** and so also in the dynamic light scattering (DLS) experiment in the solution phase (Figure 4.11).

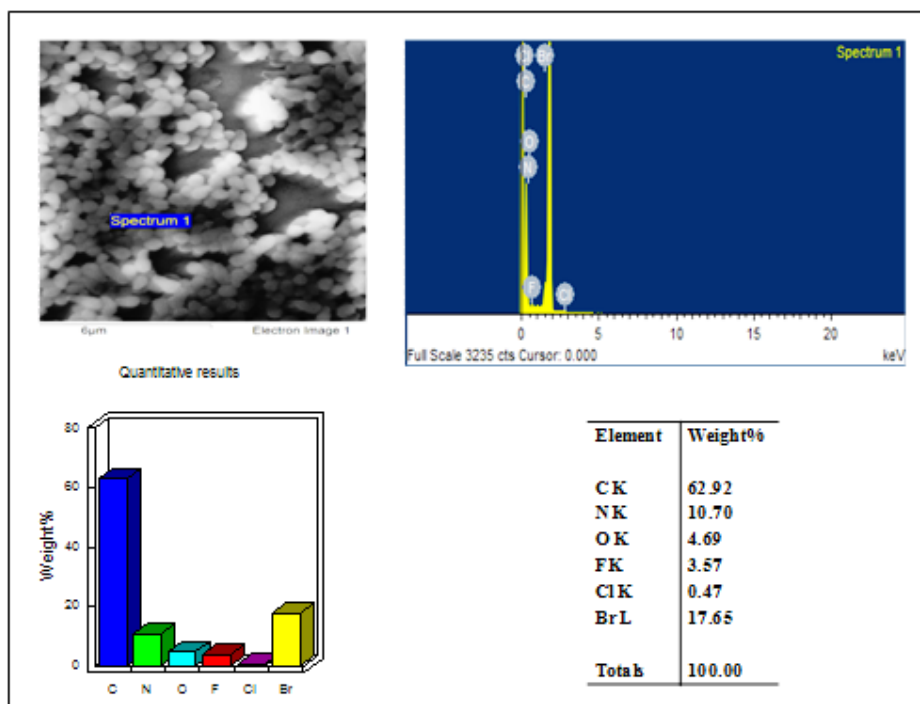


Figure 4.9. EDX elemental analysis obtained from the nanobulbs of **2** showing the presence of the entire constituent elements: C, N, O, F, Cl, and Br.

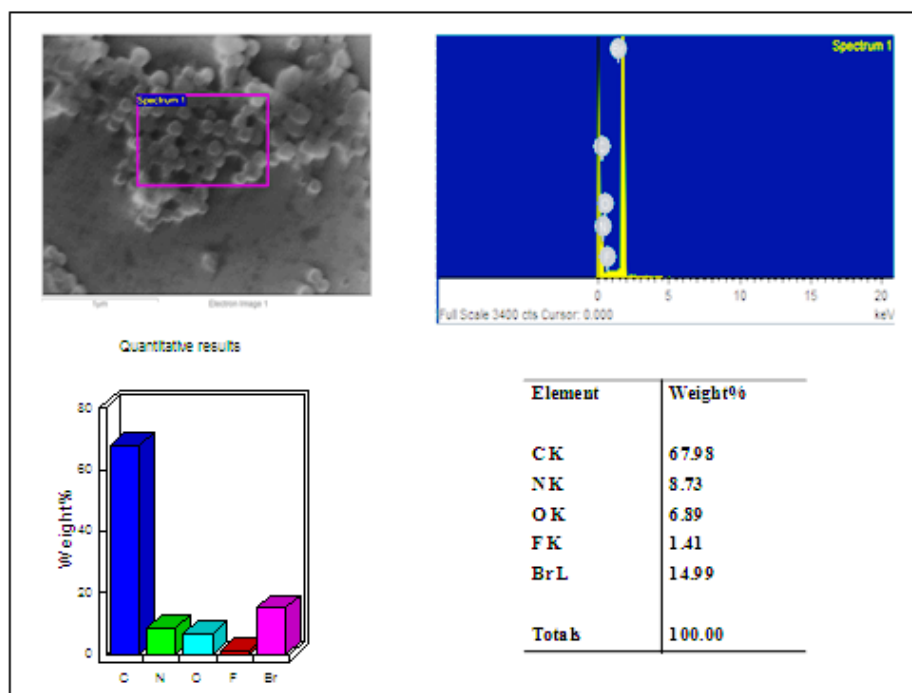


Figure 4.10. EDX elemental analysis obtained from the nanodiscs of **3** showing the presence of the entire constituent elements: C, N, O, F, and Br.

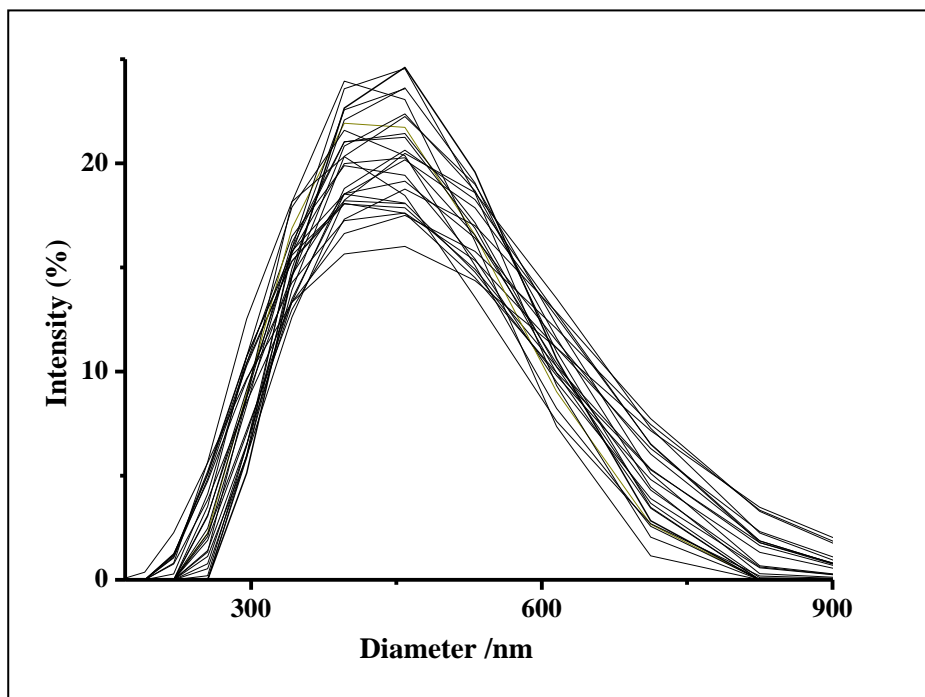


Figure 4.11. Changes in particle size distribution of the aggregates of **3** on letting it stay in DMF and H₂O (1:1) mixture. Measurements are made at 10 minutes interval.

4.3.6 Measurement of NLO properties

It is worthwhile to note that the thermo-optic effects such as thermal-lensing are always present due to high-repetition rate (80 MHz) of the fiber laser.⁴¹⁻⁴⁶ The onset of thermal-lensing is determined by a characteristic time (t_c) of the sample which is inversely proportional to its thermal diffusivity (D) and directly proportional to square of w_0 .^{39, 44} Typically, $D \sim 10^{-7} \text{ m}^2/\text{s}$ for organic solvents which results into $t_c \sim 1.0 \text{ ms}$ for beam waist varying between, $w_0 \sim 30\text{--}50 \text{ }\mu\text{m}$. If the time-difference between the two consecutive pulses is less than t_c , the accumulated thermal energy (ATE) would manifest in the form of thermal-lens in the samples. Keeping this point in mind, we control the sample irradiation by chopping the incident laser beam by using custom-made chopper wheel with 0.83% duty cycle. The chopper frequency is set at 40 Hz which result in an effective laser repetition rate of 664 kHz. Figure 4.12.a-f show the traces of normalized transmittance for **1-3** (0.1 mM solution in toluene) and **1-Nano**, **2-Nano**, **3-Nano** respectively as a function of z -axis

translation for incident on-axis peak optical irradiances $I_0 \approx 1-4 \text{ GW/cm}^2$ (dotted curves). It is evident that the transmittance curves have symmetrically placed peak and valley and therefore, lies in the regime of small nonlinear phase-shift ($\Delta\phi_0 \leq \pi$).^{47, 48}

4.3.7 Theoretical model for analyzing NLO responses

In order to ascertain the NLO parameters (n_2 and β) in presence of thermal nonlinearity such as thermal lensing, we employ the Gaussian decomposition (GD) technique after incorporating a non-local parameter (m). This idea was initially proposed by Ramirez *et al.*⁴⁷ so as to account for thermal effects. The inclusion of non-local term (m) brings in flexibility to consider spatial distribution of nonlinear phase-shift (ϕ) which can be wider as well as narrower than the incident Gaussian beam due to thermal contribution to optical nonlinearity. We consider a complex Gaussian beam (TEM_{00} mode) from a pulsed laser source to be incident on medium exhibiting $\chi^{(3)}$ nonlinearity. The complex field incident on the nonlinear medium is given by,⁴⁸

$$E(r, z, t) = E_i(t) \frac{w_0}{w(z)} \exp\left(-\frac{r^2}{w^2(z)} - \frac{ikr^2}{2R(z)}\right) e^{-i\phi(z,t)} \quad \dots (4.1)$$

where $w(z) = w_0 / [1 + (z/z_r)^2]^{1/2}$ is the beam radius at z (Figure 4.13), $R(z) = z [1 + (z_r/z)^2]^{1/2}$ is the radius of curvature, $z_0 = (1/2)kw_0^2$ is Rayleigh length for the focused Gaussian beam, $k = 2\pi n_0 / \lambda = \omega_0 / c$ is the wave number and E_i is the incident electric field amplitude in Equation 4.1. Here, ω_0 , λ are angular frequency, wavelength of em wave respectively. The term $e^{i\phi(z,t)}$ contains all the radially uniform phase-variations and hence, does not play a significant role in analyzing self-focusing or self-defocusing effects. In presence of linear and nonlinear effects, the intensity at exit-plane of a thin sample of length L ($\ll z_0$) is given by Equation 4.2,⁴⁸

$$I_e(z, r) = \frac{I_i(z, r)e^{-\alpha_0 L}}{1 + q(z, r)} \quad \dots (4.2)$$

where $I_i(z,r)$ represents the laser beam intensity at sample entrance plane, $q(z,r) = \beta I(z,r)L_{eff}$ is the normalized nonlinear absorption parameter and β is two-photon absorption coefficient. Here, α_0 is the linear absorption coefficient and $L_{eff} = (1 - e^{-\alpha_0 L}) / \alpha_0$ is the effective length traversed by

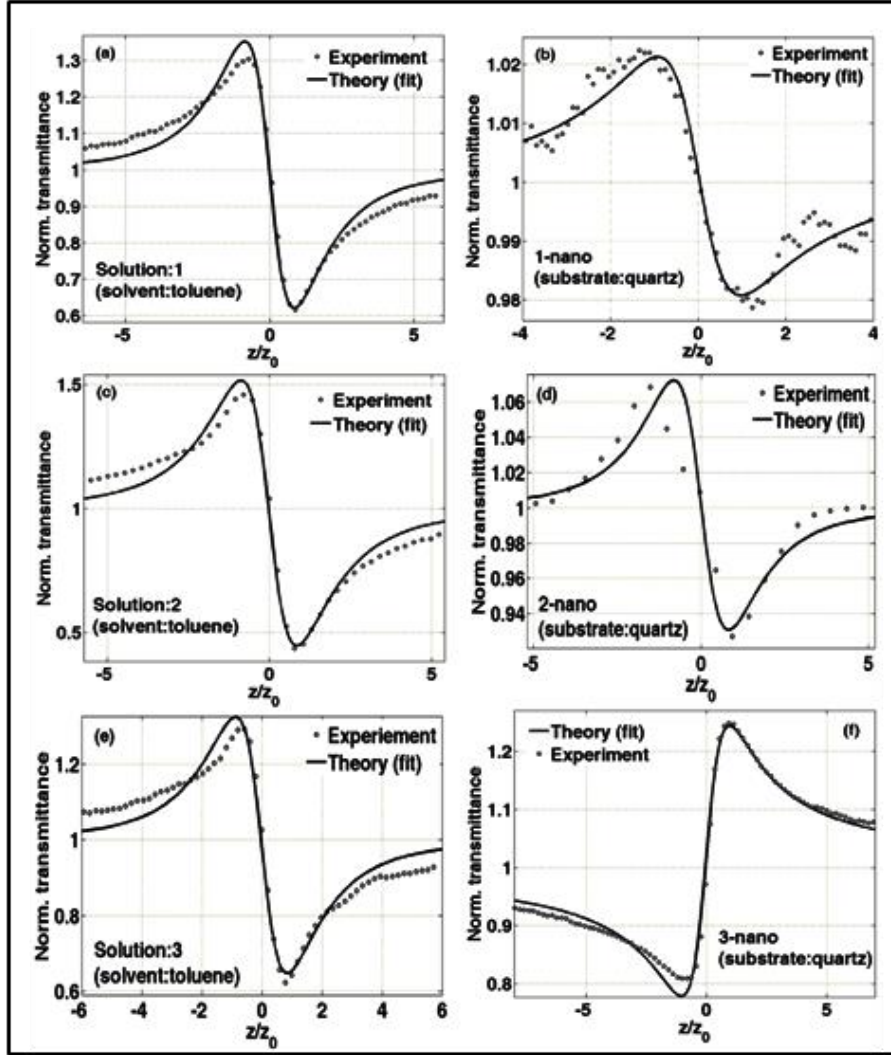


Figure 4.12. Closed aperture normalized transmittance as a function of propagation distance (z) for (a) 0.1 mM solution **1** (in toluene), (b) Aggregates of **1** (1-Nano on quartz substrate) (c) 0.1 mM solution of **2** (in toluene), (d) Aggregates of **2** (2-Nano on quartz substrate), (e) 0.1 mM solution of **3** (in toluene), (f) Aggregates of **3** (3-Nano on quartz substrate).

the beam in sample. By using the GD method, the nonlinear phase change is given by

$$\Delta\varphi(z,r) = \frac{kn_2}{\beta} \ln[1 + q(z,r)] \quad \text{where } n_2 \text{ is nonlinear refractive index of the sample.}^{49-52}$$

In order to account for non-local effects, nonlinear absorption parameter could be defined as given in Equation 4.3 below.

$$q(z, r) = \frac{q_0}{1 + (z/z_0)^2} \exp\left(\frac{-2mr^2}{w^2(z)}\right) \quad \dots (4.3)$$

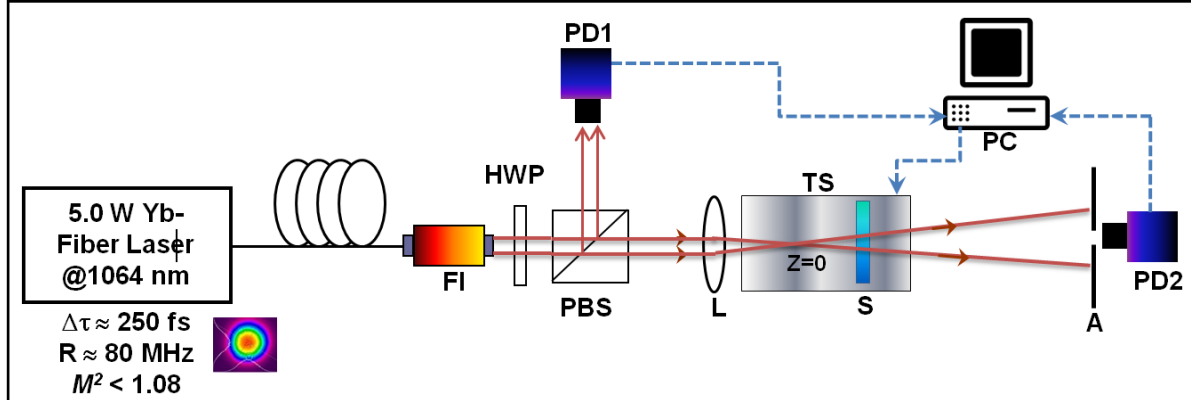


Figure 4.13. Z-scan experimental set-up using Yb-fiber laser source; FI: Fiber laser; HWP: Half-wave plate; PBS: Polarizing beam-splitter; L: Lens ($f = 100$ mm); TS: Translation stage (10 cm travel; S: Sample; A: Aperture ($S \sim 0.3$); PD1: Reference photodetector; PD2: Signal photodetector.

where $q_0 = \beta I_0 L_{eff}$ with I_0 being the on-axis beam intensity at focus. The parameter ‘ m ’ is defined as order of non-locality and can be any real positive number. For $m < 1$, the nonlinear phase change extends beyond the spatial incident intensity distribution whereas when $m > 1$, the nonlinear phase change is narrower than the spatial extent of incident intensity distribution. When $m = 1$, the nonlinear phase change has identical variation as that of incident intensity and the response can be considered as local. This would result in transmittance as given by Sheik-Bahae *et al.*⁴⁸

It is to be appreciated that $q(z)$ is usually very small, so that we can assume

$\Delta\phi(z, r) \approx \frac{kn_2}{\beta} q(z, r) = \Delta\phi_0(z) \exp\left(\frac{-2mr^2}{w^2(z)}\right)$ where $\Delta\phi_0 = \frac{\Delta\Phi_0}{1 + (z/z_0)^2}$. Here, $\Delta\Phi_0 = kn_2 I_0 L_{eff}$ this defines on-axis phase-shift at the focus due to refractive nonlinearity. Using the GD method and Equation 4.1, the electric field at the sample exit plane is given by,^{48, 52}

$$E_e(r, z) = E(r, z) e^{-\frac{m\phi}{\beta}} \sum_{n=0}^{\infty} \left[\frac{(i\Delta\phi_0(z))^n}{n!} \times \prod_{n=0}^n \left(1 - i(2n-1) \frac{\beta}{2kn_2}\right) \right] \times \exp\left(\frac{-2mn'r^2}{w^2(z)}\right) \quad \dots (4.4)$$

By assuming that the field in Equation 4.4 propagates to aperture plane undergoing only diffraction, the electric field at aperture plane can be written as shown in Equation 4.5 below.

$$E_{out}(r, z) = E(r, z=0) e^{-\frac{q_0 L}{2}} \sum_{n=0}^{\infty} \left[\frac{(i \Delta \Phi_0(z))^{2n}}{n!} \times \prod_{n=0}^n \left(1 - i(2n-1) \frac{\beta}{2kz} \right) \frac{w_{n0}}{w_n} \right] \times \exp \left(\frac{-r^2}{w_n^2} - \frac{ikr^2}{2R_n} + i\theta_n \right) \quad \dots \quad (4.5)$$

where $w_{n0} = w^2(z)/(2n+1)$, $d_n = (1/2)kw_{n0}^2$, $R_n = d \left(1 - \frac{g}{g^2 + (d^2/d_n^2)} \right)^{-1}$, $w_n^2 = w_{n0}^2 (g^2 + d^2/d_n^2)$, $\theta_n = \tan^{-1} \left(\frac{d/d_n}{g} \right)$ and $g = 1 + d/R(z)$. Here, ‘d’ is the distance between sample exit plane and the aperture. Therefore, the normalized transmittance through a finite aperture of radius r_a would be given by the ratio of on-axis electric field in presence of nonlinear phase-shift and that in absence of any nonlinear effect i.e.

$$T(z, \Delta \Phi_0) = \frac{|E_{out}(z, r=0, \Delta \Phi_0)|^2}{|E_{out}(z, r=0, \Delta \Phi_0 = 0)|^2} \quad \dots \quad (4.6)$$

which can be simplified to obtain,^{47, 49}

$$T(z, \Delta \Phi_0, q_0) = 1 - \frac{4m \Delta \Phi_0 x + q_0 (x^2 (2m+1))}{(x^2 + (2m+1)^2)(x^2 + 1)} \quad \dots \quad (4.7)$$

where $x = z/z_0$ and we have assumed that $d \gg z_0$. Hence, Equation 4.7 is used for obtaining ‘ n_2 ’ and ‘ β ’ simultaneously from the experimentally measured normalized transmittance.

4.3.8 Results

Using the variation of normalized transmittance as shown in Figures 4.12.a-f as well as Equation 4.7, we obtained the values of nonlinear refractive index (n_2) and two-photon absorption coefficient (β) as shown in Table 4.3. It is apparent that the n_2 values of aggregates of **1-3** are about three orders of magnitude greater than that of solutions. Similarly, β for **1-Nano**, **2-Nano** and **3-Nano** exhibit about two orders of enhancement in magnitude as compared to the solutions. The obvious reason behind such an observation is an increase in overall density of molecules in solid aggregates as compared to their solutions. Due to higher density of molecules in aggregates in addition to low mobility in solid phase, the contribution

to nonlinear optical effects is higher. Moreover, the solutions, namely **1-3** exhibit self-defocusing effect (negative n_2) in addition to positive nonlinear absorption (β). Usually, such a behavior is expected in solutions due to reduction in local density at high beam intensities which result in a negative (concave) lensing behavior. It was also observed that **1-Nano** and **2-Nano** defocuses the incident laser beam whereas **3-Nano** exhibits a self-focusing effect. Such a behavior clearly indicates that the impact of electrostriction in **3-Nano** masks other effects such as thermal lensing, photochemical ablation at femtosecond laser intensities, thereby resulting in positive-lensing behavior.⁵³

Although, molecules **2** and **3** resemble each other closely, the small nonlinear response as well as earlier onset of thermal effects at repetition rates ≥ 1 kHz in **2-Nano**, results in a self-defocusing behavior in aggregate phase. It is worthwhile to note that the nonlinear response (n_2 and β) of **3-Nano** are significantly higher as compared to other samples under study and the values are reasonable higher to related materials reported in literature (Table 4.4)⁵⁴⁻⁵⁹ For example, the two-photon absorption coefficient (β) for **3-Nano** is more than 100 times greater in magnitude as compared to **1-Nano** and about 200 times than that for **2-Nano**. The two-photon absorption cross-sections of different *meso*-substituted A₃-corroles were extensively studied by Rebane *et al.*¹⁵ They have observed values of 60–130 GM. Osuka *et al.* have studied the corrole dimers and have obtained values of 1100– 4600 GM.⁵⁴ Rao *et al.* have studied the germanium and phosphorus corroles and have obtained values of 100–5400 GM.¹⁶ In our case we have obtained values of 60-550 GM in solution phase measurement. A closer look reveals that our values are also in line with the previously reported data in solution phase measurement. However absorption cross-sections were never measured in corrole aggregates. The values obtained by us in the aggregated state are 100-1000 times higher in comparison to the values obtained in solution. In general polarizability and ground state dipole moment dictates the NLO responses. The molecular ground state

dipole moment has been calculated by using the DFT calculations (Figure 4.14). The values obtained are in the same order of magnitudes (3.05, 1.67, and 2.45 Debye respectively for the FB corroles **1-3**). The large improvement of nonlinear optical behavior for **1-Nano**, **2-Nano** and **3-Nano** could be attributed due to the presence of coupled MOs and thus resulting in an enhanced transition dipole moment.

Table 4.3. UV-Vis data^a and NLO coefficients^{a,b}

Compound	UV-Vis data ^a λ_{\max} / nm ($\epsilon/M^{-1}cm^{-1}$)	$n_2(\times 10^{-18})$ m^2/W	β (GM)	$\beta(\times 10^{-15})$ m/W
1^a	421 (132000), 574 (15000), 620 (14250), 654 (11000).	-16.8	176	5.7
2^a	412 (119000), 565 (20000), 610 (9000), 643 (4000).	-7.8	59	1.9
3^a	410 (162500), 565 (24000), 612 (14000), 643 (11000).	-25.9	534	17.2
1-Nano	—	-1.1×10^3	—	4.0×10^2
2-Nano	—	-1.9×10^3	—	2.0×10^2
3-Nano	—	71.8×10^3	—	444×10^2

^aIn toluene

^b $\lambda_{\text{ex}}=1064$ nm

Table 4.4. σ_{TPA} values for related compounds

Compound	Solvent	Method	n_2	σ_{TPA}	Ref.
TTC	CH ₂ Cl ₂	Z-scan	-60×10^{-16} (cm ² /W)	1408-5410 GM	16
TPC	CH ₂ Cl ₂	Z-scan	-100×10^{-16} (cm ² /W)	2301-2576 GM	16
PTTC	CH ₂ Cl ₂	Z-scan	-5.1×10^{-16} (cm ² /W)	233-543 GM	16
GeTTC	CH ₂ Cl ₂	Z-scan	-7.6×10^{-16} (cm ² /W)	112-239 GM	16
A ₃ -Corroles	CCl ₄			130 ± 26 GM	15
DH ₃ CD	CH ₂ Cl ₂	Z-scan		1100 GM	53
DH ₂ CD	CH ₂ Cl ₂	Z-scan		3700 GM	53
DZnCD	CH ₂ Cl ₂	Z-scan		4600 GM	53
H ₂ TPP	Toluene			1-25 GM	54
1a	CHCl ₃			56 (8) GM	55
1b	CHCl ₃			187 (62) GM	55
CuTPP	CHCl ₃			101 (32) GM	55
PEP	CHCl ₃			<5 GM	55
AF-250	CHCl ₃			30 GM	55
BDPAS- porphyrin dyad	Different Solvents			1000 GM	56
4D	CHCl ₃			370 GM	57
5D	CHCl ₃			7600 GM	57
5M	CHCl ₃			1800 GM	57
7M	CHCl ₃			1200 GM	57
8	CHCl ₃			1000 GM	57
Porphycenes	CHCl ₃	Z-scan		8–21 × 10 ³ GM	58
1	Toluene	Z-scan	16.8×10^{-18} (m ² /W)	5.7×10^{-12} m/W	This work
2	Toluene	Z-scan	7.8×10^{-18} (m ² /W)	1.9×10^{-12} m/W	This work
3	Toluene	Z-scan	25.9×10^{-18} (m ² /W)	17×10^{-12} m/W	This work
1-nano	–	Z-scan	1.1×10^{-15} (m ² /W)	4.0×10^{-10} m/W	This work
2-nano	–	Z-scan	1.9×10^{-15} (m ² /W)	2.0×10^{-10} m/W	This work
3-nano	–	Z-scan	71.8×10^{-15} (m ² /W)	444×10^{-10} m/W	This work

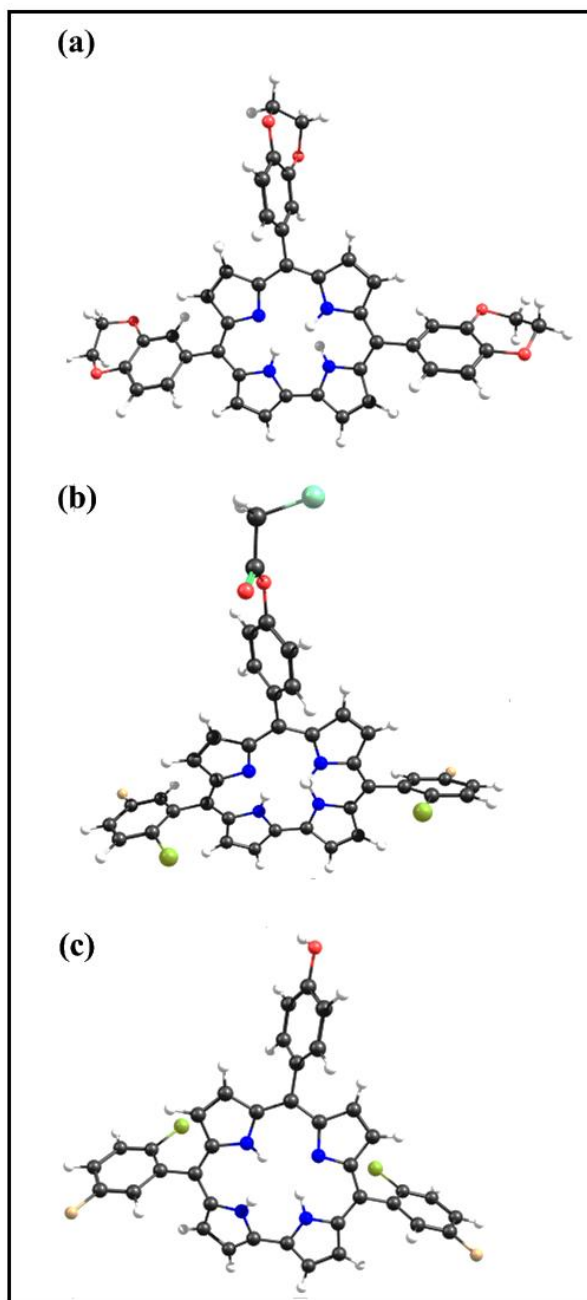


Figure 4.14. DFT optimized (BP-86/TZVP) structures of (a) **1**, (b) **2**, and (c) **3**, obtained are in the same order of magnitudes (3.05, 1.67, and 2.45 Debye respectively for the FB corroles **1-3**).

4.4 Conclusions

The present work describes the synthesis of one novel A_3 -corrole and two novel *trans*- A_2B -corroles. Purity and identity of all the three FB corroles are demonstrated by various spectroscopic techniques. The crystal structure analysis of the FB corrole, **3** are also described. Extensive intermolecular O—H \cdots N interactions and π - π stacking interactions are

observed in the single crystal X-ray structural analysis the FB corrole **3**. The self-aggregates of all the three corroles were generated on a silicon wafer as well as on quartz substrate by using drop-casting method in a dichloromethane and methanol (1:2) solvent mixture. The generated aggregates were then examined by using SEM techniques. The NLO properties of FB corroles; **1-3** are studied in the solution as well as in the aggregated state (in the form of thin films). The results show that the nonlinear refractive index, n_2 , as well as two-photon absorption coefficient (β) of corrole **3** (in toluene solution) and its solid aggregates (**3-Nano**) are significantly greater than that of corroles **1** and **2**. Our study indicates that the corrole-**3** and **3-Nano** are promising candidates (Table 4.4) for devising optical switches which can have direct applications in high-speed communication technology.

4.5 Experimental Section

4.5.1 Materials

The precursors pyrrole, 2-bromo-5-fluorobenzaldehyde, DDQ (2, 3-dichloro-5, 6-dicyano-1, 4-benzoquinone), and trifluoroacetic acid were purchased from Aldrich, USA. 4-hydroxybenzaldehyde, benzylamine, reagent grade THF, ethanol, dichloromethane, chloroacetylchloride, and triethylamine were purchased from Merck, India. Hexane and CH_2Cl_2 were distilled from KOH and CaH_2 respectively. For spectroscopic studies HPLC grade solvents were used.

4.5.2 Physical Measurements.

UV–Vis spectral studies were performed on a Perkin-Elmer LAMBDA-750 spectrophotometer. Emission spectral studies were performed on a Perkin Elmer, LS 55 spectrophotometer using optical cell of 1 cm path length. The fluorescence quantum yields were determined using tetraphenylporphyrin [TPP] as a reference.¹⁸ Time resolved fluorescence measurements were carried out using a time-correlated single photon counting (TCSPC) spectrometer (Edinburgh, OB 920). The elemental analyses were carried out with a

Perkin-Elmer 240C elemental analyzer. The NMR measurements were carried out using a Bruker AVANCE 400 NMR spectrometer. Chemical shifts are expressed in parts per million (ppm) relative to residual chloroform ($\delta= 7.26$). Electrospray mass spectra were recorded on a Bruker Micro TOF-QII mass spectrometer. SEM images of the nanoparticles were captured by using a field emission gun scanning electron microscope (FEGSEM) (Zeiss, Germany make, Supra 55) equipped with energy-dispersive X-ray analysis system (EDX). All the calculations were performed with the program package TURBOMOLE 6.4 using density functional theory (DFT).^{60,61} The BP86 functional and TZVP basis set together with the resolution-of-the-identity (RI) approximation⁶²⁻⁶⁴ (RI-BP86/TZVP in short) was employed for the structure optimization procedure. Numerical frequency calculations of the optimized structures were done to ensure that the optimized structures were true minima not the transition states.

4.5.3 Crystal Structure Determination

Single crystals of **3** were grown by slow diffusion of a solution of the corrole in dichloromethane into hexane, followed by slow evaporation under atmospheric conditions. The crystal data of **3** was collected on a Bruker Kappa APEX II CCD diffractometer at 293 K. Selected data collection parameters and other crystallographic results are summarized in Table 4.1 and Figure 4.1. All data were corrected for Lorentz polarization and absorption effects. The program package SHELXTL⁶⁵ was used for structure solution and full matrix least squares refinement on F^2 . Hydrogen atoms were included in the refinement using the riding model. Contributions of H atoms for the water molecules were included but were not fixed.

4.5.4 NLO measurements

The NLO properties (nonlinear refractive index, n_2 and two-photon absorption coefficient, β) of corrole derivatives **1-3** and aggregates of **1-3** (namely **1-Nano**, **2-Nano**, **3-Nano**) were

measured using Z-Scan technique which employs an ultrafast laser source. Since, the absorption spectra revealed Q-band tails up to ~660 nm, we chose to measure the nonlinear response in the near-infrared region at a wavelength of 1064 nm so as to have minimal manifestation due to linear absorption and non-parametric effects. Our closed-aperture Z-scan set-up comprises a femtosecond (fs) Yb-fiber laser, delivering a linearly-polarized pulses of 250 fs at 80 MHz repetition rate at 1064 nm wavelength with maximum average output power of 5.0 W as shown in Figure 4.13. For varying the irradiance, we used a combination of half-wave plate (HWP) and polarizing beam splitter (PBS) after the isolator. *Via* this configuration, we vary the pulse energy of incident radiation varies from 1.2 nJ to 12 nJ. It is important to note that the fiber laser architecture ensures that the output power is delivered in TEM_{00} mode with $M^2 \leq 1.08$. This is an extremely crucial aspect of Z-Scan technique which essentially allows Gaussian-beam decomposition (GD) method to be employed for ascertaining the nonlinear refractive index (n_2) and nonlinear absorption (β) simultaneously as described below.^{1,2} The output pulses were focused using a combination of diverging lens ($f = -100$ mm) and converging lens ($f = +100$ mm) resulting in a beam waist varying between $30 \pm 1 \mu\text{m} \leq w_0 \leq 50 \pm 1 \mu\text{m}$. 0.1 mM solutions of corrole derivatives **1-3** in toluene were prepared and a 1.0 mm thick cuvette carrying the solution was mounted on a motorized translation stage (10.0 cm travel) thus, ensuring that the sample translation is more than 25 times of the Rayleigh range (z_0) along the path of beam. The transmitted beam intensity was recorded in a photodetector after passing through an aperture of transmittance 'S'. Following an identical procedure, the closed-aperture Z-scan measurements of aggregates of **1-3** i.e. **1-Nano**, **2-Nano**, **3-Nano** on a quartz substrate is carried out. It is to be mentioned that the nonlinear response of toluene and quartz plate were used as a standard for measuring n_2 and β of solutions and their aggregates respectively.

2,2'-((2-Bromo-5-fluorophenyl)methylene)bis(1H-pyrrole), 4.

In a 100 mL two-necked round-bottomed flask, 2 g of 2-bromo-5-fluorobenzaldehyde (9.85 mmol) was dissolved in 13.7 mL of freshly distilled pyrrole (197 mmol) and stirred for 20 min at room temperature. 151 μ L of TFA (1.97 mmol) was added drop wise to this mixture. The reaction mixture was then stirred at room temperature under N₂ atmosphere. The color of the solution gradually changed to dark orange. It was then dissolved with dichloromethane and washed several times with dilute NaOH solution, water and finally with brine solution. Organic layer was dried over anhydrous Na₂SO₄. It was evaporated and finally purified by column chromatography (silica gel 100-200 mesh, EtOAc / Hexane) to yield white color solid materials as final product. Yield: 80% (2.5g). Anal. Calcd (found) for C₁₅H₁₂BrFN₂: C, 56.45 (56.57); H, 3.79 (3.69); N, 8.78 (8.87). ¹H NMR (400 MHz, CDCl₃) δ 7.964 (brs, 2 H), 7.54-7.51 (m, 1 H), 6.89-6.82 (m, 2 H), 6.73-6.71 (m, 2H), 6.19-6.18 (m, 2H), 5.88 (brs, 2H), 5.83 (singlet,1H), (Figure 4.15). ESI-MS: m/z = 319.00 [**2a**+H]⁺ (319.0168 calcd. for C₁₅H₁₃BrFN₂) (Figure 4.16).

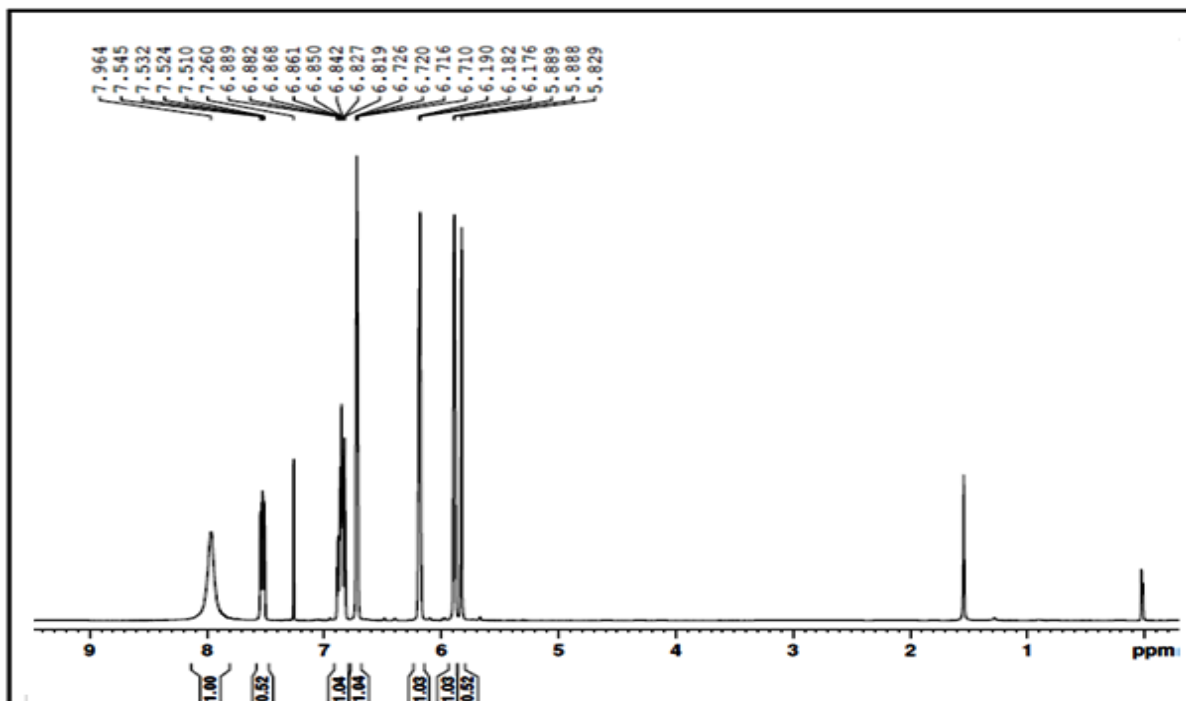


Figure 4.15. ¹H NMR spectrum of 2,2'-((2-bromo-5-fluorophenyl)methylene) bis(1H-pyrrole) in CDCl₃.

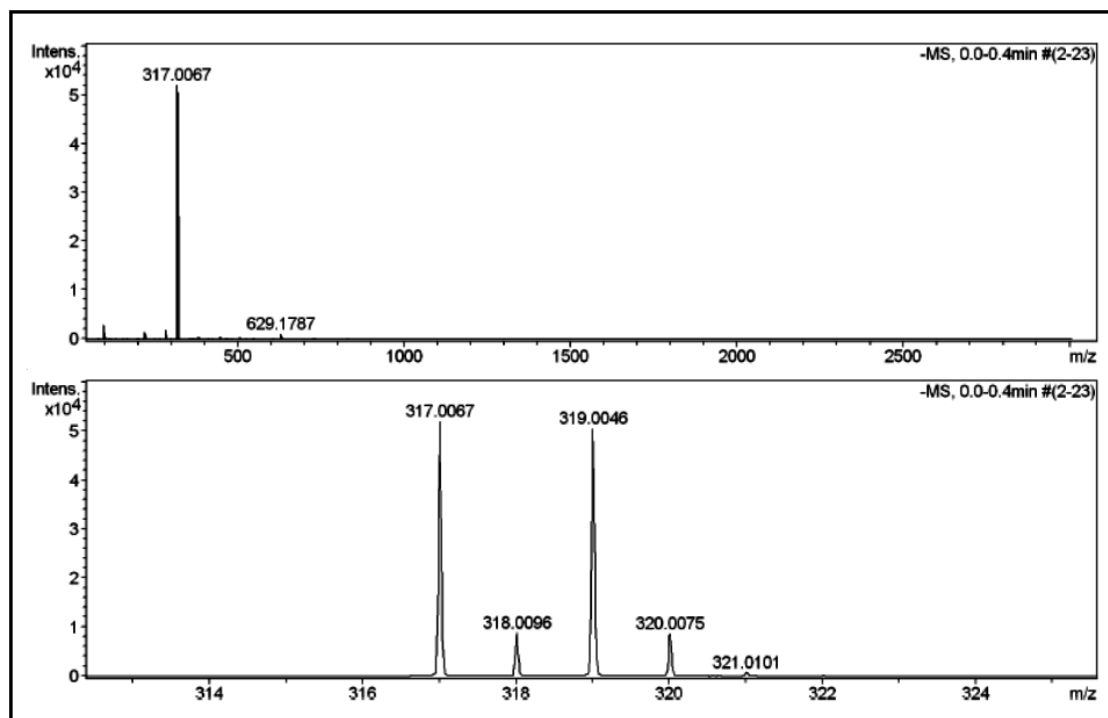


Figure 4.16. ESI-MS spectrum of 2,2'-(2-bromo-5-fluorophenyl)methylene)bis(1*H*-pyrrole) in CH₃CN shows the measured spectrum with isotopic distribution pattern.

4-(Chloroacetoxy)benzaldehyde, **5**.

4-(Chloroacetoxy)benzaldehyde was prepared by following a literature procedure.²⁵

5,10,15-Tris[3,4-(1,4-dioxan)phenyl]corrole, **1**.

1 was prepared according to available procedures of corrole synthesis.^{22,23} 0.820 g of **1**, 4-benzodioxan-6-carboxaldehyde (5 mmol) and 697 μ L of pyrrole (10 mmol) were dissolved in 400 mL of (1:1) MeOH/H₂O mixture. HCl (36%, 4.25 mL) was then added drop wise to this reaction mixture. The reaction mixture was kept at stirring for 3 h at room temp. During the course of the reaction, the reaction mixture was changed its color from orange to dark greenish brown. The reaction mixture was then extracted with CHCl₃; the organic layer was washed thrice with H₂O, dried by anhydrous Na₂SO₄, and filtered, and diluted to 300 mL with CHCl₃. Then 1.23 g of *p*-chloranil (5 mmol) was added, and the reaction mixture was refluxed for 1.5 h. The solvent was removed by rotary evaporation and the dark green colored crude product was purified by column chromatography through silica gel (100-200 mesh) column using 80% DCM and 20% hexane as eluent. Subsequent recrystallization

(CH₂Cl₂/hexane) gave the pure free base corrole, **1**. Yield: 18% (200mg). Anal. Calcd (found) for C₄₃H₃₂N₄O₆ (**1**): C, 73.70 (73.54); H, 4.60 (4.47); N, 8.00 (7.86). λ_{max} /nm (ϵ /M⁻¹cm⁻¹) in dichloromethane: 418 (129000), 577 (17300), 620 (16800), 654 (14500) (Figure 4.3). ¹H NMR (400 MHz, CDCl₃) δ : 8.89 (brs, 4 H), 8.58 (brs, 4H), 7.86-7.81 (m, 4 H), 7.67-7.62 (m, 2 H), 7.29-7.20 (m, 3 H), 4.48 (brs, 12 H), 1.49 (brs, 2H), -1.90 (brm, 1H) (Figure 4.17). ESI-MS: m/z =701.23 [**1**+H]⁺ (701.2322 calcd for C₄₃H₃₃N₄O₆) (Figure 4.18). M.p>300°C. **1** displayed strong fluorescence at 676 nm (Figure 4.3), with excited state life time of 2.00 ns (Figure 4.4)

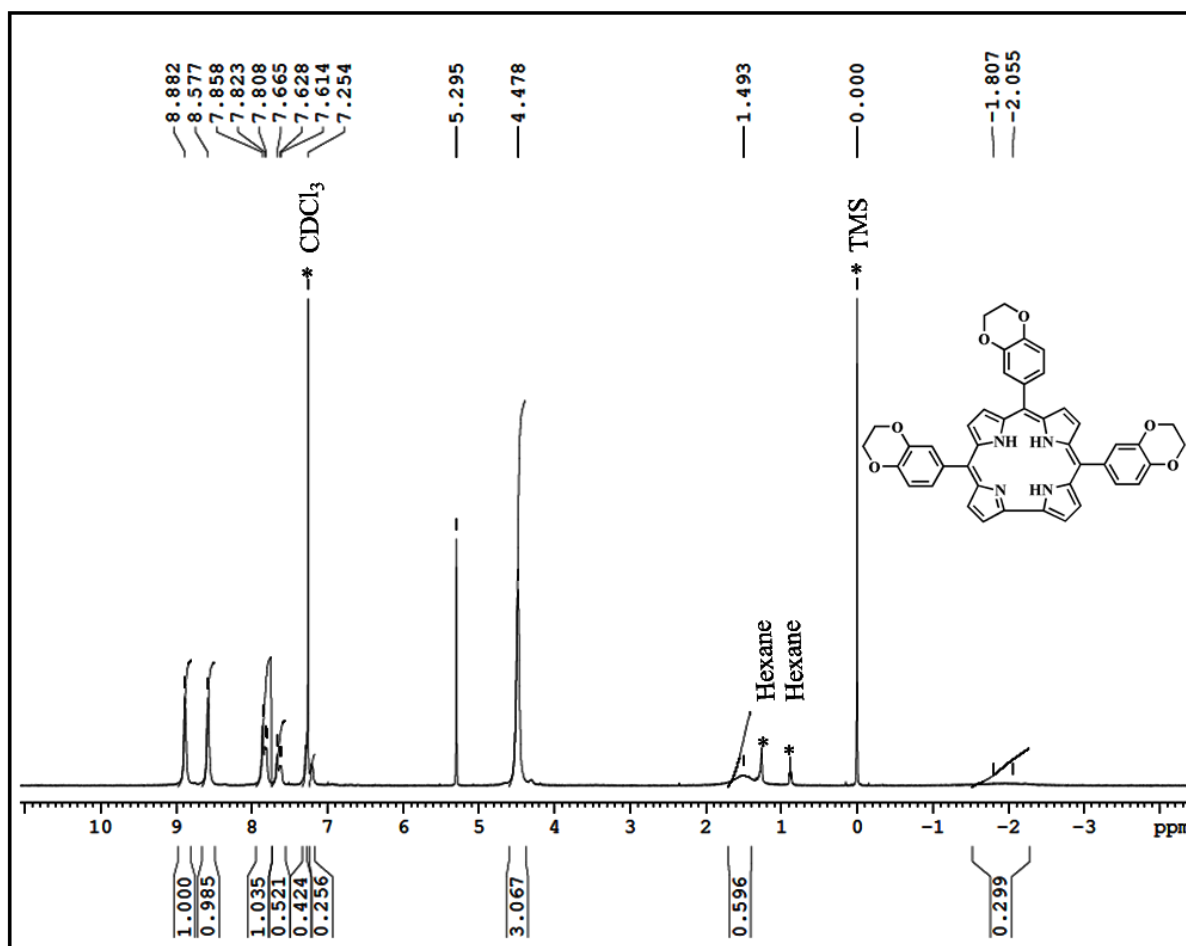


Figure 4.17. ¹H NMR spectrum of 5,10,15-tris[3,4-(1,4-dioxan)phenyl]corrole, **1** in CDCl₃.

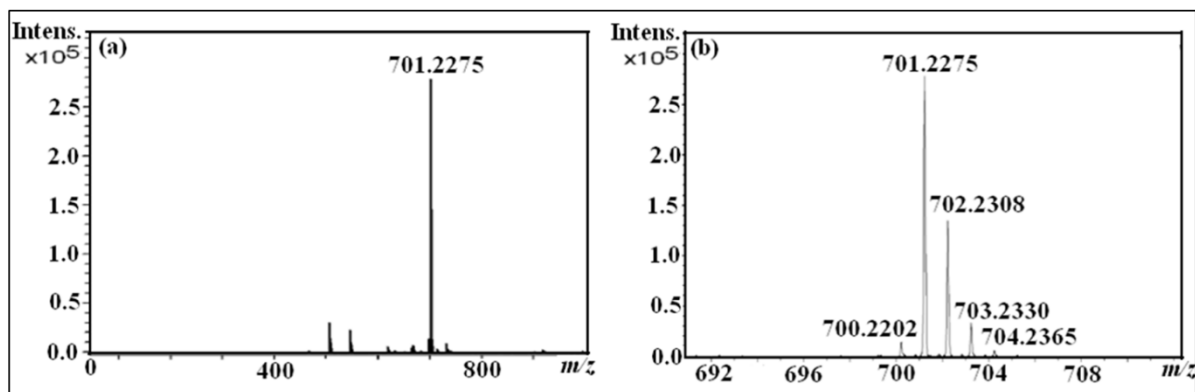


Figure 4.18. ESI-MS spectrum of 5,10,15-tris[3,4-(1,4-dioxan)phenyl]corrole, **1** in CH₃CN shows the measured spectrum with isotopic distribution pattern.

10-[4-(Chloroacetoxy)phenyl]-5,15-bis(2-bromo-5-fluoro phenyl)corrole, **2**.

0.99 g of 4-(chloroacetoxy)benzaldehyde (0.5 mmol) and 318 mg of 2-bromo-5-fluorophenyldipyromethane (1 mmol) were dissolved in 60 mL of dichloromethane. Then 3 μ L of TFA (0.04mmol) was added and the reaction was stirred for 5 h. Then the reaction mixture was diluted with 150 mL of dichloromethane and DDQ (227 mg, 1.01 mmol) in THF solution was added to it. The mixture was stirred for another 30 minutes. The mixture was evaporated and was subjected to column chromatography. After recrystallization from a mixture of DCM and hexane, it afforded a dark blue green color solid. Yield: 11% (46 mg). Anal. Calcd (found) for C₃₉H₂₃Br₂ClF₂N₄O₂ (**2**): C, 57.62 (57.53); H, 2.85 (2.71); N, 6.89 (6.75). λ_{max} /nm (ϵ /M⁻¹cm⁻¹) in dichloromethane: 409 (139100), 564(21 300), 607 (11500), 643 (6700) (Figure 4.3). ¹H NMR (400 MHz, CDCl₃) δ : 9.01 (d, J =4.1 Hz, 2 H), 8.61 (q, J =4.8 Hz, 4 H), 8.45 (d, J =4.1 Hz, 2 H), 8.29 - 8.13 (m, 2 H), 7.97 (dd, J =8.9, 5.4 Hz, 2 H), 7.85 (dt, J =8.5, 3.4 Hz, 2 H), 7.53 (d, J =8.5 Hz, 2 H), 7.38 (td, J =8.5, 3.1 Hz, 2 H), 4.48 (s, 2 H), 1.59 (brs, 2H), -2.35(brm, 1H) (Figure 4.19). ¹³C NMR (101 MHz, CDCl₃) δ : 166.2, 162.4, 159.9, 150.2, 142.1, 141.9, 140.1, 135.6, 135.6, 135.1, 133.9, 133.8, 131.0, 126.9, 126.9, 122.6, 122.5, 122.4, 122.3, 121.9, 121.9, 121.9, 121.8, 121.0, 120.1, 117.4, 117.2, 116.5, 112.9, 110.5, 41.2 (Figure 4.20). ESI-MS: m/z = 810.98 [**2**+H]⁺ (810.9844 calcd for C₃₉H₂₄Br₂ClF₂N₄O₂) (Figure 4.21). M.p>300°C. **2** displayed strong fluorescence at 654 nm

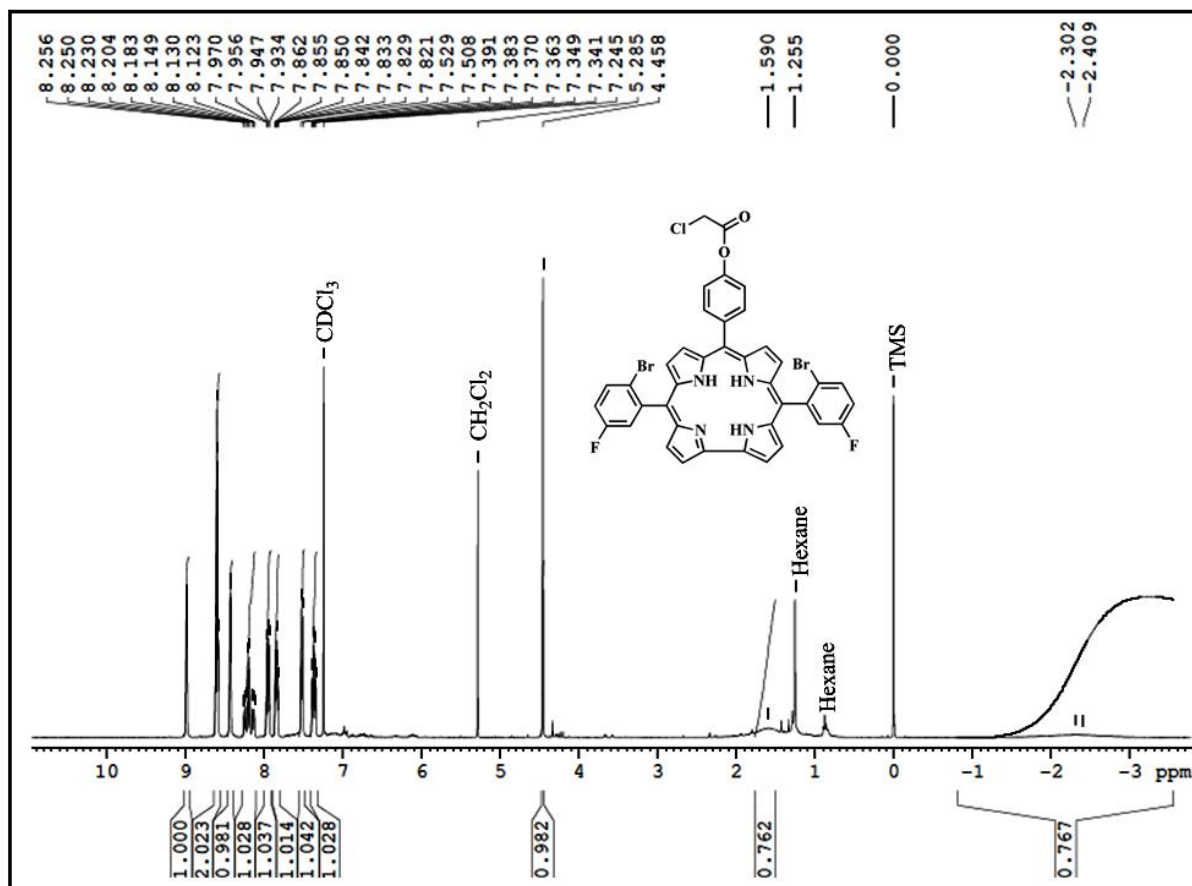


Figure 4.19. ^1H NMR spectrum of 10-[4-(chloroacetoxy) phenyl]-5,15-bis(2-bromo-5-fluoro phenyl)corrole, **2**, in CDCl_3 .

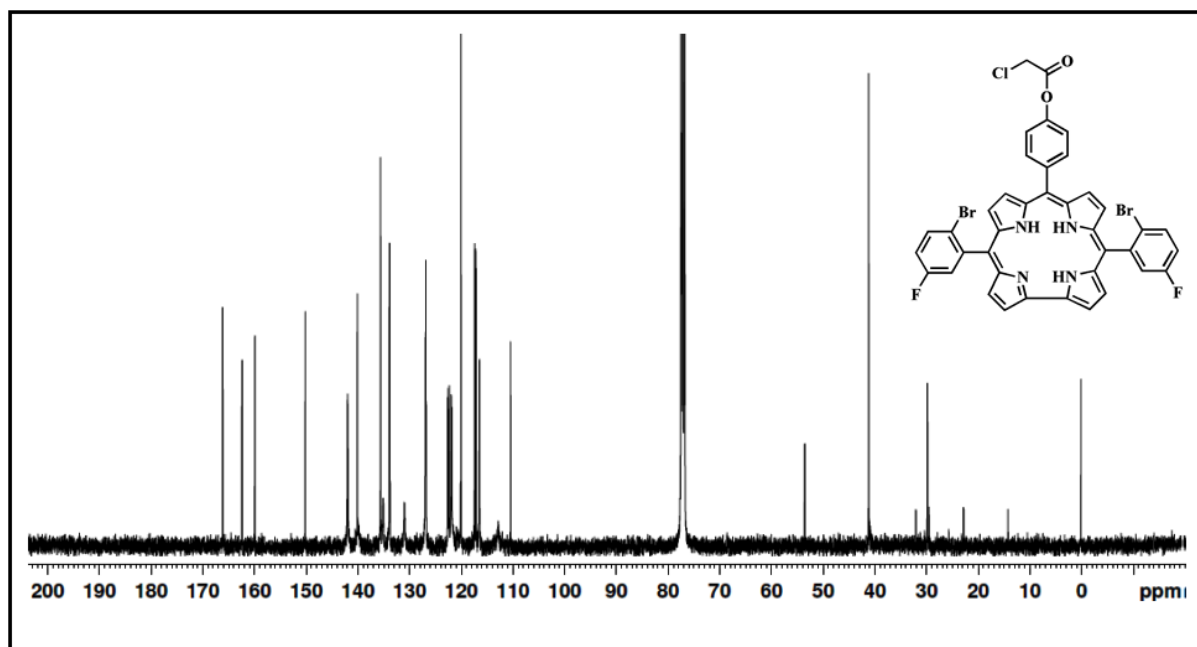


Figure 4.20. ^{13}C NMR spectrum of 10-[4-(chloroacetoxy)phenyl]-5,15-bis(2-bromo-5-fluorophenyl)corrole, **2**, in CDCl_3 .

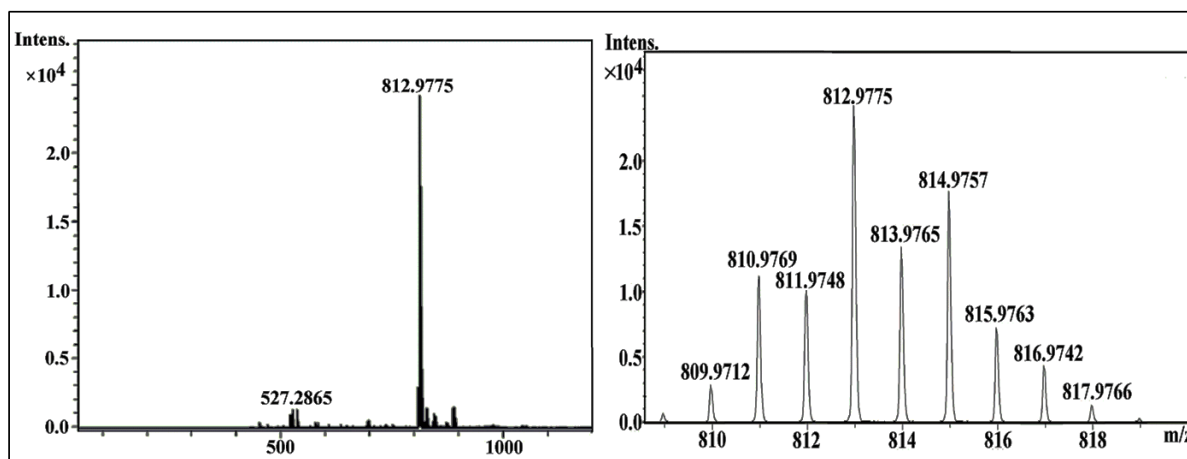


Figure 4.21. ESI-MS spectrum of 10-[4-(chloroacetoxy)phenyl]-5,15-bis(2-bromo-5-fluorophenyl)corrole, **2**, in CH₃CN shows the measured spectrum with isotopic distribution pattern.

(Figure 4.3), with excited state life time of 0.43 ns (Figure 4.4).

10-(4-Hydroxyphenyl)-5,15-bis(2-bromo-5-fluorophenyl)corrole, **3**.

In a 100 mL round bottom flask, 35 mg of 10-(4-(2-chloroacetoxy)phenyl)-5,15-bis(2-bromo-5-fluorophenyl)corrole (0.043 mmol) and 47 μ L of benzylamine (0.43 mmol) were taken in a mixture of THF (5 mL) and ethanol (5 mL). The mixture was refluxed for an hour. Then it was evaporated and was subjected to column chromatography (silica gel 100-200 mesh, EtOAc / hexane). After recrystallisation from a mixture of DCM and hexane, it afforded a dark blue green color solid. Yield: 70% (22 mg). Anal. Calcd (found) for C₃₇H₂₂Br₂F₂N₄O (**3**): C, 60.35 (60.53); H, 3.01 (3.20); N, 7.61 (7.77). λ_{max} /nm (ϵ /M⁻¹cm⁻¹) in dichloromethane: 410 (159000), 563 (24500), 608 (15600), 638 (11200) (Figure 4.3). ¹H NMR (400 MHz, CDCl₃) δ : 9.00 (d, J =4.2 Hz, 2 H), 8.68 - 8.54 (m, 4 H), 8.44(d, J =4.2 Hz, 2 H), 8.13 - 7.92 (m, 4 H), 7.86 (dt, J =8.8, 3.2 Hz, 2 H), 7.37 (td, J =8.4, 3.1 Hz, 2 H), 7.21 - 7.07 (m, 2 H), -0.35 (brs, 4 H) (Figure 4.22). ¹³C NMR (101 MHz, CDCl₃) δ : 162.3, 159.8, 154.7, 142.0, 139.7, 135.6, 135.2, 135.1, 134.1, 133.8, 133.7, 131.1, 131.0, 127.0, 126.5, 122.6, 122.4, 121.8, 117.3, 117.0, 116.5, 116.4, 114.0, 112.5, 111.4 (Figure 4.23) ESI-MS: $m/z = 735.0$ [**3**+H]⁺ (735.0128) calcd for C₃₇H₂₃Br₂F₂N₄O) (Figure 4.24). M.p>300°C.

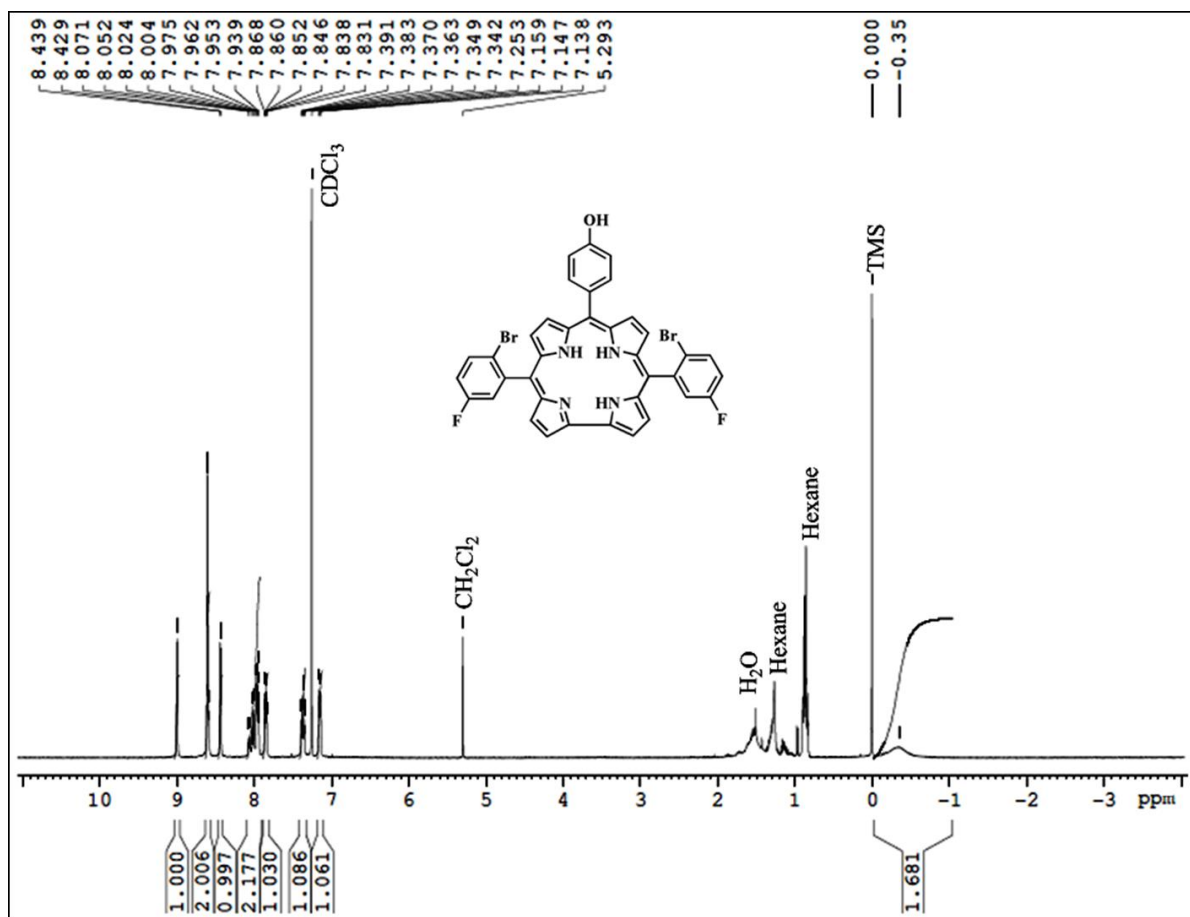


Figure 4.22. ¹H NMR spectrum of 10-(4-hydroxyphenyl)-5,15-bis(2-bromo-5-fluorophenyl)corrole, **3** in CDCl₃.

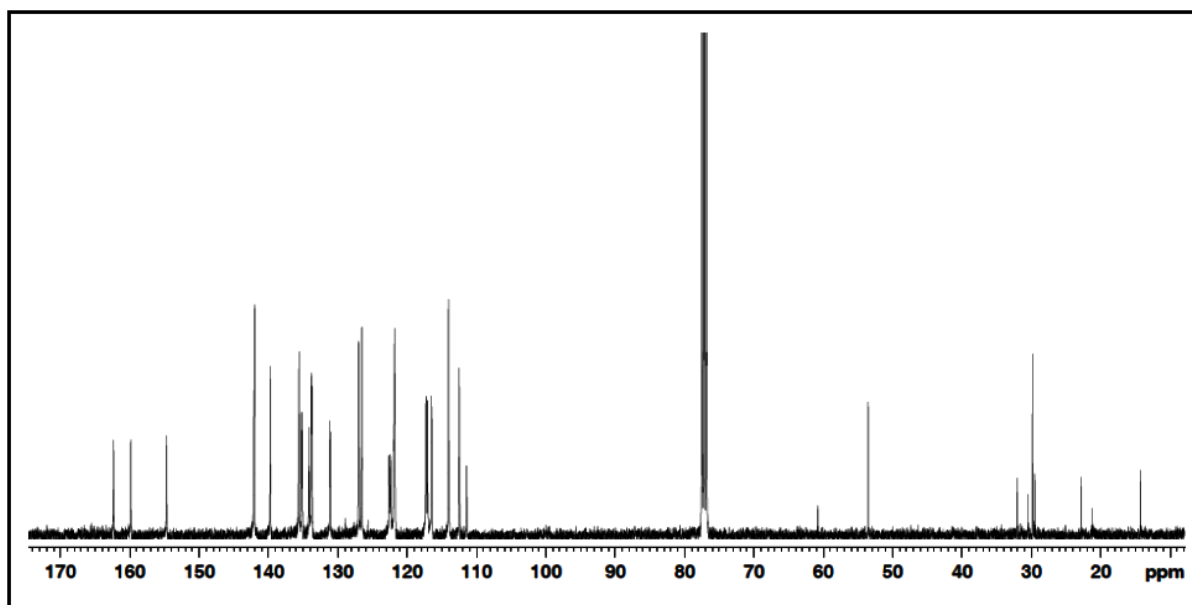


Figure 4.23. ¹³C NMR spectrum of 10-(4-hydroxyphenyl)-5,15-bis(2-bromo-5-fluorophenyl)corrole, **3** in CDCl₃.

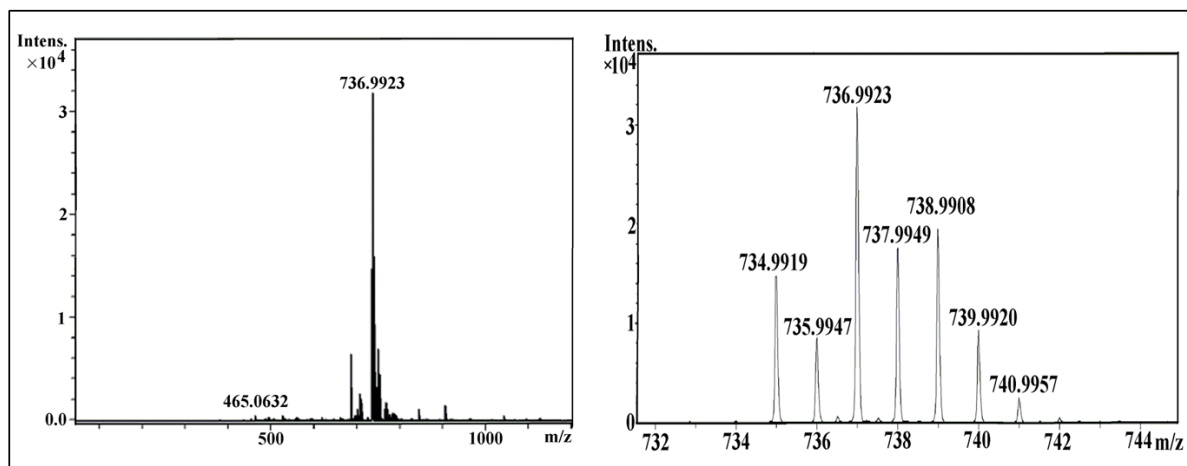


Figure 4.24. ESI-MS spectrum of 10-(4-hydroxyphenyl)-5,15-bis(2-bromo-5-fluorophenyl)corrole, **3** in CH_3CN shows the measured spectrum with isotopic distribution pattern.

3 displayed strong fluorescence at 661 nm (Figure 4.3), with excited state life time of 0.34 ns (Figure 4.4).

References

1. Prasad, P. N.; Williams, D. J., Wiley: New York, USA, **1990**.
2. Baldwin, G. C., Plenum: New York, USA, **1996**.
3. Coe, B. J.; Chamberlain, M. C.; Essex-Lopresti, J. P.; Gaines, S.; Jeffery, J. C.; Houbrechts, S.; Persoons, A., *Inorg. Chem.*, **1997**, *36*, 3284-3292.
4. Whittall, I. R.; McDonagh, A. M.; Humphrey, M. G.; Samoc, M., *Adv. Organomet. Chem.*, **1998**, *42*, 291-362.
5. McDonagh, A. M.; Humphrey, M. G.; Samoc, M.; Luther-Davies, B.; Houbrechts, S.; Wada, T.; Sasabe, H.; Persoons, A., *J. Am. Chem. Soc.*, **1999**, *121*, 1405-1406.
6. Karotki, A.; Drobizhev, M.; Dzenis, Y.; Taylor, P. N.; Anderson, H. L.; Rebane, A., *Phys. Chem. Chem. Phys.*, **2004**, *6*, 7-10.
7. Saleh, B. E. A.; Teich, M. C., *Fundamentals of Photonics*. Wiley, New York: New York, **1991**; p 983.
8. Hann, R. A.; Bloor, D., Royal Society of Chemistry: London, UK, **1991**.
9. Ashwell, G. J.; Bloor, D., Royal Society of Chemistry: **1993**.
10. Linstead, R. P., *J. Chem. Soc.*, **1934**, 1016-1017.
11. Kadish, K. M.; Smith, K. M.; Guillard, R., *The Porphyrin Handbook*. Eds. Academic: New York, USA, **2003**.
12. Suslick, K. S.; Chen, C. T.; Meredith, G. R.; Cheng, L. T., *J. Am. Chem. Soc.*, **1992**, *114*, 6928-6930.
13. Senge, M. O.; Fazekas, M.; Notaras, E. G. A.; Blau, W. J.; Zawadzka, M.; Locos, O. B.; Ni Mhuirheartaigh, E. M., *Adv. Mater.*, **2007**, *19*, 2737-2774.
14. D. S. Chemla; J. Zyss; Chemla, D. S.; Zyss, J., Eds. Academic: Orlando, USA, **1987**; Vol. I and II.

15. Rebane, A.; Drobizhev, M.; Makarov, N. S.; Koszarna, B.; Tasiar, M.; Gryko, D. T., *Chem. Phys. Lett.*, **2008**, *462*, 246-250.
16. Anusha, P. T.; Swain, D.; Hamad, S.; Giribabu, L.; Prashant, T. S.; Tewari, S. P.; Rao, S. V., *J. Phys. Chem. C*, **2012**, *116*, 17828-17837.
17. Guillard, R.; Barbe, J.-M.; Stern, C.; Kadish, K. M., in: *The Porphyrin Handbook*, Kadish, K. M.; Smith, K. M.; Guillard, R. Elsevier Science: USA, 2000.
18. Ding, T.; Alemán, E. A.; Modarelli, D. A.; Ziegler, C. J., *J. Phys. Chem. A*, **2005**, *109*, 7411-7417.
19. Ventura, B.; Degli Esposti, A.; Koszarna, B.; Gryko, D. T.; Flamigni, L., *New J. Chem.*, **2005**, *29*, 1559-1566.
20. Flamigni, L.; Ventura, B.; Tasiar, M.; Becherer, T.; Langhals, H.; Gryko, D. T., *Chem. Eur. J.*, **2008**, *14*, 169-83.
21. Aviv, I.; Gross, Z., *Chem. Commun. (Cambridge, U. K.)*, **2007**, 1987-1999.
22. Koszarna, B.; Gryko, D. T., *J. Org. Chem.*, **2006**, *71*, 3707-3717.
23. Paolesse, R.; Marini, A.; Nardis, S.; Froiio, A.; Mandoj, F.; Nurco, D. J.; Prodi, L.; Montalti, M.; Smith, K. M., *J. Porphyrins Phthalocyanines*, **2003**, *07*, 25-36.
24. Gryko, D. T.; Jadach, K., *J. Org. Chem.*, **2001**, *66*, 4267-4275.
25. Barbe, J.-M.; Canard, G.; Brandès, S.; Guillard, R., *Eur. J. Org. Chem.*, **2005**, *2005*, 4601-4611.
26. Will, S.; Lex, J.; Vogel, E.; Schmickler, H.; Gisselbrecht, J.-P.; Hauptmann, C.; Bernard, M.; Gorss, M., *Angew. Chem., Int. Ed. Engl.*, **1997**, *36*, 357-361.
27. Guillard, R.; Gros, C. P.; Barbe, J.-M.; Espinosa, E.; Jérôme, F.; Tabard, A.; Latour, J.-M.; Shao, J.; Ou, Z.; Kadish, K. M., *Inorg. Chem.*, **2004**, *43*, 7441-7455.
28. Sinha, W.; Deibel, N.; Agarwala, H.; Garai, A.; Schweinfurth, D.; Purohit, C. S.; Lahiri, G. K.; Sarkar, B.; Kar, S., *Inorg. Chem.*, **2014**, *53*, 1417-1429.

29. Albrett, A. M.; Thomas, K. E.; Maslek, S.; Młodzianowska, A.; Conradie, J.; Beavers, C. M.; Ghosh, A.; Brothers, P. J., *Inorg. Chem.*, **2014**, *53*, 5486-5493.
30. Gouterman, M.; Wagniere, G.; Snyder, L. R., *J. Mol. Struct.*, **1963**, *11*, 108-127.
31. Koszarna, B.; Gryko, D. T., *Chem. Commun.*, **2007**, 2994-2996.
32. Sinha, W.; Sommer, M. G.; Deibel, N.; Ehret, F.; Sarkar, B.; Kar, S., *Chem. -Eur. J.*, **2014**, *20*, 15920-15932.
33. Sinha, W.; Kar, S., *Organometallics*, **2014**, *33*, 6550-6556.
34. Rochford, J.; Galoppini, E., *Langmuir*, **2008**, *24*, 5366-5374.
35. Gryko, D. T.; Koszarna, B., *Org. Biomol. Chem.*, **2003**, *1*, 350-357.
36. Strachan, J.-P.; Gentemann, S.; Seth, J.; Kalsbeck, W. A.; Lindsey, J. S.; Holten, D.; Bocian, D. F., *J. Am. Chem. Soc.*, **1997**, *119*, 11191-11201.
37. Srinivasarao, M.; Collings, D.; Philips, A.; Patel, S., *Science*, **2001**, *292*, 79-83.
38. Valdes-Aguilera, O.; Neckers, D. C., *Acc. Chem. Res.*, **1989**, *22*, 171-177.
39. Hill, E. H.; Sanchez, D.; Evans, D. G.; Whitten, D. G., *Langmuir*, **2013**, *29*, 15732-15737.
40. Mooney, W. F.; Whitten, D. G., *J. Am. Chem. Soc.*, **1986**, *108*, 5712-5719.
41. Falconieri, M.; Salvetti, G., *Appl. Phys. B: Lasers Opt.*, **1999**, *69*, 133-136.
42. Gedikpınar, M.; Çavaş, M.; Alahmed, Z. A.; Yakuphanoglu, F., *Superlattices Microstruct.*, **2013**, *59*, 123-132.
43. Gnoli, A.; Razzari, L.; Righini, M., *Opt. Express*, **2005**, *13*, 7976-7981.
44. Nalda, R. d.; Coso, R. d.; Requejo-Isidro, J.; Olivares, J.; Suarez-Garcia, A.; Solis, J.; Afonso, C. N., *J. Opt. Soc. Am. B*, **2002**, *19*, 289-296.
45. Kamada, K.; Matsunaga, K.; Yoshino, A.; Ohta, K., *J. Opt. Soc. Am. B*, **2003**, *20*, 529-537.
46. Huang, C.; Li, Y.; Song, Y.; Li, Y.; Liu, H.; Zhu, D., *Adv. Mater.*, **2010**, *22*, 3532-6.

47. Ramirez, E. V. G.; Carrasco, M. L. A.; Otero, M. M. M.; Lara, E. R.; Chavez-Cerda, S.; Castillo, M. D. I., *J. Opt.*, **2011**, *13*, 085203.
48. Sheik-Bahae, M.; Said, A. A.; Wei, T. H.; Hagan, D. J.; Van Stryland, E. W., *IEEE J. Quantum Electron.*, **1990**, *26*, 760-769.
49. Rashidian Vaziri, M. R., *Appl. Opt.*, **2013**, *52*, 4843-4848.
50. Kwak, C. H.; Lee, Y. L.; Kim, S. G., *J. Opt. Soc. Am. B*, **1999**, *16*, 600-604.
51. Pálfalvi, L.; Tóth, B. C.; Almási, G.; Fülöp, J. A.; Hebling, J., *Appl. Phys. B: Lasers Opt.*, **2009**, *97*, 679-685.
52. Chen, S.-Q.; Liu, Z.-B.; Zang, W.-P.; Tian, J.-G.; Zhou, W.-Y.; Song, F.; Zhang, C.-P., *J. Opt. Soc. Am. B*, **2005**, *22*, 1911-1916.
53. Kovsh, D.; Hagan, D.; Van Stryland, E., *Opt. Express*, **1999**, *4*, 315-327.
54. Cho, S.; Lim, J. M.; Hiroto, S.; Kim, P.; Shinokubo, H.; Osuka, A.; Kim, D., *J. Am. Chem. Soc.*, **2009**, *131*, 6412-6420.
55. Kruk, M.; Karotki, A.; Drobizhev, M.; Kuzmitsky, V.; Gael, V.; Rebane, A., *J. Lumin.*, **2003**, *105*, 45-55.
56. Morone, M.; Beverina, L.; Abbotto, A.; Silvestri, F.; Collini, E.; Ferrante, C.; Bozio, R.; Pagani, G. A., *Org. Lett.*, **2006**, *8*, 2719-2722.
57. Drobizhev, M.; Meng, F.; Rebane, A.; Stepanenko, Y.; Nickel, E.; Spangler, C. W., *J. Phys. Chem. B*, **2006**, *110*, 9802-9814.
58. Ogawa, K.; Ohashi, A.; Kobuke, Y.; Kamada, K.; Ohta, K., *J. Am. Chem. Soc.*, **2003**, *125*, 13356-13357.
59. Swain, D.; Anusha, P. T.; Shuvan Prashant, T.; Tewari, S. P.; Sarma, T.; Panda, P. K.; Venugopal Rao, S., *Appl. Phys. Lett.*, **2012**, *100*, 141109.
60. Ahlrichs, R.; Bär, M.; Häser, M.; Horn, H.; Kölmel, C., *Chem. Phys. Lett.*, **1989**, *162*, 165-169.

61. Treutler, O.; Ahlrichs, R., *J. Chem. Phys.*, **1995**, *102*, 346-354.
62. Vahtras, O.; Almlöf, J.; Feyereisen, M. W., *Chem. Phys. Lett.*, **1993**, *213*, 514-518.
63. Eichkorn, K.; Treutler, O.; Öhm, H.; Häser, M.; Ahlrichs, R., *Chem. Phys. Lett.*, **1995**, *242*, 652-660.
64. Eichkorn, K.; Treutler, O.; Öhm, H.; Häser, M.; Ahlrichs, R., *Chem. Phys. Lett.*, **1995**, *240*, 283-290.
65. Sheldrick, G. M., *Acta Crystallogr., Sect. A: Found. Crystallogr.*, **2008**, *64(1)*, 112-122.

Summery and Future Prospect

Porphyrin chemistry is well explored over multidisciplinary area but there is a lack of facile synthetic protocol for cyano substituted porphyrin. A number of multistep complex protocols are reported till date. Herein, a two-step one pot synthesis has been developed. Most interesting feature of this protocol is the complete absence of porphyrin/metalloporphyrin based starting materials and additional reagents for cyanation as DDQ is performing dual role of cyanation as well as oxidative macrocyclization. This protocol would be highly beneficial to install interesting functional groups to the porphyrin macrocycle for potential application in different field.

Application of metalloporphyrin in the material science is quite elusive but fabrication of metalloporphyrin-fullerene based nano-architecture based MIS type diode is novel and quite informative. Present study reveals its future application as charge storage devices.

On the other side, one *meso* carbon contracted porphyrinoid, corrole has created an independent and new area of interest. Free base corrole and its main group metal derivative show very fascinating photophysical properties. Literature study reveals that due to the strong conjugation and reduced symmetry of the macrocycle, there is a large enhancement of 2PA. Here, we have explored NLO properties (nonlinear refractive index, n_2 and two-photon absorption coefficient, β) of a series of novel corrole systems both in solution state and in aggregated state. Detailed investigation dictates that these corrole systems could be potential promising candidates in their aggregated state for devising optical switch which can have direct applications in high-speed communication technology.